CENTRUM FIZYKI TEORETYCZNEJ
POLSKIEJ AKADEMII NAUK

DOCTORAL THESIS

Modeling Magnetized Jets from Accreting Black Holes

Author:
Bestin James

Supervisor:
Prof. Agnieszka Janiuk

Thesis submitted in partial fulfillment of the requirements for the degree of Doctor of Philosophy in Physics

Warsaw, June 2023

Declaration of Authorship

I hereby declare that this thesis represents my work which has been done after the registration for the degree of PhD at the Center for Theoretical Physics of the Polish Academy of Sciences (CTP PAS) and has not been included in any other thesis or dissertation submitted to this or any other institution for a degree, diploma or other qualifications. I confirm that the work submitted is my own and I have acknowledged all main sources of help. This thesis includes the following works:

- **"Variability of Magnetically Dominated Jets from Accreting Black Holes."** Authors: Agnieszka Janiuk, Bestin James and Ishika Palit, published in The Astrophysical Journal (ApJ) (Janiuk, James, and Palit, 2021).
- **"Modeling the Gamma-Ray Burst Jet Properties with 3D General Relativistic Simulations of Magnetically Arrested Accretion Flows."** Authors: Bestin James, Agnieszka Janiuk and Fatemeh Hossein Nouri, published in The Astrophysical Journal (ApJ) (James, Janiuk, and Nouri, 2022).
- **"Black hole outflows initiated by accretion of large-scale magnetic fields."** Authors: Bestin James, Vladimír Karas and Agnieszka Janiuk (manuscript in preparation).

Wherever contributions of others are involved, every effort is made to indicate this clearly, with due reference to the literature, and acknowledgement of collaborative research and discussions. The thesis work was done under the guidance of Prof. Agnieszka Janiuk at CTP PAS, Warsaw, Poland.

Bestin James

June 16, 2023

Other Contributions

I worked on one more main project during my PhD studies, in addition to the works mentioned above, and contributed as a co-author in the resulting article:

- **"Magnetically arrested accretion disks launching structured jets in application to GRB and AGN engines".** Authors: Agnieszka Janiuk and Bestin James, published in Astronomy & Astrophysics (A&A) (Janiuk and James, 2022).

In this work, we investigated the disk-jet connection, in the context of gamma-ray bursts and active galactic nuclei, by means of 3D general relativistic magnetohydrodynamical simulations of the magnetically arrested accretion flows. We studied a family of models with varying black hole spin, disk mass, and disk magnetization strength, and evaluated the effects of these parameters on the resulting flows. I worked mainly on quantifying the variability of jet emission by means of Fourier analysis.

In addition, I also authored/co-authored the following conference proceedings during my tenure as a doctoral student:

- **"Numerical Study of Magnetically Dominated Jets from Accreting Black Hole Sources."** Authors: Bestin James and Agnieszka Janiuk, published in Acta Physica Polonica B Proceedings Supplement (James and Janiuk, 2022).
- **"Cosmic Gamma Ray Bursts."** Authors: Agnieszka Janiuk, Bestin James and Konstantinos Sapountzis, published in Acta Physica Polonica A (Janiuk, James, and Sapountzis, 2021).
- **"Multi-messenger signals from short gamma ray bursts."** Authors: Agnieszka Janiuk, Konstantinos Sapountzis, Bestin James and Martin Kološ, published in Proceedings of Science (Multifrequency Behaviour of High Energy Cosmic Sources - XIII) (Janiuk et al., 2020).

To my beloved parents

Abstract

Modeling Magnetized Jets from Accreting Black Holes

Relativistic jets are a very common phenomenon in high-energy astrophysics, observed in many sources including active galactic nuclei (AGNs) and gamma-ray bursts (GRBs). Some of the largest and most active jets are produced by supermassive black holes residing at the center of active galaxies and extend to millions of parsecs in length. The gamma-ray bursts, which are the most luminous electromagnetic events after the big bang, are thought to be highly focused explosions with most of their energy collimated to narrow relativistic jets. The formation of these jets can be attributed usually to the dynamic interactions within the accretion flows onto a central compact object such as a black hole or a neutron star. This thesis aims to explore the connection between the magnetized accretion flows in the central engine of these sources and the associated jet properties, and provide a clearer description of the origin, spatial structure and temporal variability of the observed jets. The studies are carried out with general relativistic magnetohydrodynamic (GRMHD) simulations of accretion flows and the associated jet base in the Kerr geometry around a black hole.

Observational studies have found correlations between the measured jet variability and the Lorentz factor, which span several orders of magnitude of the central engine mass, covering both GRB and blazar samples. The first part after the introductory chapters of the thesis (Chapter 3) presents an investigation into the possible connections between the jet energetics and temporal variability taking mainly into account the disk magnetization and the black hole spin. The study is conducted by performing axisymmetric ideal GRMHD simulations and probing the jet energetics along different points of the line of sight. The time variability of the jet is also measured at these chosen locations. The results are quantified by computing the minimum variability time scale (MTS), its power density spectra and the jet Lorentz factors (Γ) and the MTS-Γ anti-correlation is qualitatively obtained in our models. The black hole spin can be attributed as the main driving parameter of the engine, which is reflected in the jet Lorentz factors.

The second part of the thesis (Chapter 4) focuses on the jet properties of gamma-ray bursts by considering a magnetically arrested disk (MAD) as the central engine. This work explores the possible dependence of the jet structure and temporal variability in the gamma-ray burst jets on the MAD state. The simulations are done in 3D with non-axisymmetric time evolution, by introducing random perturbations in the gas internal energy to the axisymmetric initial conditions. The models described in this work reach a MAD state and self-consistently produce structured jets with very fast variability in time. The models from this work are applied to the particular cases of short and long GRB systems and the results are analyzed in comparison with the observations.

The third part of the thesis (Chapter 5) focuses on outflows driven by large-scale magnetic fields in the vicinity of a black hole. This work examines the competing effects of inflows and outflows driven by a large-scale asymptotically uniform magnetic field in the Kerr geometry starting from a spherically symmetric inflow. This in turn results in the magnetic field lines being accreted with the plasma while intermittent outflows develop mainly in the equatorial region. This work provides insight into the effects of magnetized accretion onto rotating black holes and the associated outflows.

Streszczenie

Relatywistyczne dżety astrofizyczne są zjawiskiem powszechnie obserwowanym w zakresie wysokich energii, w obiektach takich jak aktywne jądra galaktyk (AGN) oraz rozbłyski gamma (GRB). Jedne z największych i najbardziej aktywnych dżetów wyrzucane są z okolic supermasywnych czarnych dziur, rezydujących w centrach galaktyk – osiągają one rozmiary milionów parseków. Z kolei rozbłyski gamma, które są najjaśniejszymi eksplozjami znanymi we Wszechświecie, poza Wielkim Wybuchem, są uważane za silnie skolimowane wyrzuty dżetów, w których większość energii jest wyświecana w jego wąskim stożku. Pochodzenie dżetów przypisuje się zazwyczaj dynamice interakcji w obrębie przepływu akrecyjnego materii na zwarty obiekt, taki jak czarna dziura bądź gwiazda neutronowa. W niniejszej rozprawie zajmujemy się związkami pomiędzy namagnesowanym przepływem akrecyjnym w centralnym silniku przyspieszającym dżet a właściwościami samego dżetu. Przedstawiamy tutaj spójny opis powstawania, struktury oraz zmienności czasowej obserwowanej w dżetach. Badania prowadzone są przy pomocy symulacji komputerowych z wykorzystaniem algorytmów relatywistycznej magnetohydrodynamiki (GRMHD). Modelujemy nimi przepływy akrecyjne oraz powstawanie dżetów w geometrii Kerra, w polu grawitacyjnym czarnej dziury.

Obserwacje potwierdziły istnienie korelacji pomiędzy obserwowaną zmiennością dżetów a ich czynnikiem Lorentza, obejmujące kilka rzędów wielkości w zakresie masy centralnego silnika, charakterystycznych zarówno dla rozbłysków gamma, jak i dla próbki blazarów. Pierwszy główny rozdział niniejszej pracy, po wstępie (Rozdział 3), omawia sprawdzenie możliwych powiązań pomiędzy energetyką dżetu a jego zmiennością czasową. Bierzemy pod uwagę różne magnetyzacje dysku oraz tempa rotacji czarnych dziur. Badania prowadzone są w zakresie osiowosymetrycznych symulacji GRMHD. Energetyka dżetu jest próbkowana w różnych pozycjach względem linii widzenia. Zmienność czasowa dżetu jest mierzona w tych samych lokalizacjach. Wyniki zostały przeanalizowane za pomocą wyznaczenia minimalnych skal czasowych zmienności (MTS), widm mocy zmienności (PDS), czynników Lorentza (Gamma), oraz korelacji MTS-Gamma. Ilościowo przedstawiamy je w niniejszej pracy. Spin czarnej dziury okazuje się głównym parametrem determinującym działanie silnika, co znajduje odzwierciedlenie w wyznaczonych czynnikach Lorentza.

Kolejna część tej pracy (Rozdział 4) koncentruje się na właściwościach dżetów w rozbłyskach gamma, przy założeniu centralnego silnika opartego na modelu magnetycznie aresztowanego dysku (MAD). Praca ta eksploruje charakterystyczną strukturę dżetu i jego zmienność w stanie MAD. Symulacje przedstawione w tym rozdziuale zostały wykonane w oparciu o nieosiowo symetryczny schemat 3D i ewolucję czasową, w której w warunku początkowym zostaje zadana losowa perturbacja w rozkładzie energii wewnętrznej w gazie, zaburzająca symetrię osiową. Modele przedstawione w tym rozdziale osiągają stan MAD i w spójny sposób produkują ustrukturyzowane dżety, bardzo szybko zmienne w czasie. Modele te zostały zaaplikowane do szczególnych dwóch typów obiektów, odpowiadających silnikom długiego lub krótkiego rozbłysku gamma. Wyniki przedyskutowaliśmy w oparciu o dostępne obserwacje tego typu źródeł.

Trzecia część pracy (Rozdział 5) koncentruje się na wypływach wspomaganych obecnością wielkoskalowych pól magnetycznych w okolicy czarnej dziury. Praca ta bada współzawodniczące efekty działania asymptotycznie jednorodnego pola magnetycznego w metryce Kerra, gdzie wypływ towarzyszy opadaniu materii, o początkowo sferycznie symetrycznym rozkładzie. W efekcie tego procesu,

linie pola magnetycznego są wciągane razem z gazem, podczas gdy okazjonalne wypływy rozwijają się głównie w płaszczyźnie równikowej. Praca ta oferuje wgląd w strukturę namagnesowanej akrecji na silnie rotującą czarną dziurę i związane z nią wypływy.

Acknowledgements

This thesis is complete only with these words of gratitude to all the people who helped and supported me along the way, from the beginning.

First and foremost, I thank my parents, Daisy and James, without whom I would not have reached this point in my life. I owe you almost everything good that I have become to this very day, and I will always cherish your constant encouragement and kind support in all the hard times of my life.

Now I would like to express my gratitude to my supervisor, Professor Agnieszka Janiuk, who made the journey of my PhD a fruitful one from the very beginning. Thank you for mentoring me in the field of astrophysics and for kindly giving me the opportunity to work with you. I am immensely grateful for your encouragement and advice at every step of my journey over the past four years. I have always been amazed by your constant enthusiasm for scientific work, clarity of thought, precision in scientific thinking, and great moral character. I hope to carry on with me at least some of the good qualities I learned from you.

I thank my sisters, Binet and Blaize Maria, for all the support you have given me since my childhood and for being there for me whenever I need you. I am extremely grateful to Weronika for becoming part of my life and for the never-ending love, happiness, and positivity you bring into my life every single day since we met. I also thank my whole family, including many of its members, who support me with their kind deeds and words that also make me who I am today.

Now, I would like to thank my scientific collaborators, prof. Vladimír Karas, from the Czech Academy of Sciences, and Fatemeh, Ishika, and Gerardo, with whom I worked together at CFT, for all the moral support, scientific insights, and the great collaborative environment you have provided me throughout this time. It has been a pleasure working with each of you. I also thank Kostas, from the University of Athens, and Martin, from Silesian University in Opava, for all the support and illuminating discussions that positively enhanced my research at different stages.

The journey of my PhD has not always been the easiest one, and friends always come to the rescue when it is hard. I would like to express my gratitude to my friends: Suresh, Abin, Ajith, Daris, Jijo, Sachu, Unni and many others; my friends from IFPAN: Sarath, Yadhu, Ajeesh, and others; my friends and colleagues from CFT: Suhani, Julius, Michele, Grzegorz, Owidiusz, Jakub, Tae-Hun, Raj, Vikram, Anjitha, and others; and many others from the different walks of my life who have helped and supported me at various stages. It is impossible to include all the names here as they will span many pages, but my gratitude to all the people who have helped, supported, and inspired me along the way will always be there with me.

I would also like to extend my thanks to prof. Lech Mankiewicz, then director and now the chair of the science council of the institute, for the kind support and guidance provided to me when I joined here from another country. I also thank prof. Maciej Billicki, the current coordinator of our doctoral school, for timely reminders on all bureaucratic requirements and the help. I would also like to thank all the other professors of CFT who have supported and inspired me at various stages. I also thank the members of my doctoral committee and the reviewers of my thesis for your kind service.

I also thank the current and former administrative, accounting and IT staff of the institute for doing their job so well that all the bureaucratic, financial and technical requirements for me are always fulfilled at the proper time.

Contents

List of Figures

List of Tables

List of Abbreviations

ADAF	Advection Dominated Accretion Flow
AGN	Active Galactic Nucleus
BP	Blandford & Payne
BZ	Blandford & Znajek
FM	Fishbone & Moncrief
GR	General theory of Relativity
GRB	Gamma-ray Burst
GRMHD	General Relativistic Magnetohydrodynamic(s)
HLL	Harten, Lax, van Leer
KS	Kerr-Schild
MAD	Magnetically Arrested Disk
MHD	Magnetohydrodynamic(s)
MRI	Magneto-rotational Instability
MTS	Minimum variability Time Scale
PL	Power-law
SANE	Standard And Normal Evolution

Physical Constants & Other Units

Speed of Light	$c = 2.997\,924\,58 \times 10^{8}\ \mathrm{m\,s^{-1}}$
Permittivity of Free Space	$\epsilon_0 = 8.854\,188 \times 10^{-12}\ \mathrm{A^2 s^4 kg^{-1} m^{-3}}$
Gravitational Constant	$G = 6.674\,30 \times 10^{-11}\ \mathrm{m^3 kg^{-1} s^{-2}}$
Planck Constant	$h = 6.626\,070\,15 \times 10^{-34}\ \mathrm{m^2 kg s^{-1}}$
Boltzmann Constant	$k_B = 1.380\,649 \times 10^{-23}\ \mathrm{m^2 kg s^{-2} K^{-1}}$
Solar Mass	$M_\odot = 1.988\,47 \times 10^{30}\ \mathrm{kg}$
Permeability of Free Space	$\mu_0 = 1.256\,637 \times 10^{-6}\ \mathrm{m kg s^{-2} A^{-2}}$
Universal Gas Constant	$\mathcal{R} = 8.314\,459\,8\ \mathrm{J mol^{-1} K^{-1}}$

Chapter 1

Introduction

Accretion is the accumulation of matter onto a central massive object due to gravity. It is observed at various mass scales in the universe ranging from stars to supermassive black holes. Most astronomical objects we see in our universe, from planets to galaxies, are formed through accretion. Accretion also results in various observable phenomena which power most of the brightest events in the universe. Many of these bright events or objects often have jets associated with them as well. An astrophysical jet is a physical phenomenon in which ionized matter and radiation are emitted in an extended beam along the rotation axis of the central object under consideration. In this thesis, the focus is on the accretion onto compact objects resulting in such electromagnetically bright events, the associated jets observed in our universe and their interconnection.

1.1 Compact objects

Compact objects in astrophysics are either the resulting remnants of stellar evolution such as neutron stars and stellar mass black holes or their higher mass counterparts, supermassive black holes.

Neutron stars are formed as the result of massive stars (with masses higher than $\sim 8\ M_\odot$ and up to $\sim 40\ M_\odot$) running out of further fissile material at their core (Fryer and Hungerford, 2005). It was known at the beginning of the 1900s that when a star reaches such a stage, it shrinks to find a new equilibrium configuration supported by the quantum degeneracy pressure of electrons which stops the further collapse and the resulting object is a white dwarf. But in 1931, Subrahmanyan Chandrasekhar showed that there is a critical mass limit[1], now known as the Chandrasekhar limit, above which the electron degeneracy pressure cannot stop the process and the whole body collapses further (Chandrasekhar, 1931). This mass limit is $\sim 1.4\ M_\odot$. It was later found that the core of such a star collapses further crushing together all the matter present in it to form neutrons and the degeneracy pressure of the neutrons prevents further collapse of the object which results in a neutron star. Later in 1939, it was found that there is a maximum mass of the object beyond which even the quantum pressure of neutrons cannot stop the collapse (Tolman, 1939; Oppenheimer and Volkoff, 1939). This limit is at $\sim 3\ M_\odot$ beyond which the object collapses to a (stellar mass) black hole, due to the immense gravity of the matter present in it. Recent gravitational wave observation of the merger of two neutron stars, GW170817, gives a lower estimate for this maximum mass limit. The estimates are in the ranges e.g. $\sim 2.01\ M_\odot$ to $\sim 2.16\ M_\odot$ (Rezzolla, Most, and Weih, 2018) and $\sim 2.16\ M_\odot$ to $\sim 2.28\ M_\odot$ (Ruiz, Shapiro, and Tsokaros, 2018). The uncertainty in the limit to this mass comes

[1] Chandrasekhar improved upon the works of Stoner, 1930 and Anderson, 1929 to obtain this value of the limiting mass

from the difficulty in clearly determining the correct equation of state of matter at the endpoint of thermonuclear evolution at densities much above nuclear densities (Hartle, 1978).

The supermassive black holes on the other hand may have formed from the early cosmic times (Fan et al., 2001) through still unclear formation mechanisms (Volonteri, 2010). The mass of the black holes observed in the universe ranges from a few solar masses for the stellar mass black holes to billions of solar masses for the supermassive black holes, which usually reside at the cores of massive galaxies. There are various methods in use for the calculation of these masses. The mass estimates for the stellar mass black holes can be done by observing the motion of the companion star(s) when they are in a binary or multiple star system (e.g. Remillard and McClintock, 2006). Whereas, the mass of supermassive black holes can be calculated by following the dynamics of stars around them (e.g. Reid and Brunthaler, 2004; Boehle et al., 2016) or the dynamics of gas being accreted to them with techniques like reverberation mapping (e.g. Hoormann et al., 2019). There are two more classes of black holes as per our current state of knowledge: intermediate-mass black holes with masses in the range $M_{BH} = 10^2 - 10^5 M_\odot$ (see e.g. Greene, Strader, and Ho, 2020 for a review) and primordial black holes that might have formed in the early stages of the universe and may have masses in any range (see e.g. Escrivà, Kuhnel, and Tada, 2022 for a review).

Accretion is a universal phenomenon which is observed along with different classes of compact objects including white dwarfs, neutron stars and at all the mass scales of black holes. For instance, gamma-ray bursts (GRBs) are powered by accretion onto stellar mass black holes and active galactic nuclei (AGNs) are powered by accretion onto supermassive black holes. We focus on accretion onto black hole sources in particular which produce magnificent observational effects as described. The theory of black holes is very briefly summarized here.

1.1.1 Black holes

Black holes are regions in space and time where gravity is so strong that even light can not escape from their gravitational effect. It was in 1784 that the initial idea of such objects was put forth by an English natural philosopher John Michell (Michell, 1784). The first proper mathematical description and thus the theoretical prediction that black holes can exist was put forth when Albert Einstein developed his general theory of relativity (GR) in 1915 (Einstein, 1916). Until his theory, space and time were considered independent entities and gravity was considered an attractive force between massive particles according to the Newtonian theory of gravity existed at that time. This notion was changed according to GR which interprets gravity as a geometric property of space and time or "spacetime" and is directly related to the mass and energy present in it. The Einstein field equations, which are a set of partial differential equations, specify the relation between these quantities (e.g. as in Misner, Thorne, and Wheeler, 1973)

$$G_{\mu\nu} = R_{\mu\nu} - \frac{1}{2} R g_{\mu\nu} = \frac{8\pi G}{c^4} T_{\mu\nu} \tag{1.1}$$

where $G_{\mu\nu}$ is the Einstein tensor, a combination of the Ricci tensor $R_{\mu\nu}$ and the metric $g_{\mu\nu}$, which contains information about the geometry of the spacetime. The sub-indices $\mu\nu$ denote the coordinates of the spacetime. R is the scalar curvature and $T_{\mu\nu}$ is the stress-energy tensor which holds information about the distribution of mass and energy.

Black holes are solutions to Einstein field equations. The first exact solution to the field equations was found by Karl Schwarzchild just the next year after the original paper on GR was published (Schwarzschild, 1916). It describes the spacetime in the exterior of a static, spherically symmetric, uncharged mass in vacuum. The line element in this metric is given in spherical coordinates by

$$ds^2 = \sum_{\mu\nu} g_{\mu\nu} dx^\mu dx^\nu = dt^2 - dr^2 - r^2 d\theta^2 - r^2 \sin^2\theta d\phi^2. \tag{1.2}$$

In the Schwarzchild spacetime, the mass M of the black hole sets the size of the system and thus the characteristic space and time scales. For instance, the length is characterised by the gravitational radius

$$r_g = \frac{GM}{c^2} = 1.477 \left(\frac{M}{M_\odot}\right) \text{km} \tag{1.3}$$

and time by

$$t_g = \frac{GM}{c^3} = 4.923 \times 10^{-6} \left(\frac{M}{M_\odot}\right) \text{s}. \tag{1.4}$$

The Schwarzchild solution is a useful approximation for the study of slowly rotating astrophysical black holes. There are two interesting locations in Schwarzchild spacetime. The first is the physical singularity at $r = 0$, where the spacetime is no longer well-defined. The second is the event horizon, which hides this singularity, below which the escape velocity exceeds the speed of light and thus no information from within this boundary cannot reach an external observer (Finkelstein, 1958; Bambi, 2018). The radius of the event horizon is given by the Schwarzchild radius $r_s = 2r_g$. Any object with a physical radius smaller than its Schwarzchild radius will be a black hole. Other exact solutions for the Einstein field equations followed later after the Schwarzchild solution, for example, according to Hans Reissner (Reissner, 1916) and Gunnar Nordström (Nordström, 1918) for a static, spherically symmetric, charged black hole. However, the actual nature of these solutions was not clearly understood at the initial times. It was only in 1958, David Finkelstein established the importance of the event horizon and its physical significance.

In 1963, Roy Kerr found another solution for the Einstein field equations for an axisymmetric, rotating, uncharged mass in vacuum, now known as the Kerr solution (Kerr, 1963). The line element in Kerr metric written in Boyer-Lindquist coordinates (Boyer and Lindquist, 1967) is given by

$$\begin{aligned} ds^2 = &- \left(1 - \frac{2Mr}{\Sigma}\right) dt^2 - \left(\frac{4Mar\sin^2\theta}{\Sigma}\right) dt d\phi + \frac{\Sigma}{\Delta} dr^2 + \Sigma d\theta^2 \\ &+ \sin^2\theta \left(r^2 + a^2 + \frac{2Ma^2 r \sin^2\theta}{\Sigma}\right) d\phi^2, \end{aligned} \tag{1.5}$$

where $\Delta = r^2 - 2Mr + a^2$ and $\Sigma = r^2 + a^2\cos^2\theta$. This solution for a spinning black hole depends only upon the mass M and angular momentum J of the object. The parameter a quantifies the spin of the black hole, defined by the dimensionless expression

$$\frac{a}{M} = \frac{Jc}{GM^2} \tag{1.6}$$

which represents the angular momentum per unit mass of the black hole. In the limit when $a \to 0$, the Schwarzchild solution is obtained. The size of the horizon of a Kerr black hole is given by

$$r_{\mathrm{H}\pm} = M \pm \sqrt{M^2 - a^2} \tag{1.7}$$

where $r_{\mathrm{H}+}$ represents the outer horizon, which is physically identical to the event horizon in the Schwarzchild case. It can be seen from this equation that only values of $\mid a \mid \leq M$ are permissible for a horizon to exist around the singularity. This is known as the cosmic censorship conjecture whose violation would result in a naked singularity or a singularity without an event horizon. Another boundary of importance in the case of a Kerr black hole is its ergosphere which lies between the outer horizon $r_{\mathrm{H}+}$ and a surface at $r = r_{\mathrm{E}} = M + \sqrt{M^2 - a^2 \cos^2\theta}$. The boundary of the ergosphere is a rather flattened sphere, than a perfect one, touching the event horizon at the poles. All inertial frames co-rotate with the rotating spacetime inside this boundary which is known as frame dragging. Figure 1.1 shows a schematic of the important boundaries in the Kerr metric. In 1971, Roger Penrose formulated a process in which it is possible to extract energy from the rotation of a Kerr black hole from within the ergosphere, now known as the Penrose process (Penrose and Floyd, 1971). Other exact solutions for the Einstein-Maxwell field equations are also known e.g. the Kerr-Newman solution for an electrically charged rotating mass in vacuum (Newman et al., 1965).

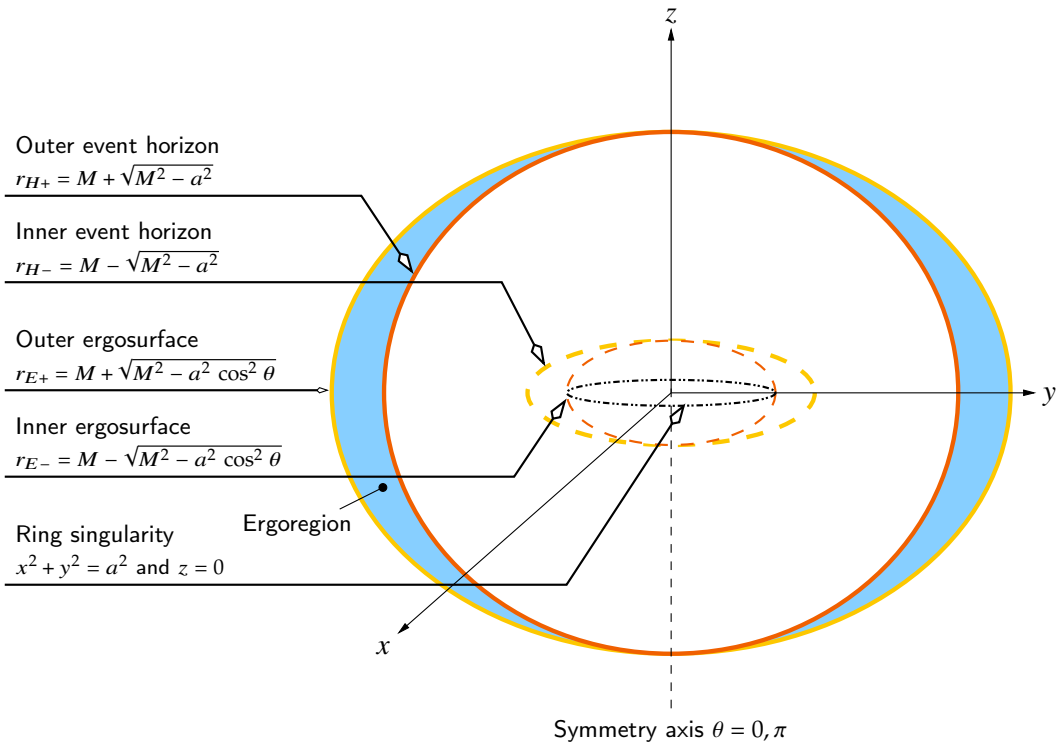

FIGURE 1.1: Schematic location of the horizons, ergosurfaces, and curvature singularity in the Kerr spacetime (Figure credit: Visser, 2007; labels modified to match with present text).

1.1.2 Astrophysical black holes

After remaining many decades as just theoretical curiosities, the existence of black holes in nature was considered to explain the observed properties of quasars in the 1960s. When they were initially discovered in the second half of the 20th century, such sources were called quasars by the contraction of the terms "quasi-stellar radio sources" owing to the unknown physical origin of the radio emission observed from them. Their extremely high luminosity ($\sim 10^{46} - 10^{47}$erg s^{-1}), fast variability in the observed flux, and cosmologically red-shifted emission lines pointed towards sources of extra-galactic origin confined to a very compact region (of about 1 AU). The first proposal that quasars are powered by the accretion of matter onto supermassive black holes was made independently by Yakov Zel'dovich and Edwin Salpeter in 1964 (Zel'dovich, 1964; Salpeter, 1964). Later it turned out that quasars are active galactic nuclei of very high luminosity with a supermassive black hole at their center. Cygnus X-1 which was discovered in 1964 (Bowyer et al., 1965) and found to have a companion star in 1974 (Bolton, 1972; Webster and Murdin, 1972) is one of the brightest X-ray sources in the sky. When the mass of the compact object in this source was estimated from the orbital motion of the companion star, it turned out to be much higher than the maximum possible mass for a neutron star. Thus the compact object in Cygnus X-1 was identified as the first stellar-mass black hole candidate (Bambi, 2018). Later it became apparent through observations of stellar motions that our own galactic nucleus hosts a supermassive compact object at its center, which most astronomers consider as a black hole (Eckart and Genzel, 1997; Ghez et al., 1998). The object is called Sagittarius A* (Sgr A*) and its presence is further confirmed by the recent radio images of the black hole shadow (shown in Figure 1.2) obtained by very-long-baseline interferometry (VLBI) imaging techniques (Event Horizon Telescope Collaboration et al., 2022b). By astrophysical considerations, black holes in nature are expected to possess effectively negligible electric charge and should therefore be completely describable by only their mass and angular momentum or in other words by the Kerr solution. Having described the basics about black holes, let us move on to a brief description of accretion in astrophysics.

1.2 Accretion processes in astrophysics

Accretion is the key phenomenon in driving the formation of young stars and planetary systems, influencing the evolution of many multiple star systems, and also the evolution of galaxies. All the observations we conduct in astronomy except the newly developed paradigm of gravitational waves require the emission of energy in the form of electromagnetic radiation. The emission of electromagnetic radiation can be driven by various mechanisms which considerably differ in their efficiency and availability. The efficiency can be characterized in simple terms by the energy output we get from a unit of fuel and it is convenient to use a dimensionless convention based on Einstein's principle of mass-energy equivalence ($E = mc^2$):

$$\eta = \frac{\Delta E}{mc^2} \tag{1.8}$$

where ΔE is the energy liberated in the process and m is the rest mass of the fuel material used. The common processes available in nature for energy liberation include chemical reactions which depend on electromagnetic interactions, nuclear reactions which depend on the strong force, and gravitational interactions which

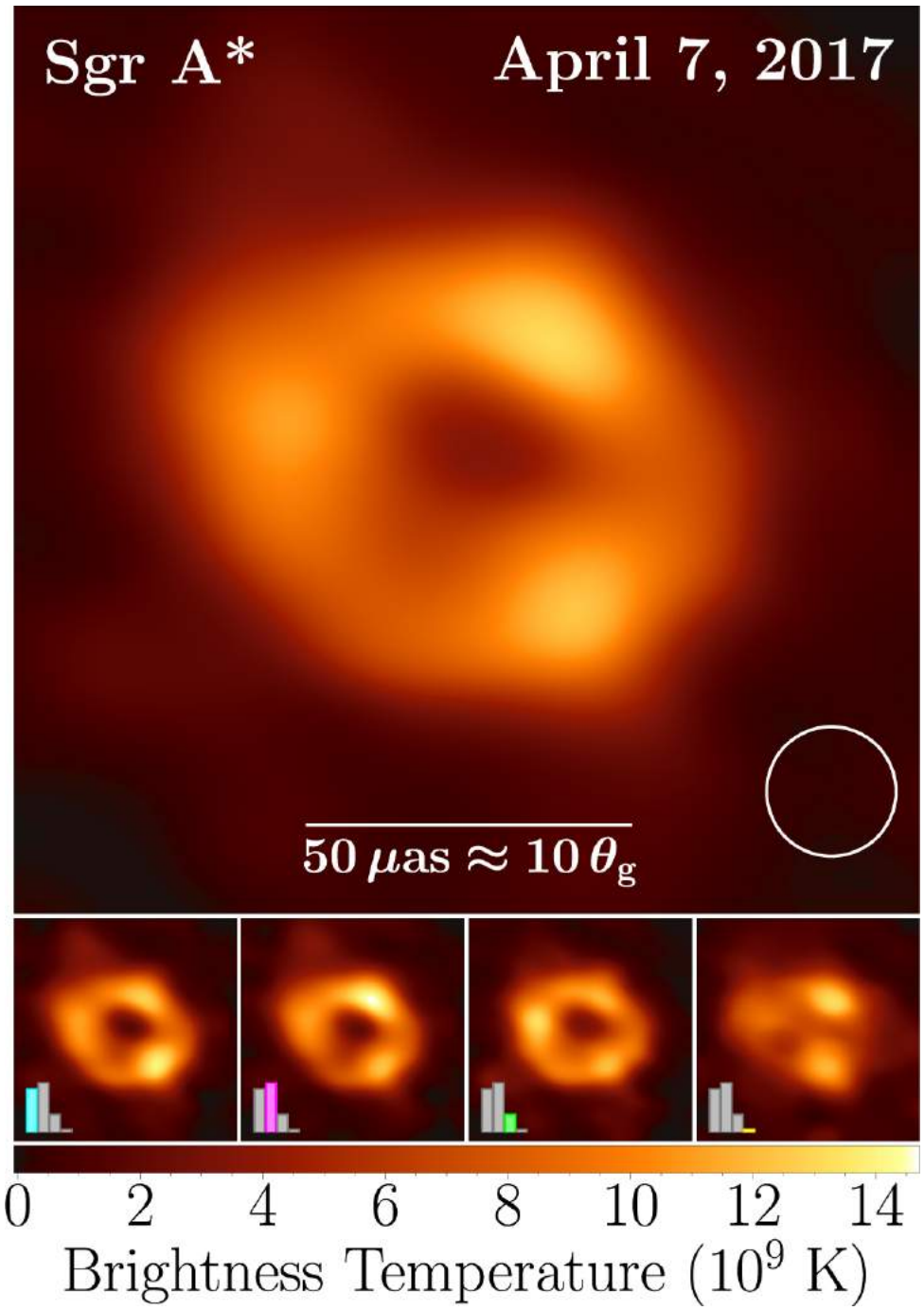

FIGURE 1.2: Representative image of Sgr A* shadow obtained by the EHT collaboration from observations in 2017. The image shown is an average from the different reconstruction methodologies and reconstructed morphologies (Image credit: Event Horizon Telescope Collaboration et al., 2022b). This further confirms the existence of a supermassive black hole in the center of our own galaxy Milky Way.

result in the release of gravitational potential energy. In the units mentioned above, the chemical processes have an efficiency in the range of $\sim 10^{-9} - 10^{-10}$ and the nuclear reactions which power the stars have an efficiency in the order of $\sim 10^{-3}$. On the other hand, the available gravitational potential energy to be converted to heat when a small body of mass m falls down from infinity to another larger body of mass M having radius R is given by GMm/R and thus the possible efficiency is $\eta = \frac{GMm}{Rmc^2} = \frac{GM}{Rc^2}$. If we use the Schwarzchild radius r_s in place of R in this expression we get an efficiency of 0.5 for a gravitating body of mass M[2]. Even when a fraction of this heat is converted to radiation, by various radiation mechanisms, the efficiency is still higher than other processes. So accretion is an extremely efficient process in terms of energy output. Now let us move on to a more precise estimation of the efficiency considering the relativistic case.

1.2.1 Efficiency of accretion onto a Kerr black hole

Most astrophysical black holes very probably possess nonzero angular momentum and thus the Kerr metric is the most suitable one to describe such realistic systems (Bardeen, 1970). Now to be more precise about the possible accretion power in black hole sources, let us have an estimate of efficiency in the relativistic case considering the motion of a test particle in Kerr metric (Bardeen, Press, and Teukolsky, 1972).

Test particles move along geodesics in a given spacetime geometry. A geodesic in affine geometry is a curve $x^\mu = x^\mu(\lambda)$ which parallel transports its tangent vector $u^\alpha = dx^\alpha/d\lambda$. Here λ is an affine path parameter, normalized to give proper time along time-like geodesics, and we will now use an over-dot to denote ordinary differentiation with respect to λ. Now the geodesic equations can be obtained by using the variational principle

$$\delta \int L d\lambda = 0, \tag{1.9}$$

where the Lagrangian is given by

$$L = \frac{1}{2} g_{\alpha\beta} \dot{x}^\alpha \dot{x}^\beta \tag{1.10}$$

and the conjugate momenta corresponding to the coordinates x^α can be obtained in the usual way $p_\alpha = \frac{\partial L}{\partial \dot{x}^\alpha}$ (Carter, 1968; Rezzolla, 2016).

Now, let us try to follow the motion of a test particle with mass m in the equatorial plane of the black hole spin. We set $\theta = \pi/2$ in equation 1.5 and then we can write the Lagrangian as

$$2L = -\left(1 - \frac{2M}{r}\right)\dot{t}^2 - \frac{4aM}{r}\dot{t}\dot{\phi} + \frac{r^2}{\Delta}\dot{r}^2 + \left(r^2 + a^2 + \frac{2Ma^2}{r}\right)\dot{\phi}^2. \tag{1.11}$$

Now, we can obtain the following first integrals corresponding to the cyclic coordinates t and ϕ

$$p_t = \frac{\partial L}{\partial \dot{t}} = \text{constant} = -E \tag{1.12}$$

and

[2]It is the efficiency of the accretion process when an infalling body of mass m hits the surface of a body with mass M at its Schwarzchild radius. This initial calculation is intended to give a rough estimate of the possible range of efficiency of accretion and this formula is not directly applicable in the case of a black hole as it does not have a clearly defined surface.

$$p_\phi = \frac{\partial L}{\partial \dot{\phi}} = \text{constant} = l \tag{1.13}$$

with E and l representing the energy and angular momentum respectively of a test particle moving along the given geodesic.

Also, we can obtain the geodesic equations from 1.11 as

$$\dot{t} = \frac{(r^3 + a^2 r + 2Ma^2)E - 2aMl}{r\Delta} \tag{1.14}$$

and

$$\dot{\phi} = \frac{2aME + (r - 2M)l}{r\Delta}. \tag{1.15}$$

We can also write a third integral of motion from 1.11 as follows

$$r^3\dot{r}^2 = E^2(r^3 + a^2 r + 2Ma^2) - 4aMEl - l^2(r - 2M) - m^2 r\Delta = \tilde{V}(E, l, r) \tag{1.16}$$

where we can regard $\tilde{V}$ as an effective potential for radial motion in the equatorial plane. Circular orbits occur where $\dot{r} = 0$, which requires $\tilde{V} = 0$ or $\frac{\partial \tilde{V}}{\partial r} = 0$. These equations can be thus solved for E and l to obtain

$$E/m = \tilde{E} = \frac{r^2 - 2Mr \pm a\sqrt{Mr}}{r(r^2 - 3Mr \pm 2a\sqrt{Mr})^{1/2}} \tag{1.17}$$

and

$$l/m = \tilde{l} = \pm\frac{\sqrt{Mr}(r^2 \mp 2a\sqrt{Mr} + a^2)}{r(r^2 - 3Mr \pm 2a\sqrt{Mr})^{1/2}}, \tag{1.18}$$

where the upper sign corresponds to co-rotating orbits and the lower sign corresponds to counter-rotating ones. Circular orbits then exist from infinity all the way down to the limiting radius where the energy diverges, i.e. when the denominator of equation 1.17 vanishes. We find the photon orbit, solving for the resulting equation as

$$r_{\text{ph}} = 2M\left(1 + \cos\left(\frac{2}{3}\cos^{-1}\left(\pm\frac{a}{M}\right)\right)\right). \tag{1.19}$$

For $a = 0$, $r_{\text{ph}} = 3M$ and for $a = M$, $r_{\text{ph}} = M$ (for prograde case) and $r_{\text{ph}} = 4M$ (for retrograde case). So this orbit can even be at the horizon for the co-rotating particles in the "extremal" Kerr case (with $a = M$). Not all circular orbits are bound for $r > r_{\text{ph}}$ also. Unbound circular orbits possess $E/m > 1$ and a particle in such an orbit will escape to infinity on an asymptotically hyperbolic orbit upon an infinitesimal outward perturbation.

Bound orbits exist for $r > r_{\text{mb}}$, where r_{mb} denotes the radius of the marginally bound circular orbit with $E/m = 1$ and is given by

$$r_{\text{mb}} = 2M \mp a + 2\sqrt{M(M \mp a)}. \tag{1.20}$$

For a bound orbit to be stable, it needs to satisfy the condition $\frac{\partial^2 \tilde{V}}{\partial r^2} \leq 0$. Also using 1.17, we can write $1 - \left(\frac{E}{m}\right)^2 \geq \frac{2}{3}\frac{M}{r}$.

For each value of black hole spin a/M, now we have the solution for $r_{\rm ms}$, the radius of the marginally stable circular orbit given by

$$r_{\rm ms,\pm} = M\left[3 + Z_2 \mp \sqrt{(3 - Z_1)(3 + Z_1 + 2Z_2)}\right] \tag{1.21}$$

with

$$Z_1 = 1 + (1 - a^2)^{1/3}\left[(1 + a)^{1/3} + (1 - a)^{1/3}\right], \tag{1.22}$$

$$Z_2 = \sqrt{3a^2 + Z_1^2}. \tag{1.23}$$

The marginally stable circular orbit corresponds to the innermost stable circular orbit (or ISCO) as well. Let us now calculate some specific values for the marginally stable radii

$$r_{\rm ms} = \begin{cases} 6M \text{ for } a/M = 0, \\ M \quad \text{for } a/M = 1 \text{ (prograde)}, \\ 9M \text{ for } a/M = -1 \text{ (retrograde)}. \end{cases} \tag{1.24}$$

Now for the moment, let us consider the Schwarzchild case where stable circular orbits exist down to $r = 3M$ for photons ($r_{\rm ph}$). This is the limit at which the denominator of the equation

$$\tilde{E}^2 = \frac{(r - 2M)^2}{r(r - 3M)} \tag{1.25}$$

goes to zero ($\tilde{E} = E/m \to \infty$). Particle circular orbits are stable down to $r_{\rm ISCO} = 6M$ which gives $\tilde{E}_{ISCO} = \sqrt{8/9}$. Thus the binding energy per unit mass of a particle in the last stable circular orbit in the Schwarzchild case is given by 1.25 as

$$\tilde{E}_{bind} = 1 - \sqrt{8/9} \approx 5.72\% \tag{1.26}$$

This is the fraction of the rest-mass energy liberated when a particle which was initially at rest at infinity spirals inwards to a non-rotating black hole to the innermost stable circular orbit, and then plunges and disappears into the black hole.

Now let us consider the Kerr black hole. The binding energy of the marginally stable circular orbit can be computed by using the equations 1.17 and 1.21 and we find the expression

$$\frac{a}{M} = \mp\frac{4\sqrt{2}(1 - \tilde{E}^2)^{1/2} - 2\tilde{E}}{3\sqrt{3}(1 - \tilde{E}^2)}. \tag{1.27}$$

The value of $\tilde{E}$ decreases from $\sqrt{8/9}$ in the Schwarzchild case to $\sqrt{1/3}$ for the prograde orbits and increases to $\sqrt{25/27}$ for the retrograde orbits in the Kerr case. Thus the binding energy $(1 - \tilde{E}_{ms})$ on the (prograde) marginally stable circular orbit in the case of a maximally rotating Kerr black hole is

$$\tilde{E}_{bind} = 1 - \sqrt{1/3} \approx 42.3\% \tag{1.28}$$

of the rest mass energy. So this is the energy liberated when a particle spirals in towards a Kerr black hole through a succession of almost circular equatorial orbits. This shows the huge efficiency of accretion in the probably more realistic case of rotating black holes.

1.2.2 Eddington luminosity

All most luminous sources observed in astronomy are powered by the process of accretion. It is also a fact established by astronomers as a result of decades of instrumental development and observations.

Luminosity is the observed physical property which can be used to quantify the radiation produced in the accretion disks. In simple terms, the luminosity of a source depends on the efficiency of the energy conversion process η and the mass accretion rate $\dot{M}$ onto it, $L = \eta \dot{M} c^2$. As photons carry momentum which can exert pressure, there is a maximum possible luminosity for a given spherical distribution of mass at which the inward gravity is able to balance the outward radiation pressure. The limit of luminosity for a stationary, spherically symmetric, fully ionized hydrogen gas cloud is given by the Eddington luminosity

$$L_{\rm Edd} = GM \frac{4\pi m_p c}{\sigma_T} = 1.26 \times 10^{38} \frac{M}{\rm M_\odot} {\rm ergs}^{-1} \tag{1.29}$$

where M is the mass of the gravitating body, m_p is the mass of the proton and σ_t is the Thompson scattering cross-section for the electron. Thus the maximum possible luminosity of a source in hydrostatic equilibrium is its Eddington luminosity and there could be radiation pressure-driven outflows if it exceeds this limit. But since the accretion flow is not always spherical and there could be other additional stresses in the disk accretion along with the gravity, the actual luminosity of an object can be higher than this limit and then it is said to radiate at super-Eddington luminosity.

1.2.3 Spherical accretion

To understand the dynamics of accretion onto a central object we start with a classical example having the highest symmetry, the spherical accretion in the simple Newtonian regime. We may not have symmetry in the flow in many cases, for example when a stream of matter hits the surface of a star and also relativistic considerations are often necessary. On the other hand, the spherical accretion is a good approximation in the case of many realistic systems such as the hot accretion flows onto Sgr A* and advection-dominated accretion flows (ADAFs).

The accreting matter is usually not very dense but highly ionized being a mixture of electrons and ions. The particles in this case may exchange energy between them through scattering, that is through Coulomb interactions. If these interactions are frequent, the matter in the flow can be characterized by its density, pressure and temperature or in other words, the hydrodynamical approximation, as a starting point. We now describe the basic assumptions to consider for a hydrodynamic description of the flow.

The hydrodynamic equations read as follows. The first one comes from the fact that the rate of change of fluid mass inside a volume equals the net rate of fluid flow into the volume (i.e. mass conservation), often termed the continuity equation

$$\frac{\partial \rho}{\partial t} + \nabla.(\rho \boldsymbol{u}) = 0. \tag{1.30}$$

The second one which is the equation of motion comes from the fact that the rate of change of total fluid momentum in a volume equals the sum of forces acting on it (i.e. momentum conservation). For an inviscid fluid, it is called the Euler's equation

$$\rho \left(\frac{\partial \boldsymbol{u}}{\partial t} + (\boldsymbol{u}.\nabla)\boldsymbol{u} \right) = -\nabla P + \boldsymbol{f}. \tag{1.31}$$

The third one comes from the conservation of energy. For this, we consider a fluid element having two possible forms of energy. First, the kinetic energy per unit volume $\frac{1}{2}\rho u^2$ and second the internal energy per unit volume $\rho\epsilon$, where ϵ is the internal energy per unit mass which depends on the temperature T of the gas. For a monoatomic (Hydrogen) gas with only three translational degrees of freedom, the internal energy per unit mass amounts to

$$\epsilon = \frac{3}{2} k_B T/\mu m_H \tag{1.32}$$

according to the equipartition theorem of elementary kinetic theory, where m_H is the mass of the hydrogen atom. The energy equation of the gas can then be written in the form

$$\frac{\partial}{\partial t}\left(\frac{1}{2}\rho u^2 + \rho\epsilon\right) + \nabla.\left[\left(\frac{1}{2}\rho u^2 + \rho\epsilon + P\right)\boldsymbol{u}\right] = \boldsymbol{f}.\boldsymbol{u} - \nabla.\boldsymbol{F}_{rad} - \nabla.\boldsymbol{q}. \tag{1.33}$$

Here ρ is the fluid density, $\boldsymbol{u}$ is the fluid velocity field, P is the pressure and $\boldsymbol{f}$ is the force per unit volume of the fluid. $\boldsymbol{F}_{rad}$ is the radiation flux vector and the term $-\nabla.\boldsymbol{F}_{rad}$ gives the rate at which radiant energy is lost by emission, or gained by absorption per unit volume of the gas. $\boldsymbol{q}$ is the conductive flux of heat, and this measures the rate at which random motions transport the thermal energy in the gas. For an ionized gas obeying the requirement that the mean free path $\lambda \ll T/\mid \nabla T \mid$, standard kinetic theory gives the value $q \cong -10^{-6}\, T^{5/2}\, \nabla T$ erg s^{-1} cm^{-2}. In many astrophysically relevant cases, the temperature gradient in the gas is small enough that this term can be omitted from the energy equation (Frank, King, and Raine, 2002).

In addition, an equation of state relates the pressure of the gas to the density and temperature. Even though astrophysical fluids take various configurations including degenerate matter in neutron stars and white dwarfs or partial ionization states which change the mean molecular weights, we can in most cases take an approximation of an ideal gas. The equation of state for an ideal monoatomic gas can be written in the form

$$P = \rho k_B T/\mu m_p \tag{1.34}$$

where $m_p \sim m_H$ is the proton mass, and μ is the mean molecular weight.

Now let us consider steady flows, for which the time derivatives become zero. Also let us assume that there are no energy losses in the system, through radiation or thermal conduction, and thus the adiabatic case. Then the equations 1.30, 1.31 and 1.33 become

$$\nabla.(\rho\boldsymbol{u}) = 0, \tag{1.35}$$

$$\rho(\boldsymbol{u}.\nabla)\boldsymbol{u} = -\nabla P + \boldsymbol{f} \tag{1.36}$$

$$\nabla.\left[\left(\frac{1}{2}\rho u^2 + \rho\epsilon + P\right)\boldsymbol{u}\right] = \boldsymbol{f}.\boldsymbol{u}. \tag{1.37}$$

Using equations 1.35 and 1.36 in 1.37 we can write

$$\rho\boldsymbol{u}.\nabla\left(\frac{1}{2}u^2\epsilon + P/\rho\right) = \boldsymbol{f}.\boldsymbol{u} \tag{1.38}$$

and in turn

$$\rho \boldsymbol{u}.\nabla(\epsilon + P/\rho) = \boldsymbol{u}.\nabla P. \tag{1.39}$$

Expanding and rearranging this gives

$$\boldsymbol{u}.(\nabla\epsilon + P\nabla(1/\rho))) = 0. \tag{1.40}$$

From the definition of the gradient operator and Equation 1.40, one can write

$$\mathrm{d}\epsilon + P\mathrm{d}(1/\rho) = 0. \tag{1.41}$$

Now using the expressions for internal energy per unit mass (1.32) and the ideal gas law (1.34) we can write

$$\frac{3}{2}\mathrm{d}T + \rho T\mathrm{d}(1/\rho) = 0 \tag{1.42}$$

from which we can write $T^{3/2}\rho^{-1}$ = constant or equivalently

$$P\rho^{-5/3} = \text{constant}. \tag{1.43}$$

This is the equation of state for a non-relativistic adiabatic gas. For the relativistic case, this becomes $P\rho^{-4/3}$ = constant. For a more general (polytropic) case, for example, if our gas is not monoatomic, we can write this as

$$P\rho^{-\gamma} = \text{constant}, \tag{1.44}$$

where γ is the adiabatic index and for an isothermal flow $\gamma = 1$.

Now let us consider a basic accretion problem in which a star of mass M and radius R is embedded in an interstellar medium with uniform density $\rho_{out} = \rho$ and temperature $T_{out} = T$. We venture to have an estimate of the accretion rate of the interstellar matter onto the star. The problem was originally solved by Herman Bondi in 1952 (Bondi, 1952) and a brief summary of it follows here. For now, in such a consideration, it is assumed that the angular momentum, magnetic field strength and bulk motion of the interstellar medium are negligible.

Before going into the details, let us introduce the concept of sound speed $c_s = \left(\frac{dP}{d\rho}\right)^{1/2}$. It is the speed at which the pressure differences travel through a gas and it limits the rate at which the gas responds to the pressure changes. Now the pressure gradient (for a polytope) can be expressed in terms of the density gradient

$$\frac{dP}{dr} = \frac{dP}{d\rho}\frac{d\rho}{dr} = c_s^2\frac{d\rho}{dr}. \tag{1.45}$$

For solving the problem, we assume a steady flow with spherical symmetry. In this case, the gas velocity has only the radial component $u = u_r$ and we assume this value as negative for the inward flow. The continuity equation (1.35) (in spherical coordinates) now reduces to

$$\frac{1}{r^2}\frac{d}{dr}(r^2\rho u) = 0 \tag{1.46}$$

or equivalently $r^2\rho u$ = constant. Now we can introduce the flow constant, the mass accretion rate $\dot{M}$, in the traditional form

$$\dot{M} = 4\pi r^2 \rho(-u) \tag{1.47}$$

since $\rho(-u)$ is the inward flux of the gas. Now the Euler equation (1.36) has only one component for the external force $\boldsymbol{f}$, which is from gravity which only has a radial component

$$f_r = \frac{-GM\rho}{r^2} \tag{1.48}$$

so that the equation 1.31 finally becomes

$$u\frac{du}{dr} + \frac{1}{\rho}\frac{dP}{dr} + \frac{GM}{r^2} = 0 \tag{1.49}$$

or equivalently

$$u\frac{du}{dr} + \frac{1}{\rho}\frac{d\rho}{dr}c_s^2 + \frac{GM}{r^2} = 0. \tag{1.50}$$

From the continuity equation (1.46) we can write

$$\frac{1}{\rho}\frac{d\rho}{dr} = -\frac{1}{ur^2}\frac{d}{dr}(ur^2) \tag{1.51}$$

and thus we can write equation 1.50 as

$$u\frac{du}{dr} - \frac{c_s^2}{ur^2}\frac{du}{dr} + \frac{GM}{r^2} = 0 \tag{1.52}$$

or equivalently as

$$\frac{d}{dr}(u^2) = \frac{-\frac{GM}{r^2}\left[1 - \left(\frac{2c_s^2 r}{GM}\right)\right]}{\frac{1}{2}\left(1 - \frac{c_s^2}{u^2}\right)}. \tag{1.53}$$

We can notice immediately from this equation that when the local velocity crosses the local sound speed, $u^2 = c_s^2$, the denominator of the right-hand side expression becomes zero and the equation has a critical point. We can assume that the matter is at rest at infinity with a nonzero temperature so that u^2 is slowly rising inwards. In this case, the velocity diverges when it approaches the sound speed (c_s) in the medium. So for the supersonic motion to be possible, there should be a transition between subsonic to supersonic velocities in the medium as we approach the star. For this to be possible, the numerator in the right-hand side of the equation should be zero at the radius where the local velocity (u) becomes equal to the local sound speed (c_s) and this radius is called the sonic radius (r_s). Thus two conditions are to be satisfied at the sonic radius,

$$u^2 = c_s^2 \tag{1.54}$$

and

$$r_s = \frac{GM}{2c_s^2(r_s)}. \tag{1.55}$$

This is the radius around the star which divides the flow into two parts namely: (a) the outer subsonic flow with $u^2 < c_s^2$ and (b) the inner supersonic flow with $u^2 > c_s^2$. The location where this radius is located is called the sonic point where the velocity of the flow reaches the local sound speed (c_s).

Now let us try to have an estimate of the accretion rate in this case. Let us start with integrating equation 1.49 and by using equation 1.44, we get (for $\gamma \neq 1$)

$$\frac{u^2}{2} + \frac{K\gamma}{\gamma - 1}\rho^{\gamma-1} - \frac{GM}{r} = \text{constant}, \tag{1.56}$$

where K is constant.

Using again the concept of sound speed (c_s), we get the Bernoulli integral

$$\frac{u^2}{2} + \frac{c_s^2}{\gamma - 1} - \frac{GM}{r} = \text{constant}. \tag{1.57}$$

Now using the boundary condition that $u^2 \to 0$ as $r \to \infty$, the constant evaluates to $c_s^2(\infty)/(\gamma - 1)$, where $c_s(\infty)$ is the sound speed in the gas at infinity. Now using also the ideas from equations 1.54 and 1.55, we can write

$$c_s^2(r_s)\left(\frac{1}{2} + \frac{1}{\gamma - 1} - 2\right) = \frac{c_s^2(\infty)}{\gamma - 1} \tag{1.58}$$

or

$$c_s(r_s) = c_s(\infty)\left(\frac{2}{5 - 3\gamma}\right). \tag{1.59}$$

From this, we can also write the expression for sonic radius

$$r_s = \frac{GM(5 - 3\gamma)}{4c_s^2(\infty)}. \tag{1.60}$$

and the Bondi radius

$$r_B = \frac{GM}{c_s^2(\infty)}. \tag{1.61}$$

Now we can write the expression for Bondi accretion rate using equation 1.47 as

$$\dot{M}_B = 4\pi G^2 M^2 \frac{\rho(\infty)}{c_s^3(\infty)}\left(\frac{2}{5 - 3\gamma}\right)^{\frac{5-3\gamma}{2(\gamma-1)}}. \tag{1.62}$$

For partially ionized interstellar medium, we have a typical value for $\gamma = 1.4$, then the factor $[2/(5 - 3\gamma)]^{(5-3\gamma)/2(\gamma-1)}$ has a value 2.5.

We have seen that the accretion flows must be transonic, that is they have to transition from a subsonic to supersonic velocity, in order to satisfy the boundary conditions near a black hole. In spherical Bondi accretion, we have one sonic point where this transition occurs.

In many realistic scenarios, matter often possesses additional angular momentum which makes the regime of simple spherically symmetric accretion not really applicable. Having described the basics of spherically symmetric accretion let us move on to the case of rotating flows around a central object, which is closer to real flows. In such flows, the mechanisms which transport angular momentum outwards in the material play an important role in its evolution as they are crucial in sustaining the flow.

1.2.4 Accretion disks

Accretion disks are flattened astrophysical objects comprising rapidly rotating material around a central gravitating object. In simple terms, the matter possessing an initial velocity around a massive object in space eventually assumes a flattened disk shape in order to conserve angular momentum and minimize collisions between the constituent particles. The angular momentum of the material in these accretion disks is gradually transported outwards by various dissipative processes, causing the matter to spiral down into the central compact object, converting its gravitational energy into heat and then by various radiative processes releasing this energy which is observed by us from Earth (Abramowicz and Fragile, 2013).

Keplerian disk

We will now discuss the basics of the standard accretion disk theory with the description of a Keplerian disk. A disk of material that obeys Kepler's laws of motion due to the existence of a massive central object is known as a Keplerian disk. In such a disk, the velocity of the material at a distance r from the central object is proportional to $r^{-1/2}$ by the standard Newtonian theory. Now the accretion of a material of mass m through a Keplerian disk from a large distance $r_{\rm out}$ to an inner radius $r_{\rm in}$ requires the particle to give a huge amount of energy (dependent on the efficiency of the mechanism) $\sim \eta mc^2$, as we have discussed earlier. That is, the material has to give up its angular momentum which amounts to $\sim \sqrt{GMr_{\rm out}}$. The viscous stresses within the fluid can support this process. It is worth noting that the stresses resulting from ordinary molecular viscosity are hugely insufficient in the context of astrophysical accretion disks. Instead, stresses resulting from turbulence and other physical mechanisms can act like an effective viscosity in the astrophysical scenario.

In a geometrically thin accretion disk, the radial pressure gradients are ignorable. Let us assume that the disk is axially symmetric. In the cylindrical polar coordinates (R, ϕ, z), we can to introduce a new quantity Σ which is the disk surface density

$$\Sigma(R,t) = \int_{-H}^{+H} \rho(R,z,t)dz. \tag{1.63}$$

where H is the disk scale height. The fluid velocity $\boldsymbol{u}$ varies little with z if the disk has a limited vertical extent, and we may integrate the fluid equations over z with $\boldsymbol{u}$ evaluated at the midplane $z = 0$. The radial force equation then yields the centrifugal balance,

$$R\Omega^2(R) = \frac{GM}{R^2}, \tag{1.64}$$

where $\Omega(R)$ is the local angular velocity at the radius R in the disk and M is the mass of the central object. Also, we have assumed that the orbit speed $R\Omega$ much exceeds the thermal speed $v_T \equiv (k_B T/m)^{1/2}$ in the midplane of the disk for us to ignore the contribution of the pressure gradient in the radial force balance, i.e. $R\Omega \gg v_T$. Since the disk has a characteristic scale height $H = v_T/\Omega$, this approximation also holds that the disk is indeed geometrically thin, $H \ll R$.

Also, in equation 1.64, we have assumed that the mass of the disk is much smaller than the mass M of the central object,

$$2\pi \int_{R_i}^{R_o} \Sigma R dR \ll M, \tag{1.65}$$

where R_i and R_o are the radii of the inner and outer edges of the disk, respectively. When equation 1.65 holds, equation 1.64 implies that the circular frequency Ω satisfies the Kepler's third law, i.e. $\Omega \propto R^{-3/2}$. A Keplerian disk like this possesses a shear which amounts to

$$R\frac{d\Omega}{dR} = -\frac{3}{2}\Omega. \tag{1.66}$$

Now, let us assume that a shear stress $T_{R\phi}$ can be associated with this rate of strain,

$$T_{R\phi} = \mu R\frac{d\Omega}{dR}, \tag{1.67}$$

where μ is the coefficient of viscosity. From this, we can notice that a uniformly rotating disk, with $d\Omega/dR = 0$, produces no viscous shear stress $T_{R\phi}$. For a differentially rotating disk on the other hand, with $\mu > 0$, the friction of the slowly moving material on the outside exerts a surface force in the $-\phi$ direction on the neighbouring material inside. This in turn produces a viscous torque which promotes an outward transport of angular momentum. If we denote the angular momentum per unit mass of the material as

$$j = R^2\Omega, \tag{1.68}$$

it is possible to show that the ϕ-component of the force equation can be written in the form

$$\rho\left(\frac{\partial j}{\partial t} + u_R\frac{\partial j}{\partial R} + u_z\frac{\partial j}{\partial z}\right) = \frac{1}{R}\frac{\partial}{\partial R}(R^2 T_{R\phi}). \tag{1.69}$$

We can see from equations 1.64 and 1.68 that j has negligible variations with t and z and hence we can integrate equation 1.69 over z to obtain the angular momentum transport equation,

$$-\dot{M}_d\frac{dj}{dR} = \frac{\partial\tau}{\partial R}, \tag{1.70}$$

where we have considered the mass accretion rate across a circle of circumference $2\pi R$ in the disk as

$$\dot{M}_d \equiv -2\pi R u_R \Sigma, \tag{1.71}$$

and τ as the viscous torque across the same circle,

$$\tau \equiv 2\pi R\int_{-H}^{+H} R T_{R\phi} dz. \tag{1.72}$$

Equation 1.70 states that the difference in viscous torque on the outer and inner edges of an annulus of area $2\pi R dR$ causes an inward flow of mass ($\dot{M}_d$) in the disk, when the specific angular momentum between the two edges is dj.

We now define the kinematic viscosity as

$$\nu_* \equiv \frac{\mu}{\rho}, \tag{1.73}$$

so that equation 1.67 becomes

$$T_{R\phi} = \rho\nu_* R\frac{d\Omega}{dR}. \tag{1.74}$$

Now with the assumption that ν_* varies slowly with z so that we can approximate it by its value at the midplane, let us perform the integration in z for equation 1.72 to obtain

$$\tau = 2\pi R\Sigma\nu_* R^2 \frac{d\Omega}{dR}. \tag{1.75}$$

The surface density Σ satisfies the axisymmetric equation of continuity integrated over z,

$$\frac{\partial\Sigma}{\partial t} + \frac{1}{R}\frac{\partial}{\partial R}(Ru_R\Sigma) = 0, \tag{1.76}$$

which, with the help of equation 1.71, can be rewritten as

$$\frac{\partial\Sigma}{\partial t} - \frac{1}{2\pi R}\frac{\partial\dot{M}_d}{\partial R} = 0. \tag{1.77}$$

If we can regard ν_* as a known, equations 1.70, 1.75 and 1.77 constitute a complete set to solve for the R and t dependences of the disk accretion rate $\dot{M}_d$, the viscous torque τ, and the disk surface density Σ.

Now, we can rewrite equation 1.77 using equations 1.70 and 1.75 to obtain

$$\frac{\partial\Sigma}{\partial t} + \frac{1}{R}\frac{\partial}{\partial R}\left[\left(\frac{dj}{dR}\right)^{-1}\frac{\partial}{\partial R}\left(R^3\frac{d\Omega}{dR}\nu_*\Sigma\right)\right] = 0. \tag{1.78}$$

Since $j = R^2\Omega$, equation 1.78 shows that the spreading of Σ represents a diffusion process (inwards in the inner disk part for mass accretion and outwards in the outer disk for the conservation of angular momentum). This means that Σ satisfies a real PDE which possesses two space and one time derivatives, with the diffusion coefficient given in the order of magnitude by the kinematic viscosity ν_*. Specific examples of using a transformation to j as the spatial variable in place of R can be found in e.g. Lynden-Bell and Pringle, 1974. The time scale for the viscous accretion to reach a quasi-steady state in the disk locally should therefore be in the order of magnitude form

$$t_{acc} = R^2/\nu_*. \tag{1.79}$$

If the molecular contribution was the only source of viscosity, then ν_* would be $\sim \ell v_T$, where ℓ is the particle mean free path and v_T is the thermal velocity. Here, the values appropriate for a nebular disk around a newly born star would be $R \sim 10^{14}$ cm, $\ell \sim 10$ cm, and $v_T \sim 10^5$ cm s^{-1}. Then the viscous accretion time scale would be $t_{acc} \sim 10^{22}$ s $\sim 3\times10^{14}$ yr, higher by 7 to 8 orders of magnitude than the age conventionally ascribed to such disks (Shu, 1992). In such cases, for the viscous accretion to explain such objects, there must be an anomalous source of viscosity. The same conclusion holds for all other astronomical objects where viscous accretion disks are considered to explain their operation.

Many processes have been proposed, and also tested in numerical simulations, over the last couple of decades as sources of this anomalous viscosity. Some of them are very specific and unavoidable in the relevant systems, like convective turbulence (e.g. in Lin and Papaloizou, 1980). The other processes are more generic, for instance, which depend on magnetic stresses, the self-gravity of the disk, and different other mechanisms. A more promising mechanism arises when the disk is threaded by weak poloidal magnetic fields. Velikhov, 1959 and Chandrasekhar, 1961 described this process in the 1960s, but its importance as a viscosity-driving mechanism in

astrophysical accretion disks was realized by Balbus and Hawley, 1991. More details about the operation of this mechanism are described in section 1.4.4. Prior to this, scientists considered an effective viscosity which drives the instabilities in the disk. This was done by writing an effective viscous shear stress in terms of a dimensionless "α-parameter", which is briefly described below. This prescription is still a useful one considering the simplicity of the arguments needed to describe realistic astrophysical scenarios.

The α-disk prescription

Shakura and Sunyaev, 1973 defined an effective viscosity (α) parameter which drives the angular momentum transport in an accretion disk. The argument was as follows.

If the source of viscosity in accretion disks is turbulence, then the coefficient of kinematic viscosity ν_* has the form

$$\nu_* \approx l_0 v_0, \tag{1.80}$$

where l_0 is the correlation length of the turbulence and v_0 is the mean turbulent speed. If we assume that the velocity of the turbulent elements cannot exceed the local sound speed ($v_0 < c_s$), and also that their typical size cannot be higher than the disk thickness ($l_0 < H$), then we can write

$$\nu_* = \alpha H c_s, \tag{1.81}$$

where $0 < \alpha < 1$ is a dimensionless coefficient, assumed by Shakura and Sunyaev to be a constant.

Now for thin disks, the hydrodynamical stress tensor can be written in terms of an internal torque with the approximate form

$$T_{r\phi} = \rho \nu_* \frac{\partial \Omega}{\partial r}. \tag{1.82}$$

For thin disks, $r(\partial\Omega/\partial r) \approx -\Omega$ and $c_s = (P/\rho)^{1/2} \approx \Omega H$. So the torque must have the form $T_{r\phi} = -\alpha P$. From numerical simulations, it is now apparent that the pressure P we consider should include the gas and radiation contributions (Hirose, Krolik, and Blaes, 2009). Typical values of α are ~ 0.1 (King, Pringle, and Livio, 2007).

Fluid description in black hole spacetime

To describe the behavior of matter in a black hole space time, we often solve the fundamental conservation laws, namely the conservation of rest mass and the conservation of energy-momentum, which can be expressed mathematically as

$$\nabla_\mu (\rho u^\mu) = 0, \ \nabla_\mu T^\mu_\nu = 0, \tag{1.83}$$

where ρ is the rest mass density, u^μ is the four velocity of matter, and T^μ_ν is the stress-energy tensor. These conservation laws are supplemented by other material equations like the equation of state, prescriptions of conductivity, viscosity, opacity, etc which are mostly approximations and will depend on the system under consideration. The stress-energy tensor is often described to be consisted of a fluid part and an electromagnetic part in the context of accretion disks (further description of this is in Chapter 2). The fluid part can be written as

$$(T^{\mu}_{\nu})_{\rm fluid} = (\rho u^{\mu})(W u_{\nu}) + \delta^{\mu}_{\nu} P, \tag{1.84}$$

where W is the enthalpy, δ^{μ}_{ν} is the Kronecker delta and P is the fluid pressure. The fluid density, enthalpy, pressure and other characteristics are linked by the first law of thermodynamics, $\mathrm{d}U = T\mathrm{d}S - P\mathrm{d}V$, which we can write also in the form

$$\mathrm{d}\epsilon = W\mathrm{d}\rho + nT\mathrm{d}S, \tag{1.85}$$

where U is the internal energy, T is the temperature, S is the entropy and $\epsilon = \rho c^2 + \Pi$ is the total energy density, with Π being the internal energy density and

$$V = \frac{1}{n},\ U = \frac{\Pi}{n},\ W = \frac{P+\epsilon}{\rho}. \tag{1.86}$$

In many situations, the equation of state is assumed to be that of an ideal gas,

$$P = \frac{\mathcal{R}}{\mu}\rho T, \tag{1.87}$$

where $\mathcal{R}$ is the universal gas constant and μ is the mean molecular weight.

Characteristic timescales

Now, let us consider briefly the generic types of physical processes that can occur in black hole accretion disks and the associated timescales. First are the dynamical processes with a characteristic timescale $t_{\rm dyn} \sim 1/\Omega$ where Ω is the orbital angular velocity. Thermal processes have a characteristic timescale $t_{\rm th} \sim c_s^2/\nu_*\Omega^2$, where c_s is the sound speed and ν_* is the kinematic viscosity. The next is the viscous processes with a characteristic timescale $t_{\rm vis} \sim r^2/\nu_*$ where r is the radial distance from the black hole. Typically we expect that

$$t_{\rm dyn} \ll t_{\rm th} \ll t_{\rm vis}. \tag{1.88}$$

Classification of disk solutions

It is difficult to obtain a general self-consistent solution to the whole set of hydrodynamic equations describing the accretion flows. So most of the research has been concentrated on obtaining different classes of restricted solutions to the complete set of equations (Frank, King, and Raine, 2002). As an initial approximation, it is appropriate to consider only the dynamical structure of the disk as the dynamical processes are much faster than viscous and thermal processes. The dynamical structure of the disk is driven mainly by the forces of gravity, pressure and rotation. The particular astrophysical situation dictates the relative relevance of these forces in a system. Based on the dynamical structure, the accretion flows can be divided into a few generic classes which are described below. We can characterize the flows in terms of their relative thickness $h = H/R$, dimensionless accretion rate $\dot{m} = 0.1\dot{M}c^2/L_{\rm Edd}$, optical depth τ, the ratio of advective energy flux to the radiative one (which gives the importance of advection) $q = Q_{\rm adv}/Q_{\rm rad}$, the importance of radiation pressure $\xi = P_{\rm gas}/(P_{\rm gas} + P_{\rm rad})$, location of the inner edge of the disk $r_{\rm in}$, and the accretion efficiency η (Abramowicz and Fragile, 2013).

- **The thin disk:** These are geometrically thin and optically thick disks that radiate efficiently and are in thermal equilibrium. They are expected to be found

around slowly rotating black holes with small accretion rates. We can describe their structure with the standard Shakura-Sunyaev prescription. The thin disk can be characterized by the following values of parameters described above: $h \ll 1$, $\dot{m} < 1$, $\tau \gg 1$, $q = 0$, $\xi \sim 1$, $r_{\rm in} = r_{\rm ms}$ and $\eta \sim 0.1$.

- **The thick disk:** These are geometrically thick and optically thin disks that radiate inefficiently and are not in thermal equilibrium. They are expected to be found along with rapidly rotating black holes and usually possess higher accretion rates. These solutions are found as steady-state solutions, but in realistic scenarios, the presence of magnetic fields drives the turbulence in them which results in higher accretion rates. The thick disks can be described by the following values of parameters: $h > 1$, $\dot{m} \gg 1$, $\tau \gg 1$, $q \sim 1$, $\xi \ll 1$, $r_{\rm in} \sim r_{\rm mb}$ and $\eta \ll 0.1$.

- **The slim disk:** The slim disk solutions have a geometrical thickness which falls between the thin disks and the thick disks and hence the name. This configuration is considered in cases where the thin disk approximation is not viable. The slim disks can be described by the following values of parameters: $h \sim 1$, $\dot{m} \gtrsim 1$, $\tau \gg 1$, $q \sim 1$, $\xi < 1$, $r_{\rm mb} < r_{\rm in} < r_{\rm ms}$ and $\eta < 0.1$.

- **The advection dominated accretion flows (ADAFs:)** A separate class of accretion flow solutions were discovered which can be different from the disk solutions described above. These flows develop when the accreting plasma possesses smaller angular momentum as compared to the standard disks. The ADAFs can be characterized by the following values of parameters: $h < 1$, $\dot{m} \ll 1$, $\tau \ll 1$, $q \sim 1$, $\xi = 1$, $r_{\rm mb} < r_{\rm in} < r_{\rm ms}$ and $\eta \ll 0.1$.

If we take a closer look, we can notice that the parameter space of these flows overlaps with one another in certain contexts. For example, there exist ADAF solutions with the same mass accretion rate as thin disk solutions (Chen et al., 1995). In such cases, it is not clear which solution prevails in realistic systems. Figure 1.3 shows a standard classification of disk solutions based on the mass accretion rate and the optical thickness. In this figure, the mass accretion rate is scaled to the Eddington rate, $\dot{m} = \dot{M}/\dot{M}_{\rm Edd}$.

Thick disks

The models we use in this thesis belong to the class of thick accretion disks and we now discuss here some more important details of this class of solutions. Researchers starting in the 1970s developed a general method of constructing perfect fluid equilibrium solutions of matter orbiting around a Kerr black hole (e.g. Fishbone and Moncrief, 1976; Abramowicz, Jaroszynski, and Sikora, 1978; Paczyński and Wiita, 1980; Paczynski and Abramowicz, 1982). A general description of these models can be obtained as follows. Let the matter is distributed uniformly and axisymmetrically and it orbits the black hole along circular trajectories with an angular momentum $\mathcal{L}(r, \theta)$. Since it is a fluid only description, the stress-energy tensor is given by equation 1.84,

$$T^{\mu}_{\nu} = (T^{\mu}_{\nu})_{\rm fluid} = \rho W u^{\mu} u_{\nu} + P \delta^{\mu}_{\nu}. \tag{1.89}$$

Also, the four-velocity of the matter has the following form,

$$u^{\mu} = A(\eta^{\mu} + \Omega \xi^{\mu}), \tag{1.90}$$

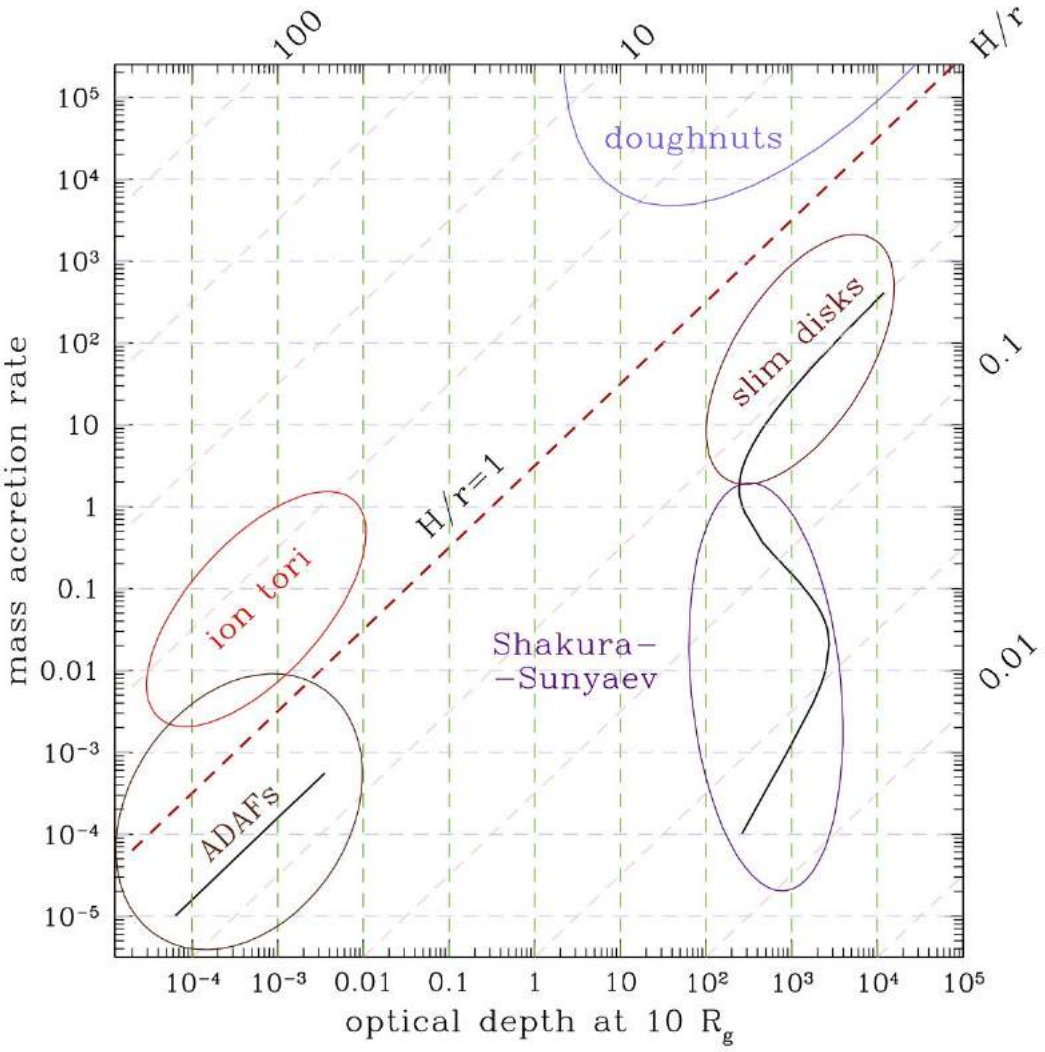

FIGURE 1.3: Plot depicting various types of analytic or semi-analytic accretion disk solutions based on the mass accretion rate ($\dot{m}$) and optical depth (Σ). The models we use in this thesis belong to the class of thick disk solutions (sometimes referred to as "doughnuts" because of their geometry) which is discussed in section 1.2.4 (Figure credit: Abramowicz and Fragile, 2013).

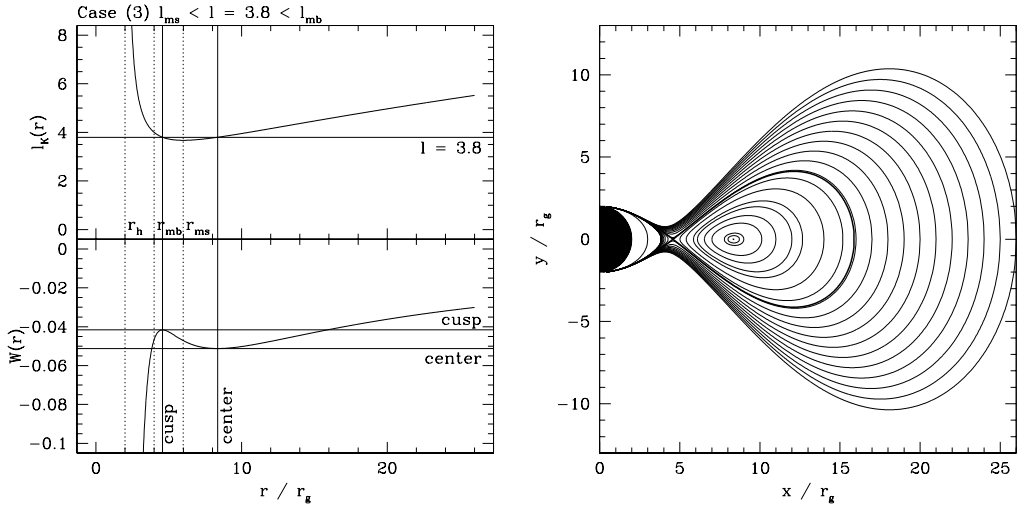

FIGURE 1.4: Representation of a constant angular momentum thick disk orbiting a Schwarzchild black hole. The right panel shows the equipressure surfaces for a constant specific angular momentum value of $\ell = 3.8$. W on the left panel of the figure refers to effective potential. The figure is adapted from Font and Daigne, 2002.

where η^μ and ξ^μ are the Killing vectors associated with the time and azimuthal symmetry, respectively and $\Omega = u^\phi/u^t$ is the angular velocity. The normalization constant (sometimes called the red-shift factor) A comes from the $u^\mu u^\nu g_{\mu\nu} = -1$ condition,

$$-A^{-2} = g_{tt} + 2\Omega g_{t\phi} + \Omega^2 g_{\phi\phi}. \tag{1.91}$$

Now, using the general equation $\nabla_\mu T^\mu_\nu = 0$, one can derive the expression,

$$\nabla_\mu \ln A - \frac{\ell \nabla_\nu \Omega}{1 - \ell\Omega} = \frac{1}{\rho}\nabla_\nu P. \tag{1.92}$$

In the case of a barytropic fluid ($P = P(\epsilon)$), the right-hand side of equation 1.92 is the gradient of a scalar function, and thus the left-hand side also should be the gradient of a scalar, which gives,

$$\ell = \ell(\Omega). \tag{1.93}$$

The equation for equipressure surfaces, $P = P(r,\theta) =$ constant, can be written in Boyer-Lindquist coordinates as $r_P = r_P(\theta)$, where $r_P(\theta)$ is given by

$$-\frac{dr_P}{d\theta} = \frac{\partial_\theta P}{\partial_r P} = \frac{(1-\ell\,\Omega)\partial_\theta \ln A + \ell\,\partial_\theta \Omega}{(1-\ell\,\Omega)\partial_r \ln A + \ell\,\partial_r \Omega}. \tag{1.94}$$

Knowing the values of angular velocity or specific angular momentum ($\ell = \ell(r,\theta) = -u_\phi/u_t$), equation 1.94 can be integrated to get the shapes of equipressure surfaces (Chakrabarti, 1985). Figure 1.4 shows the equipressure surfaces for one case of $\ell = \ell(\Omega) = \ell_0 =$ constant.

Having described the essential theoretical aspects of accretion flows, we will now focus on a more astrophysical aspects of accreting environments.

1.3 Radiation mechanisms

The mechanisms which generate electromagnetic radiation depend hugely on the thermodynamic state of matter (including electron density, ion density, and temperature), its state of motion and the strength of the magnetic field present. Also, the opacity of matter to radiation plays a major role in this. Thus optically thick accretion disks (with $\tau \gg 1$, where τ is the optical depth) can be quite luminous and efficiently cooled by radiation. On the other hand, optically thin accretion disks (with $\tau \ll 1$) are inefficiently cooled and are less luminous.

Electromagnetic theory dictates that any charged particle when accelerated emits energy in the form of electromagnetic waves or in other words radiation. We now briefly discuss the important radiative processes which produce the electromagnetic emission in the astrophysical contexts considered in this thesis. A more detailed description of these processes is found in standard textbooks (e.g. Rybicki and Lightman, 1986).

1.3.1 Black body radiation

All baryonic matter emits electromagnetic radiation when it is above absolute zero temperature. This radiation is often called thermal radiation because it represents a conversion of the internal energy of the matter into electromagnetic energy. On the other hand, all matter absorbs electromagnetic radiation to a certain extent. When an object absorbs all the radiation falling on it, at all wavelengths, it is called a black body. At the same time such a body, if it is at a uniform temperature, will have a characteristic emission frequency distribution at a given temperature. This emission is called black body radiation. The concept of a black body is an idealization as no perfect black bodies exist in nature. The intensity of the emitted radiation in such a system depends on the equilibrium temperature of the body. The intensity of the black body radiation at a given frequency ν is given by

$$I_\nu = \frac{2h\nu^3}{c^2(e^{h\nu/k_BT} - 1)}, \tag{1.95}$$

where h is the Planck's constant, c is the speed of light in vacuum, k_B is the Boltzmann's constant, and T is the temperature in the absolute scale.

1.3.2 Bremsstrahlung

Bremsstrahlung is the radiation produced by the deceleration of a charged particle when deflected by another charged particle, or in other words due to the acceleration caused by an electric field of another charged particle. Typically an electron produces such radiation when deflected by a proton or an atomic nucleus. The name comes from the German word "Bremsstrahlung" which can be translated as "braking radiation" due to the braking effect for electrons when they hit a metal target. The incident electrons are not bound to a system (e.g. an atom or ion) both before and after the incidence and hence the emitted spectrum is continuous. It is sometimes called the "free-free" emission owing to this fact. In astrophysical scenarios, the free-free emission is caused by the inelastic scattering of relativistic thermal electrons off (non-relativistic) ions and other electrons. Thus the emissivity (emission rate per unit volume) will be constituted by the electron-ion and electron-electron interaction contributions. Often, X-rays are emitted by the incident electrons through this

mechanism if they initially possess high enough energy. If quantum effects are negligible, the total power radiated by an accelerated charged particle is given by the relativistic generalization of the Larmor formula,

$$P = \frac{q^4\gamma^4}{6\pi\epsilon_0 c}\left[\dot{\beta}^2 + \frac{(\beta.\dot{\beta})^2}{1-\beta^2}\right], \tag{1.96}$$

where q is the charge of the particle, γ is the Lorentz factor, ϵ_0 is the permittivity of the free space, β $(= v/c)$ is the ratio of the particle velocity to the speed of light and $\dot{\beta}$ is its time derivative.

One of the astrophysical examples of bremsstrahlung radiation observed involves the hot intracluster gas of galaxy clusters. A recent study on the role of bremsstrahlung for the GRMHD models of accreting black holes was done by considering the spectral energy distributions of accretion disks around slowly accreting supermassive black holes (Yarza et al., 2020).

1.3.3 Synchrotron emission

Synchrotron radiation is the electromagnetic emission produced by a relativistic charged particle gyrating in a magnetic field. In such a case, the acceleration is perpendicular to the particle velocity. It was first noticed when a charged particle beam was accelerated in a circular accelerator called the General Electric 70 MeV Synchrotron and hence the name. The radiation produced this way is naturally polarized due to the mechanism and the frequencies generated can range over a large range of the electromagnetic spectrum. Synchrotron radiation is similar to the bremsstrahlung, which is emitted when a charged particle is accelerated in a direction parallel to its velocity, and hence it is sometimes called magneto-bremsstrahlung. Assuming the accretion environment is threaded by magnetic fields, the relativistic electrons can radiate via synchrotron emission. The power radiated in synchrotron radiation by an accelerated charged particle is given by the relativistic Larmor formula,

$$P = \frac{1}{6\pi\epsilon_0}\frac{q^2a^2\gamma^4}{c^3}, \tag{1.97}$$

where a is the magnitude of the acceleration. The synchrotron power emitted by an electron can also be written in terms of the magnetic field energy density $U_{\rm B}$ in the form, $P = (4/3)\sigma_{\rm T}c\gamma^2\beta^2U_{\rm B}$. This process is believed to be responsible for the radio emission from our own galactic nucleus, supernova remnants, and extragalactic radio sources. It is also believed to be responsible for the non-thermal optical and X-ray emission observed from the Crab Nebula.

1.3.4 Inverse Compton scattering

Inverse Compton scattering is the process in which a charged particle transfers part of its energy to a photon and thereby increasing its energy. It is the opposite of the usual Compton effect in which a high-frequency photon loses its energy on interaction with a charged particle. In astrophysical systems, it is a major mechanism in which the lower energy photons produced by the thermal emission in the accretion disks are up-scattered to higher energies by the relativistic electrons in the surrounding corona. The total energy loss rate of the electron, and thereby the net power converted into radiation is given by

$$P = \frac{4}{3}\sigma_{\rm T} c \gamma^2 \beta^2 U_{\rm rad} \tag{1.98}$$

where $U_{\rm rad}$ is the radiation energy density.

1.4 Plasma instabilities

Plasma is one of the four fundamental states of matter in which a significant portion of its particles are charged with any combination of ions and electrons. Our current understanding is that most of the baryonic matter in the universe, especially in astrophysical systems, exists in this state (Chiuderi and Velli, 2015). When matter in other states becomes sufficiently hot and energetic, it becomes ionized and forms a plasma. The distinction between plasma and other molecular states matter is that the ionized substance becomes highly electrically conductive to the point that the long-range electric and magnetic fields dominate its behaviour (Chen, 2016). The presence of charged particles makes plasma electrically conductive and susceptible to local electromagnetic fields, which include strong fields generated by stars and in turn fields around accreting compact systems. To have a complete description of the plasma state, all the particle equations need to be solved for their motion in an electromagnetic field, which is practically impossible. So we often resort to approximations which fall into the general classes of fluid models and kinetic models. Fluid models describe the plasma in terms of bulk quantities like density and averaged velocity. Magnetohydrodynamics (MHD) which falls under the fluid description treats plasma as a single fluid governed by a combination of Maxwell's equations and the Navier-Stokes equations. This thesis studies the astrophysical plasma in the context of MHD. This section describes very briefly the most important hydrodynamic and magnetohydrodynamic instabilities relevant in the context of accretion flows considered in this thesis.

1.4.1 Raleigh-Taylor instability

The Raleigh-Taylor instability is an instability of interface between two fluids of different densities when a heavy fluid rests on top of a lighter one in an effective gravitational potential. Energetically, the fluids will seek to reduce their combined potential energy and thus the system will tend to overturn its configuration. These overturns are often accomplished by "fingers" of fluid penetrating each other. In a configuration of two fluids as depicted in the cartoon in Figure 1.5, the Raleigh-Taylor instability will arise for $\rho_1 > \rho_0$ when the gravitational force is directed downwards. The resulting turbulence and mixing have considerable consequences in many natural flows including supernova explosions (Wang and Chevalier, 2001). Figure 1.6 shows the Raleigh-Taylor instability fingers visible in the Hubble image of the Crab Nebula. This instability is often accompanied by another type of fluid instability called the Kelvin-Helmholtz Instability.

1.4.2 Kelvin-Helmholtz instability

Kelvin-Helholtz instability occurs when there is a velocity difference between two fluids in contact or when there is a velocity shear in a single continuous fluid. This often happens when one fluid tries to slip past the other one via a tangential discontinuity. A jet of fluid plasma which tries to propagate through an ambient medium is a prevalent astrophysical example of such a scenario. In the simplistic example

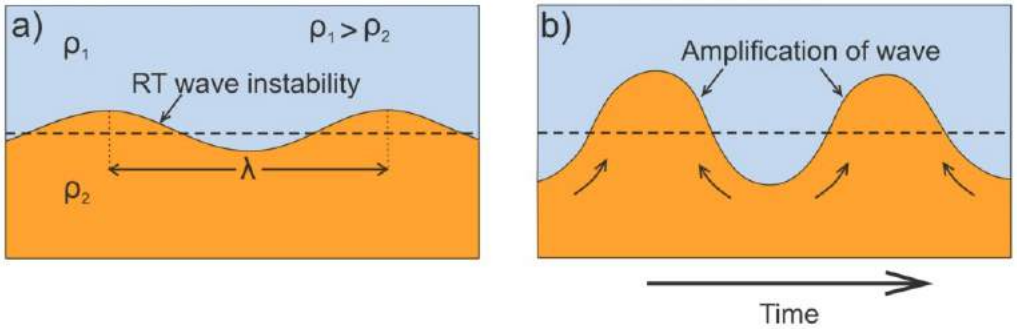

FIGURE 1.5: Schematic of two fluid layers of densities ρ_1 and ρ_2, with velocities u_1 and u_2 respectively, flowing adjacent to each other. When the gravitational force is directed downwards, the condition for Raleigh-Taylor instability is $\rho_1 > \rho_2$ (Figure credits: Ghosh, 2021)

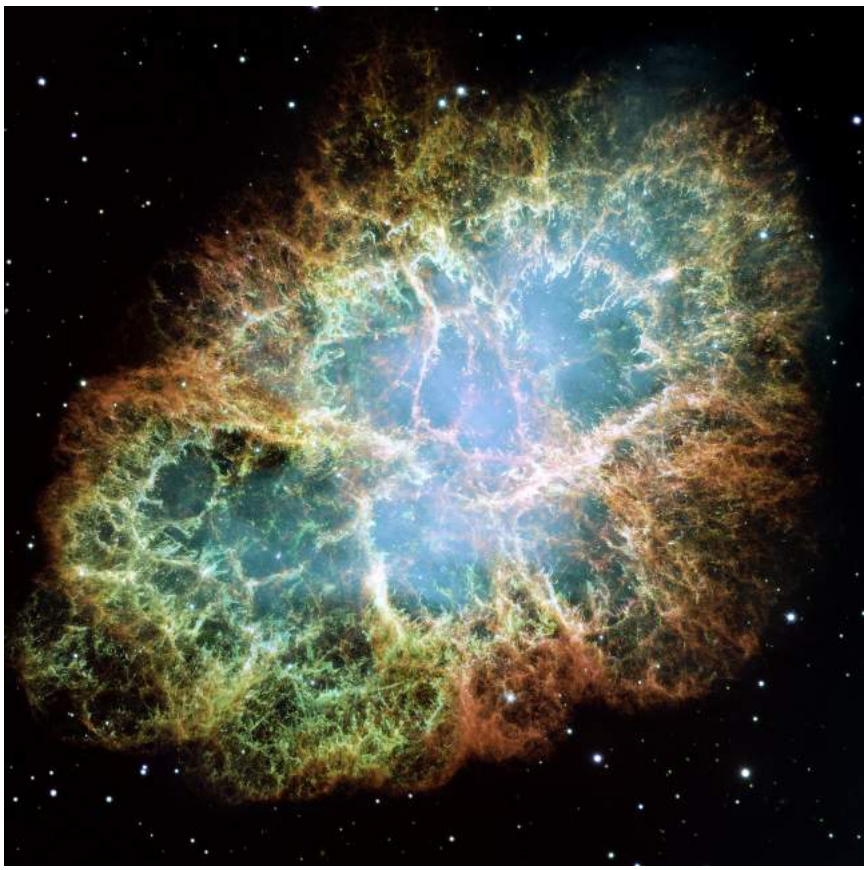

FIGURE 1.6: Raleigh-Taylor instability fingers visible in the Hubble Space Telescope image of the Crab Nebula. Image credits: NASA, ESA, J. Hester and A. Loll (Arizona State University).

presented in Figure 1.5, the Kelvin-Helmholtz instability will arise when the square of the slip speed satisfies the condition

$$(u_1 - u_2)^2 \geq \frac{2(\rho_1 + \rho_2)}{\rho_1 \rho_2}[Tg(\rho_2 - \rho_1)^{1/2}] \tag{1.99}$$

when the system lies in a vertical gravitational field with downward directed acceleration g and the interface between the fluids has an associated surface tension T. The Raleigh-Taylor and Kelvin-Helmholtz instabilities often appear together in the same system. For example, the Kelvin-Helmholtz instability can distort the opposed fingers of heavy and light fluid that try to slip through one another during the development of the Raleigh-Taylor instability (Shu, 1992).

1.4.3 Rotational instability (Rayleigh criterion)

Here we describe Rayleigh's criterion for the instability of a rotating fluid. For this, let us consider an axisymmetric fluid distribution (e.g. a flattened disk or a cylinder) which rotates about its axis under the combination of gravitational attraction and pressure gradient. Then the equilibrium condition is

$$-R\Omega^2(R) = g - \frac{1}{\rho}\frac{dP}{dR} \tag{1.100}$$

where R is the cylindrical radius, and P is the fluid pressure. Let us consider now whether the equilibrium presented here is stable. For this, let us assume a specific ring in the disk, whose specific angular momentum given by $j = R^2\Omega(R)$ is conserved due to the axial symmetry of the system. This system can be considered stable if the displaced fluid rings tend to return to their original positions. Now let us assume we displace a ring of fluid from R_0 to R_1, and then the condition for stability is given by

$$(R_0^2\Omega_0)^2 < (R_1^2\Omega_1)^2. \tag{1.101}$$

So the Raleigh criterion for rotational instability is

$$\frac{d}{dR}\left[(R^2\Omega)^2\right] < 0. \tag{1.102}$$

If the specific angular momentum of the disk decreases with increasing radius, then the disk will violate this criterion and will be unstable to hydrodynamical perturbations. In most cases, astrophysical accretion disks are stable to this instability, as shown by many authors (e.g. Hawley, Balbus, and Winters, 1999).

1.4.4 Magnetorotational instability (MRI)

Having described the basic hydrodynamic instabilities relevant to us, let us now consider magnetized flows. We have already discussed the origin and prevalence of magnetic fields in the astrophysical plasma and in turn in the accretion disks. In reality, the presence of magnetic fields plays a crucial role in the development and sustenance of accretion flows onto compact objects. We now discuss one of the most relevant plasma instability, termed as magnetorotational instability (MRI), and its importance in the context of astrophysical accretion disks.

The MRI is believed to be one of the most important mechanisms which generate turbulence and drives angular momentum transport in astrophysical accretion disks. It is an instability that arises due to the action of a weak magnetic field in a

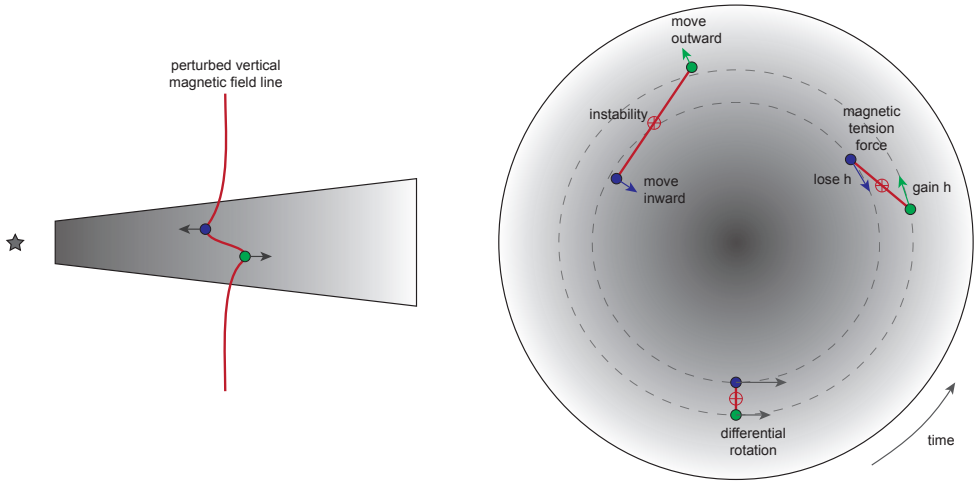

FIGURE 1.7: A schematic showing the action of MRI in a magnetized accretion disk. The figure shows two fluid elements in a disk in nearby orbits in blue and green colors, the magnetic tension force which connects them and the action of MRI due to this. The left part shows the poloidal view and the right part shows the top view of the configuration (Figure credit: Armitage, 2022).

differentially rotating disk. It grows very fast, on orbital timescales, and can drive turbulence in the disk once it becomes non-linear. The mechanism was initially described by Velikhov, 1959 and Chandrasekhar, 1961, but its importance to the accretion disks was realized by Balbus and Hawley, 1991 (see Balbus and Hawley, 1998 for a review). Balbus and Hawley's paper describes the instability by starting with fluid equations for a magnetized differentially rotating disk and applying the tools of first-order perturbation theory. We here stick to a simpler but more physically intuitive description. The basic mechanism of the MRI action is depicted in Figure 1.7, for the conceptually simplest case of a disk threaded by a weak initially vertical magnetic field. In the figure, the blue (inner) and green (outer) circles represent two fluid elements in nearby Keplerian orbits connected by the magnetic tension force. Due to differential rotation of the disk, the inner fluid element moves faster than the outer one and this way the inner element gets pulled back while the outer element gets pulled forward. This way the outer fluid element gains more angular momentum while the inner one loses it and moves inwards. Thus angular momentum of the material in the disk is transported outwards.

A more detailed look at the problem will show that the disk will be susceptible to the MRI only if the magnetic field is weak, satisfying the condition,

$$\frac{B_z^2}{8\pi} < \frac{3}{\pi^2}\rho c_s^2, \tag{1.103}$$

where B_z is the vertical component of the magnetic field, and only if the rotational velocity of the disk satisfies

$$\frac{d}{dr}(\Omega^2) < 0. \tag{1.104}$$

Keplerian accretion disks always satisfy the criterion in equation 1.104, and thus are unstable to MRI whenever the vertical magnetic field threading them is sufficiently weak. The MRI is thus an effective mechanism which can drive turbulence in

a magnetized accretion disk. The random turbulent motions can lead to the outward transport of angular momentum through turbulent viscosity.

1.4.5 Interchange instability

Interchange instability is a hydromagnetic instability which occurs when a plasma comes in contact with a magnetic field in free space. When the strength of the magnetic field decreases with distance from the boundary of the plasma, so that the field lines are curved outwards, then it is energetically favourable for the plasma to change places with the magnetic field. This phenomenon is known as interchange instability owing to the fact that the motion can be described as an interchange of lines of force in space (Frank-Kamenetskii, 1972). In other words, this instability is driven by gradients of magnetic pressure in areas where the confining magnetic field is curved. During the action of this instability, the field lines move as a whole, conserving their direction and geometry. The perturbation on the plasma surface then takes the shape of flutes along the magnetic field lines and hence this instability is also called flute instability. The concept of this instability was first noted by Kruskal and Schwarzschild, 1954, who demonstrated that a situation similar to Raleigh-Taylor instability in classical fluids exists in magnetically confined plasma. This instability is studied more in detail in the context of fusion reactors as the development of this instability adversely affects the plasma confinement in magnetically confined fusion.

On the other hand, the presence and action of interchange instability are important, along with the magnetic reconnection, in driving the accretion in magnetically arrested disks (MADs) which is discussed in the following section.

1.5 Magnetically arrested disks

Magnetically arrested accretion flows are formed in black hole systems when a significant amount of poloidal magnetic flux is accumulated in the vicinity of a black hole due to a cumulative action of the accretion flow. The accumulated field will be prevented from escaping outwards by the continued inward pressure of accretion while the field lines also cannot fall into the black hole which results in the accumulation of flux on the horizon (Punsly, 2001). Now the accumulated poloidal magnetic flux disrupts the accretion flow at a certain (magnetospheric) radius which lies outside the event horizon of the black hole. The flow then breaks up into blobs or streams, and the gas has to fight its way towards the black hole through a process of magnetic interchanges and reconnection. The velocity of the gas in this disrupted region is much less than the free-fall velocity. This type of disrupted accretion flow is known as a "magnetically arrested disk" (or MAD) (Narayan, Igumenshchev, and Abramowicz, 2003). Bisnovatyi-Kogan and Ruzmaikin, 1974 discussed a similar concept, emphasizing the significance of a large-scale dipole magnetic field in a non-rotating accretion flow. They employed a method for the resistivity of turbulent plasma, similar to the α-viscosity of turbulent hydrodynamics. These old ideas were then later recognized and confirmed in 3D MHD simulations of radiatively inefficient accretion flows around black holes. When disks are radiatively efficient, they can be sometimes cool enough to be neutral and the magnetic field can pass through the gas via ambipolar diffusion. However, if magnetic winds are involved in angular momentum loss, there is a possibility that a substantial field may be pulled towards

the center and the MAD state is achievable (Narayan, Igumenshchev, and Abramowicz, 2003). MAD models have been also shown to result in Poynting-dominated jets from accreting black holes (Igumenshchev, 2008). MAD models have been studied later on in much detail in many GRMHD simulations and it has been shown that in conjunction with the Blandford-Znajek mechanism (Blandford and Znajek, 1977), it can act as a very good environment for the extraction of energy from the rotation of the black hole and the rest mass energy of the accreting gas (Tchekhovskoy, Narayan, and McKinney, 2011). A lot of interest in this model has arisen recently when it was suggested from the EHT observations and the associated numerical simulations that M87* exists very likely in a MAD state (Event Horizon Telescope Collaboration et al., 2021). From the recent observations, it is apparent that Sgr A* may also be existing in a MAD state (Event Horizon Telescope Collaboration et al., 2022b), even though this fact is disputable because of the severe constraints set by the light curve variability of the source (Event Horizon Telescope Collaboration et al., 2022a). So the characteristic of magnetic field configuration around Sgr A* is still an active research topic.

In contrast to the magnetically arrested state, another type of flow is often defined which is weakly magnetized and without huge hindrance from the magnetic field. It is termed as "standard and normal evolution" (or SANE).

1.6 Relativistic jets

Relativistic jets are extended beams of ionized particles and radiation that are accelerated close to the speed of light launched along the rotation axis of magnetized accreting objects. They are highly complex phenomena with their origins often associated with the dynamic interactions within the accretion disk and with the central compact object. Most of the brightest sources we observe in the universe constitute relativistic jets. The ultra-relativistic jets in gamma-ray bursts and parsec scale jets in AGNs are great examples of this phenomenon. Over the years, various models have been proposed to explain the formation and properties of jets. But, the current consensus is that magnetic fields and rotation are the main factors responsible for their emergence. Two influential models in this field are the Blandford-Znajek (BZ) mechanism (Blandford and Znajek, 1977) and the Blandford-Payne (BP) mechanism (Blandford and Payne, 1982). The main difference between the two is the source of energy for the jet. The BZ mechanism relies on the rotational energy of the black hole, while the BP model uses the rotational energy of the accretion flow. Numerical simulations indicate that truly relativistic jets are primarily produced by the BZ mechanism, while quasi-relativistic jets and non-relativistic winds may be driven by a combination of the BP and other mechanisms (Yuan and Narayan, 2014).

In the BZ mechanism, a large-scale poloidal magnetic field penetrates the ergosphere of a rotating black hole and threads the horizon. This creates a toroidal field due to the frame-dragging effect by the rotation of the black hole and hence a Poynting flux. The BZ mechanism relies on the Penrose mechanism (Penrose and Floyd, 1971) which shows that negative electromagnetic energy can flow inward within the ergosphere (as measured at infinity) and reduce the mass-energy and angular momentum of the black hole. At the same time, an outward Poynting-dominated jet carries positive energy and angular momentum. The power liberated by the BZ mechanism is given by

$$P_{BZ} = \frac{\kappa}{4\pi c}\Phi^2\Omega_H^2 \tag{1.105}$$

where Φ is the magnetic flux on the black hole horizon, $\Omega_H = ac/2r_H$ is the angular velocity of the black hole horizon, with a being the dimensionless spin parameter of the black hole, and r_H is the radius of the horizon.

The BZ mechanism is believed to power the relativistic jets observed in nature including the ultra-relativistic jets in GRBs and relativistic jets in AGNs. Many numerical simulations, including the ones presented in this thesis, also support the idea that the BZ mechanism is an ideal candidate for powering relativistic jets.

It is also worth noting that the efficiency of both BZ and BP processes depends on field geometry and strength. Black hole spin plays a key role in the BZ process, but may also affect the BP process due to the inertial frame dragging. Most importantly, the two mechanisms lead to different compositions of the jet: the BP process loads the mass of the accretion disk itself and hence the jet is baryon rich while in the BZ process, the electron-positron pairs created in the black hole magnetosphere are the main jet composition.

1.7 Gamma-ray bursts

Gamma-ray bursts (GRBs) are interesting astrophysical events that occur during the end phases of the life cycles of certain stars. They are intense, short and non-repeating flashes of MeV γ-rays with various temporal, spectral and structural properties (Piran, 2004). They were discovered by the Vela satellites in the 1960s (Klebesadel, Strong, and Olson, 1973) and opened up an interesting field of further investigations about their occurrence, origin, progenitor systems and properties, which remain highly active until today. Their nature and origin remained a mystery for more than two decades after their discovery, owing to the fact that they could only be detected for tens of seconds mostly at gamma-ray energies. Also, the GRBs could only be detected by space-borne instruments because the high-energy light they emit cannot easily penetrate the Earth's atmosphere.

When a GRB happens, there is a sudden increase in the number of detected photons, which can be detected by the electronics on an observing satellite. This is known as the trigger. The photons collected can then be used to create light curves and spectra of the GRBs. High-energy astronomical instruments have different designs depending on their energy range and localizing requirements. A gamma-ray detection module is made up of a scintillator crystal containing heavy elements. When photons with energies ranging from a few keV to tens of MeV interact with the scintillator, they produce lower-energy photons that are detected by photomultipliers. The energy of the incoming gamma ray can then be measured. While the response of these modules is not uniform, comparing the photon counts in different modules on the same platform can provide a rough estimate of the location of the source (Duque, 2021). These GRB detection modules are used in most GRB missions. By timing the GRB photons across different satellites equipped with such modules, the source can be localized more accurately. There are more different types of detection instruments aboard GRB observatories, like Compton scattering instruments for detecting gamma-rays with energies up to a few MeV and pair-production instruments for gamma-rays with energies up to hundreds of GeV. The capability to localize GRBs in the sky played a major role in the further development of this field. This in turn resulted in the discovery of the afterglow phase of GRBs as well. Before this, we were relying only on gamma-ray data. This phase which consists of only gamma-ray photons from a burst is referred to as the prompt phase.

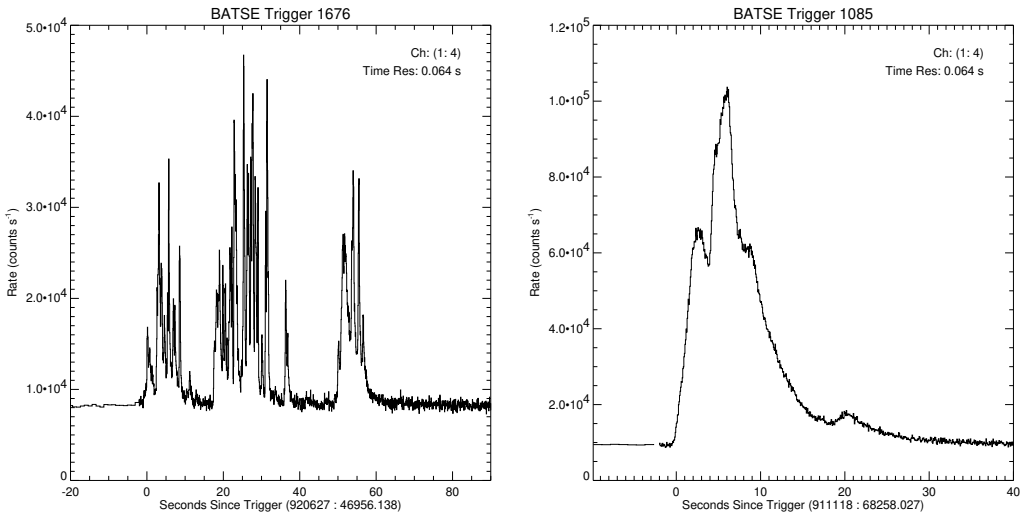

FIGURE 1.8: Two example light curves of gamma-ray bursts detected by BATSE on NASA's Compton Gamma Ray Observatory. The graphs show the number of photons with energies of over 20 keV counted per second over time in seconds. Both the light curves belong to the class of long gamma-ray bursts. The plots also show the varied morphology of the GRB light curves. (Figure credits: Mallozzi, 2018.)

A typical light curve of a GRB consists of a time sequence of the detected photon count in a given energy band. The gamma-ray light curve provides information about the duration of GRBs, often estimated with the T_{90} statistic. To determine the T_{90}, the photons are arranged in time order based on their measured energies. This helps to identify the time interval between when 5% and 95% of the cumulative detected energy were achieved. This is done after the instrumental and environmental background has been subtracted from the signal. GRBs show a wide range of durations, ranging from a few milliseconds to hundreds of seconds, as measured by their T_{90} values.

Figure 1.8 shows example GRB light curves from the BATSE equipment on the NASA's Compton Gamma-Ray Observatory.

Short and long GRBs

With time, astronomers started to recognize a bimodal distribution for the duration of GRB light curves. This was recognized more clearly based on BATSE data from Compton Gamma-Ray Observatory in the 1990s. The two classes are identified as the short and long GRBs, with their conventional division at $T_{90} \sim 2$ seconds (Norris et al., 1984; Kouveliotou et al., 1993). The short GRBs have a duration as small as a few milliseconds while the long events extend to hundreds of seconds. Also typically, the short GRBs tend to exhibit harder (higher in energy) γ-ray spectra while the long ones tend to exhibit generally softer spectra (von Kienlin et al., 2020).

During the afterglow era, we were able to identify the host galaxies of GRBs and make comparisons between the two classes of GRBs. Long GRBs are usually found in faint, blue, and highly star-forming galaxies located near the center of the galaxy and associated with massive stars (Le Floc'h et al., 2003; Savaglio, Glazebrook, and Le Borgne, 2009). However, short GRBs are not specific to any particular galaxy type

or star formation activity and can occur at a larger offset from their host galaxies (Fong and Berger, 2013).

The cosmological origin, the observed variability and energies suggested cataclysmic formation or interaction of compact objects as the source of both classes of GRBs. The general picture of the GRB phenomenology as we understand it now, is as follows. The transient activity in the vicinity of a compact object results in the launching of an ultra-relativistic jetted outflow which is Poynting dominated and that reaches Lorentz factors $\Gamma \gtrsim 100$ and isotropic equivalent energies of 10^{52}erg.

The differences in the observed properties for both classes of GRBs helped us in finding appropriate models to explain their origin. The origin of long GRBs was proposed in the 1990s to be the collapse of massive stars. This is known as the collapsar model (Woosley, 1993; Paczyński, 1998). In this model, a massive star collapses into a black hole and the surrounding material forms an accretion disk around it. This model was confirmed by various observations, together with the afterglow spectra of associated supernovae (e.g. Galama et al., 1998; Hjorth et al., 2003). The origin of short GRBs remained unclear for a longer time, even though the first sensible suggestions came in the 1980s (Paczynski, 1986; Eichler et al., 1989). The scenario for short GRBs which is widely accepted nowadays is the merger of two compact objects. It can be either two neutron stars or a neutron star and a black hole. The matter ejected from such a merger (e.g. by the tidal forces) will result in an accretion disk around the merger product, a black hole. This progenitor scenario was confirmed by the famous multi-messenger (i.e. in electromagnetic and gravitational wave spectra) observations of the GRB170817A, which was a short GRB with an associated gravitational wave event (Abbott et al., 2017). Despite having a general picture, there are many open questions in GRB physics including the central engine composition, the origin of high-energy emission, the jet structure, and very fast variability in time (see e.g. Zhang, 2011 for a review). Also, GRBs are excellent probes of the universe at high redshifts. A handful of GRBs have been detected at redshift $z > 6$ (even up to $z \sim 9$), and the distances to some of them were confirmed through spectroscopic as well photometric analysis (Salvaterra, 2015). So they also help to pinpoint the locations of the earliest star-forming galaxies.

1.8 Active galactic nuclei

AGNs are highly energetic astrophysical sources that are powered by accretion of matter onto supermassive black holes in the center of galaxies. These sources show unique observational signatures that span the entire electromagnetic spectrum and cover more than twenty orders of magnitude in frequency (Padovani et al., 2017). They are also known to be the most luminous persistent electromagnetic sources across the universe. A galaxy that hosts an AGN is often called an active galaxy. In 1909, Fath observed the strong emission lines in the nuclear spectrum of NGC1068, which marked the first recorded description of the optical spectrum of an AGN (Fath, 1909). Later on, Seyfert conducted a systematic study of a class of AGNs by examining the nuclear regions of six unusual spiral galaxies (Seyfert, 1943). The rich optical spectra of AGNs generated significant interest, leading to the eventual classification of Seyfert galaxies based on the presence (Seyfert 1 galaxies) or absence (Seyfert 2 galaxies) of broad permitted lines. The discovery of quasars in the early 1960s, with their high luminosities, quasi-stellar appearance, and optical spectra similar to those of Seyfert 1 galaxies, further propelled the study of AGNs (e.g. Schmidt, 1963). With the development of radio astronomy, radio-loud AGNs were

detected parallely along with such optical observations. We in turn were able to optically identify these extra-galactic radio sources which showed a rich emission line spectra similar to those of Seyfert galaxies. Also, some radio-loud AGNs were identified to have rapid variability in optically wavelengths, which were then collectively called blazars. These were later identified as AGNs with relativistic jets pointing towards our line of sight.

Various subclasses of AGNs have been defined based on their observed characteristics. They are traditionally classified based on the amount of radio emission from them as "radio-loud" and "radio-quiet", whereas the radio-loud sources are known to have relativistic jets which produce non-thermal radiation and the radio-quiet sources often do not possess them (Padovani, 2017). This is one of the presently relevant classifications. The study of AGNs is a very broad field and we skip here the elaborate details on their classification and observed properties (Detailed reviews on this topic can be found. e.g. Krolik, 1999; Tadhunter, 2008; Padovani et al., 2017). We will very briefly describe here the known physical characteristics of our two nearest known sources, Sgr A* and M87*.

The center of our own galaxy contains a compact radio source called Sgr A*, which provides as an excellent opportunity to study black hole accretion. The presence of a dark, compact object with a mass of $\sim 4.14 \times 10^6 M_\odot$, has been confirmed by the observing the orbits of O and B stars around the galactic center. Also, the measurements of the spatial size of Sgr A* indicates that it must be a supermassive black hole. Due to its relative proximity, there is abundant data available to study the nature of accretion flow in this source. Sgr A* typically remains in a steady, low luminosity state known as the "quiescent state". However, there are occasionally strong variations seen in the infrared and X-ray bands, referred to as "flares". The ADAF model and its variations describe the main features of the quiescent phase (Yuan and Narayan, 2014), but cause of flares remain unclear, despite significant advancements in recent research. The outer boundary of accretion around Sgr A* is typically assumed to be around the Bondi radius, $R_B \sim 10^5 R_{Schw.} \approx 0.04pc$. This is where the thermal energy of the external ambient gas equals its potential energy in the gravitational field of the black hole. *Chandra* X-ray observations helped in estimating the density and temperature of gas near R_B givin an estimate of the Bondi mass accretion rate.3D numerical simulations of accreting stellar winds also provided a consistent estimate of $\sim 10^{-6} M_\odot \mathrm{yr}^{-1}$. The simulations also suggests the gas to possess a considerable amount of angular momentum near the Bondi radius. Flares in Sgr A* have been detected in multiple wavebands, with the strongest being in X-rays and infrared. These flares occur within a range of a few minutes to three hours, suggesting that they are produced near the black hole. So far most models for explaining the observations have been phenomenological, and further investigations are essential in this regard.

M87* is a low-luminosity AGN at a distance of 16.9 Mpc from us with a measured central supermassive black hole mass of $M_{BH} = 6.2 \times 10^9 M_\odot$ (Event Horizon Telescope Collaboration et al., 2019). By the comparison of observed data, theoretical predictions and simulations, it is concluded that M87* is very likely in a MAD state (Event Horizon Telescope Collaboration et al., 2021). The spin of the black hole in M87* is not easy to determine (Event Horizon Telescope Collaboration et al., 2021), but some recent works started to put constraints on its value based on theoretical predictions (e.g. Cruz-Osorio et al., 2022). The mass accretion rate at the black hole horizon of M87* estimated from the EHT observations is in the range $\dot{M}_{BH} \approx (3 - 20) \times 10^{-4} M_\odot \mathrm{yr}^{-1}$. This combined with the bolometric luminosity estimate (considering only the nuclear emission) of $L_{bol} \approx 8.5 \times 10^{41} \mathrm{erg\,s}^{-1}$ can be

used to have an approximate estimate on the radiative efficiency of the source (Xie, Narayan, and Yuan, 2023). In reality, the theory of hot accretion flows around supermassive black holes, and how much energy is dissipated by viscous heating, is still a not clearly understood problem even though some rough constraints are available. More accurate calculations of accretion rate at the black hole horizon, the nature of magnetic fields (i.e. whether it is MAD or SANE), and developing appropriate models of accretion will help us to constrain and understand these phenomena with further clarity.

1.9 Chapters overview

In this thesis, we present different sets of numerical simulations of magnetized accretion onto Kerr black holes to explain some of the observed properties of GRBs and AGNs. We modeled the accretion of magnetized plasma in Kerr geometry by assuming ideal magnetohydrodynamics with the openly available HARM code (Gammie, McKinney, and Tóth, 2003; Noble et al., 2006). In Chapter 2, we present the basic numerical setup used in the simulations and describe our implementation of the HARM code.

In Chapter 3 (article 1), we present the time variability studies of magnetically dominated jets from black hole sources at different mass scales, from GRBs to AGNs. We investigate whether our models can qualitatively reproduce the anti-correlation found between the minimum variability time scale and the jet Lorentz factor as seen from observations in the case of GRBs and AGNs (Wu et al., 2016). In this part of the work, my contribution was in running all the simulations and the analysis of all the data from it, except for the power-density spectral analysis which was done by my colleague. My supervisor helped in interpreting the results and presenting the work in the proper context.

In Chapter 4 (article 2), we further focus our studies on the structural and temporal properties of GRB jets and investigate their dependence on the inflow properties. In this part of the thesis, I lead the investigation by running all the simulations, analysing the data, and interpreting of results. My supervisor helped me by providing guidance at different stages and also in the interpretation of results, along with another colleague from my group providing additional insights.

In chapter 5, we focus on the outflows developed in accreting black hole sources due to the presence of large-scale magnetic fields. In this work, I computed all the models and interpreted the resulting data in consultation with Prof. Vladimír Karas from the Czech Academy of Sciences and my supervisor.

Finally, Chapter 6 presents a brief summary of the thesis and its prospects.

Chapter 2

Numerical methods

Modeling the central engines of gamma-ray bursts, active galactic nuclei and the associated phenomena involve the modeling of plasma in extreme environments. Such scenarios are subject to strong gravity, extreme electromagnetic fields and rotation and thus demands relativistic considerations. In this chapter we discuss the basics of general relativistic magnetohydrodynamics (GRMHD), including the code we use and its scheme, the basic equations of GRMHD, the grid and coordinate setup we use in the code, and some code performance tests.

2.1 The HARM code

The HARM (High Accuracy Relativistic Magnetohydrodynamic) code originally developed by Gammie, McKinney, and Tóth, 2003 follows the time evolution of plasma in general relativity in a conservative and shock-capturing scheme by solving the equations of GRMHD. The code has been adapted and further developed in our group adding various capabilities including parellelization for 3D runs. The code uses a $3+1$ decomposition (e.g. Gourgoulhon, 2007) of the 4-dimensional spacetime metric by resolving it into three spatial and one temporal slice.

2.1.1 Basic GRMHD equations

Some of the basic equations for describing accretion flows around a black hole are discussed in the first chapter. Here we briefly describe them all in one place the way it is used in the HARM code and the assumptions made in the code. This section follows the original papers describing the code (Gammie, McKinney, and Tóth, 2003; Noble et al., 2006; Janiuk et al., 2018).

We follow the dynamical evolution of magnetized plasma by solving a set of partial differential equations. The first equation necessary to describe the fluid flow in GRMHD is for the conservation of particle number

$$(nu^{\mu})_{;\mu} = 0, \tag{2.1}$$

where n is the particle number density and u^{μ} is the four-velocity. When rewritten in the coordinate basis, replacing n with $\rho = mn$ where m is the mean rest mass per particle, this becomes

$$\frac{1}{\sqrt{-g}}\partial_{\mu}(\sqrt{-g}\rho u^{\mu}) = 0 \tag{2.2}$$

where $g = \det(g_{\mu\nu})$. This is called the continuity equation.

The next equations represent the conservation of energy-momentum

$$T^{\mu}_{\nu\ ;\mu} = 0 \tag{2.3}$$

where T^{μ}_{ν} is the stress-energy tensor.

For a system containing a only perfect fluid and an electromagnetic field, the stress-energy tensor can be written as the sum of a fluid part and an electromagnetic part:

$$T^{\mu\nu} = T^{\mu\nu}_{\text{fluid}} + T^{\mu\nu}_{\text{EM}} \tag{2.4}$$

where

$$T^{\mu\nu}_{\text{fluid}} = (\rho + u + p)u^{\mu}u^{\nu} + pg^{\mu\nu} \tag{2.5}$$

(here u is the internal energy and p the pressure of the gas) and

$$T^{\mu\nu}_{\text{EM}} = F^{\mu\alpha}F^{\nu}_{\alpha} - \frac{1}{4}g^{\mu\nu}F_{\alpha\beta}F^{\alpha\beta}. \tag{2.6}$$

Here $F^{\mu\nu}$ is the Faraday tensor and a factor of $\sqrt{4\pi}$ is absorbed into the definition of F for convenience. For convenience, we can define the magnetic field 4-vector in the fluid frame as $b^{\mu} \equiv \frac{1}{2}\epsilon^{\mu\nu\kappa\lambda}u_{\nu}F_{\lambda\kappa}$ where ϵ is the Levi-Civita tensor. Considering the ideal MHD approximation and after some rearrangements, we can write electromagnetic part of the stress tensor also in the form

$$T^{\mu\nu}_{\text{EM}} = b^2u^{\mu}u^{\nu} + \frac{1}{2}b^2g^{\mu\nu} - b^{\mu}b^{\nu}. \tag{2.7}$$

The next equation we solve is the (space components of the) induction equation

$$\partial_t(\sqrt{-g}B^i) = -\partial_j(\sqrt{-g}(b^ju^i - b^iu^j)), \tag{2.8}$$

subject to the constraint given by the time component of the equation,

$$\frac{1}{\sqrt{-g}}\partial_i(\sqrt{-g}B^i) = 0, \tag{2.9}$$

where B is the magnetic field and $b^i \equiv (B^i + B^iu^{\mu}g_{i\mu}u^i)/u^t$.

The strength of the magnetic field in the fluid frame can be obtained by $B^2 = b^{\alpha}b_{\alpha}$. It is also worth defining a magnetization parameter $\sigma = B^2/\rho$ and the plasma-β parameter $\beta = 2p/B^2$.

The equation of state (EOS), for the models studied in this thesis, is assumed to be that of an ideal gas $p = (\gamma - 1)u$, where γ is the adiabatic index (Gammie, McKinney, and Tóth, 2003). Other more realistic equations of state, taking into account the microphysics of the accreting matter, are also possible (e.g. Janiuk, 2017; Nouri, Janiuk, and Przerwa, 2023).

In summary, the set of fundamental equations solved by the HARM code are the particle number conservation equation (2.1), the four equations of energy-momentum conservation (2.3), and the induction equation (2.8).

It is also worth noting here the relativistic formulation of Maxwell's equations in curved spacetime

$$\partial_{\alpha}F_{\mu\nu} + \partial_{\nu}F_{\alpha\nu} + \partial_{\mu}F_{\nu\alpha} = 0, \quad \partial_{\alpha}F^{\alpha\beta} = \mu_0J^{\beta}, \tag{2.10}$$

where J^{β} is the electric current four-vector. The Faraday tensor $F_{\mu\nu}$ is given by

$$F_{\mu\nu} = \partial_\mu A_\nu - \partial_\nu A_\mu, \tag{2.11}$$

where A^μ is the electromagnetic four-vector.

2.1.2 Numerical scheme

There are different possible ways to integrate the GRMHD equations. The first choice is between the conservative and non-conservative schemes. Non-conservative schemes integrate the internal energy equation rather than the total energy one. Such schemes are useful when the internal energy is small compared to the total energy (e.g. Stone and Norman, 1992; De Villiers and Hawley, 2003).

On the other hand, the partial differential equations in the HARM code are in conservative form as they are derived from the formulation of conservation of mass, momentum, and energy. HARM is a finite-volume code with a Harten, Lax, van Leer (HLL) shock-capturing scheme (Harten, Lax, and van Leer, 1983) that solves the hyperbolic system of partial differential equations in the standard Valencia conservation formalism (Papadopoulos and Font, 1999). The integrated equations in HARM are of the form

$$\partial_t \boldsymbol{U}(\boldsymbol{P}) = -\partial_i \boldsymbol{F}^i(\boldsymbol{P}) + \boldsymbol{S}(\boldsymbol{P}). \tag{2.12}$$

Here, $\boldsymbol{U}$ is a vector of conserved variables like particle number density, or energy or momentum, $\boldsymbol{F}^i$ are the fluxes in finite control volume, and $\boldsymbol{S}$ is a vector of the source terms. Here $\boldsymbol{U}$ is conserved in the sense that it only depends on the fluxes at the boundary if $\boldsymbol{S} = 0$. Vector $\boldsymbol{P}$ comprises primitive variables like rest-mass density, internal energy density, components of velocity and components of magnetic field. These primitive variables are interpolated to model the flow within the zones. This means that $\boldsymbol{U}$ and $\boldsymbol{F}^i$ depend $\boldsymbol{P}$. So, a set of conserved variables is updated at each time step using the fluxes. The flow inside a grid zone is modeled through interpolation, using the chosen primitive variables. Now, the vector of conserved variables is updated instead of the primitive variables. A conservative numerical scheme is used to compute the vector of conserved variables $\boldsymbol{U}$. Once the conserved variables are known, the vector of primitive variables $\boldsymbol{P}(\boldsymbol{U})$ is calculated, once or twice per time step depending on the order of the scheme. A summary of the conservative scheme at one time step is given in Figure 2.1.

The HARM scheme solves equations represented by Equation 2.12. These involve a vector $\boldsymbol{U}$ of conserved variables such as particle number density, energy, or momentum density in the coordinate frame. $\boldsymbol{F}^i$ represent the fluxes, while $\boldsymbol{S}$ represents a vector of source terms that do not involve derivatives of $\boldsymbol{P}$. Thus the source terms do not affect the characteristic structure of the system. In non-relativistic MHD, both $\boldsymbol{P} \rightarrow \boldsymbol{U}$ and $\boldsymbol{U} \rightarrow \boldsymbol{P}$ possess a closed form solution. However, this is not the case in GRMHD as $\boldsymbol{U}(\boldsymbol{P})$ will be a complicated non-linear relation. The inversion $\boldsymbol{P}(\boldsymbol{U})$ is calculated numerically once or twice per each time step. The transformation between the conserved and primitive variables requires solving a set of non-linear equations which are done numerically as well. The pure HLL scheme does not preserve any numerical representation of divergence free magnetic field. HARM instead uses a version of constrained transport that can be combined with a zone-centered evaluation. This idea was first introduced by Tóth, 2000, where it is called flux-interpolated constrained transport (flux-CT) scheme. This scheme preserves a numerical representation of $\boldsymbol{\nabla}.\boldsymbol{B} = 0$ by smoothing out the fluxes with a special operator.

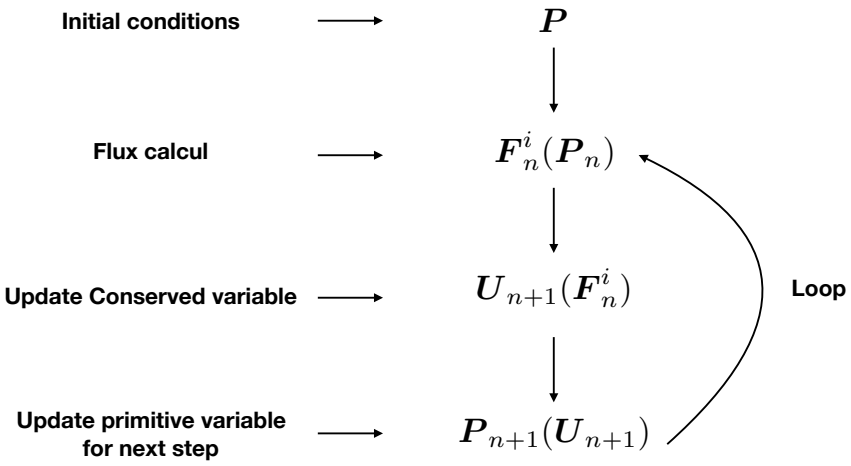

FIGURE 2.1: The summary of a conservative scheme of order 1 at a time step. Here n denotes the time step. The figure is adapted from Janiuk et al., 2018

To ensure accurate solutions when solving hyperbolic partial differential equations using numerical methods, it is also necessary to follow the Courant condition (Courant, Friedrichs, and Lewy, 1967). This condition limits the duration of time steps during computer simulations. Explicit methods use the current system state to calculate the state at a later time, while implicit techniques incorporate both current and subsequent states to derive an answer. HARM's time step uses explicit methods to calculate states that satisfy the Courant condition.

At the beginning of each simulations, we set the initial conditions from which the fluxes are calculated which in turn update the conservative variables. Then, the primitive variables get updated for the next time step using the conserved variables and the code advances in time steps. We prescribe the initial conditions for our models in the Boyer-Lindquist coordinates, and then they are transformed to the code coordinates, the Kerr-Schild (KS) coordinates (Weinberg, 1972; Visser, 2007), before the initial time step.

2.1.3 Grid and coordinate setup

HARM uses a modified version of the spherical Kerr-Schild (MKS) coordinates for its internal grid. In the KS coordinates, matter can accrete smoothly through the black hole horizon and thus the flow evolution can be tracked properly without encountering any coordinate singularities. The grid has been adjusted to be logarithmic in radius near the black hole and super-exponentially spaced in the outer region to achieve finer resolution closer to the black hole. In the polar code coordinates, we also put an option to adjust the grid spacing close to the equatorial plane which can be useful in the evolution of accretion disk flows. In the code, the KS radius r has been replaced by a logarithmic radial coordinate $x^{[1]}$ such that

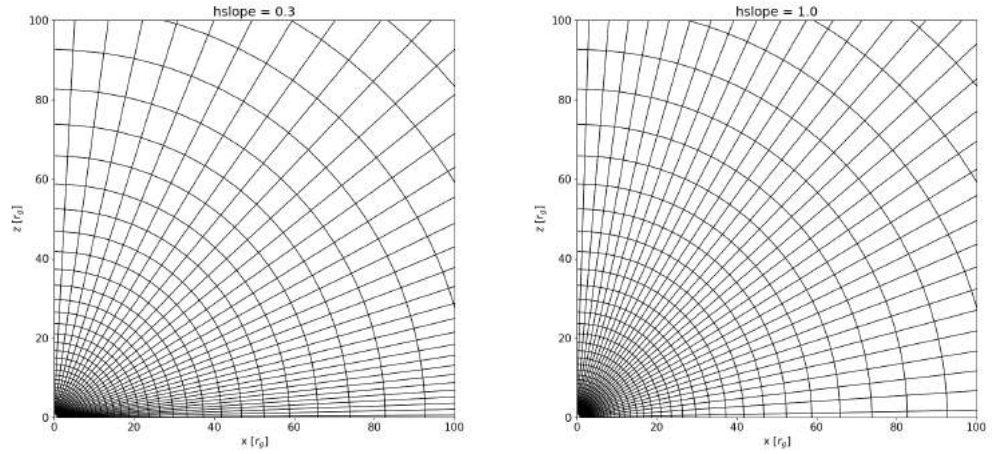

FIGURE 2.2: Simplified plot of the HARM numerical grid showing the varied concentration of angular resolution near the equatorial plane with (a) h_{slope} = 0.3, and (b) h_{slope} = 1.0, up to a radius of 100 r_g.

$$r = e^{x^{[1]}}, \tag{2.13}$$

the KS latitude θ has been substituted by $x^{[2]}$ such that

$$\theta = \pi x^{[2]} + \frac{(1-h)}{2} sin(2\pi x^{[2]}) \tag{2.14}$$

and the azimuthal angle ϕ is kept the same,

$$\phi = x^{[3]}. \tag{2.15}$$

We can adjust the value of h (called 'h_{slope}' in the code) in Equation 2.14 to concentrate more grid cells near the midplane. We used the values of 0.3, 0.5 and 1.0 for the h_{slope} parameter in our different models in this thesis, depending on the configuration. The simplified grid shapes when two of these values are used are plotted in Figure 2.2.

2.1.4 Example initial configuration of fluid distribution and magnetic field

We usually begin our simulations in the HARM code with idealized equilibrium initial configurations of steady state accretion disks or a spherically symmetric inflow.

For example, a typical steady state thick disk solution for a fluid in Kerr geometry is given by Fishbone & Moncrief (FM) (Fishbone and Moncrief, 1976), which is used as an initial condition in many fiducial GRMHD disk models. In the FM model, the angular momentum distribution is given by

$$\ell_* = \frac{\ell}{1 - \Omega\ell} = \text{constant}, \tag{2.16}$$

where ℓ_* is a constant across any given disk. The orbital frequency is given by

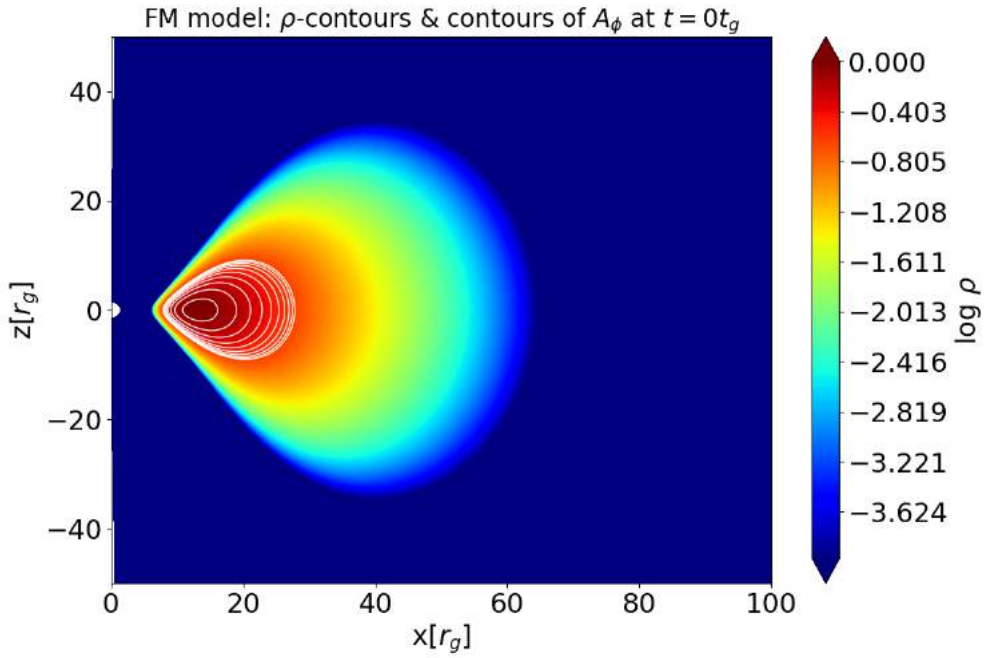

FIGURE 2.3: Example initial configuration of density and magnetic field with the Fishbone-Moncrief disk and a poloidal magnetic field that follows the contours of disk density (given by the vector potential in Equation 2.19). The density contours are shown in the color scale while the contours of the magnetic vector potential, which is equivalent to the magnetic field lines in this case, are shown with the white lines.

$$\Omega = -\frac{g_{\phi\phi} + (g_{\phi\phi}^2 - 4\ell_* g_{tt} g_{\phi\phi})^{1/2}}{2\ell_* g_{\phi\phi}}, \tag{2.17}$$

and the enthalpy W has the form,

$$W = -\ln A + \ell_* \Omega, \tag{2.18}$$

where A is the redshift factor given by $A = (g_{tt} + g_{\phi\phi\Omega^2})^{-1/2}$. These initial conditions are prescribed in Boyer-Lindquist coordinates in the code. Then the density and velocity distributions of the fluid are calculated from this prescription according to the values of the radius of maximum pressure (*rmax*) and the radius of inner edge (*rin*) of the disk that we choose at the initial time.

The FM disk is a steady-state solution and it will stay unchanged in time (only being unstable to small numerical instabilities) unless there is some mechanism to perturb this configuration. For this purpose, we introduce the magnetic field of chosen strength in addition to this solution so that the fluid becomes a magnetized plasma. Various initial magnetic field configurations are possible including axisymmetric poloidal and toroidal configurations or even non-axisymmetric fields. The choice is rather arbitrary as one does not clearly know which configurations are most prevalent in nature. In our models, we chose to work with purely poloidal field configurations prescribed by the form of the magnetic vector potential $\boldsymbol{A}$. For a purely poloidal field, the only non-vanishing component of the vector potential will

be A_ϕ. For example, the form of the vector potential $\boldsymbol{A}$ for a poloidal field which follows the contours of the disk density is given by

$$A_\phi = (\bar{\rho}/\rho_{max}) - \rho_0 \tag{2.19}$$

and $A_r = A_\theta = 0$. Here, $\bar{\rho}$ is the density in the disk (averaged over 2 neighbouring cells), ρ_{max} is the maximum density and ρ_0 is an offset value to restrict the field lines to the regions where the density in the disk is larger than a threshold value (e.g. $0.2 \times \rho_{max}$). Figure 2.3 shows the output plotted from the HARM code with the example initial configuration described here. The strength of the magnetic field is set by the plasma-β parameter which was described earlier. The magnetic field configurations used in our specific models are explained in the relevant chapters. A few other possible field geometries and their time evolution are explored in Kološ and Janiuk, 2020.

2.2 Code performance

The convergence of the HARM scheme in the hydrodynamical as well as magnetized regimes are discussed in the original article (Gammie, McKinney, and Tóth, 2003).

For a demonstration of the convergence of physically relevant quantities, we choose the mass accretion rate (that is saved in the code diagnostics, more frequently than other data dumps), for a fiducial FM disk model, and note here its dependence on the resolution. Figure 2.4 shows the mass accretion rate with time, depending on the resolution, for the models with two types of initial conditions. The first condition is that of the non-magnetized case. For this model, we made two runs at the resolutions 512×512 and 1024×1024 (in the r and θ directions respectively) as shown in the plot. In this case, we expect that there will be no accretion of mass to the black hole as the Fishbone-Moncrief solution describes a steady state solution. The only accretion of mass possible should be from any numerical instabilities and it should be negligibly small. This is the case we observe from our model, when run in two resolutions. In this cases, the value of accretion rate is independent of the resolution and they stay negligibly small as long as we keep running it. When we turn on the magnetic field it results in the MRI and drives the accretion after a certain initial time has passed. This can be noticed in the last three runs presented in the plot (for the resolutions of 256×256, 512×512 and 1024×1024). In the case of magnetized accretion, we note that the value of accretion rate depends on the resolution. In this case, it is always better to use higher resolutions, which is only limited by the computational resources. On the other hand, we can notice from our three runs that even the smallest resolution produces similar values of mass accretion rate when compared to the highest resolution we tried. It can also be noted that the models run at higher resolutions produces slightly higher mass accretion rates, especially the the values of spikes.

The HARM code works in 1, 2, and 3-Dimensions. For optimal and timely results, it is crucial to parallelize any practical 2D or 3D simulation. HARM has been improved through the adoption of the Message Passing Interface (MPI) and a more robust Hybrid parallelization mechanism. This enhancement ensures efficiency in both 2D and 3D runs. By using hybrid programming techniques, we combine distributed and shared memory applications, which allows more processor cores to be committed to a numerical simulation. Our approach involves dividing the computational domain into slices, with each MPI process utilizing a small memory space. Our version of the HARM code is parallelized in the r (N1) and ϕ (N3) directions.

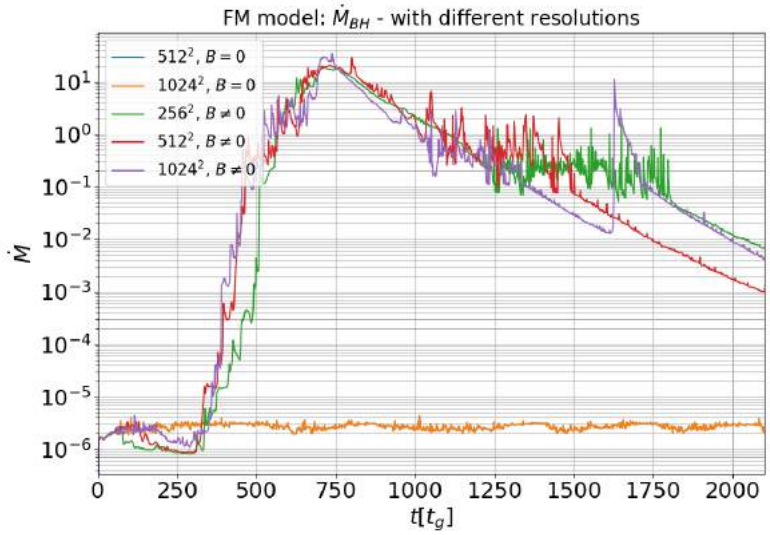

FIGURE 2.4: Mass accretion rate at the black hole horizon ($\dot{M}_{BH}$) for the Fishbone-Moncrief model, with different 2D (r, θ) resolutions, for the non-magnetized and magnetized cases.

Here N1, N2 and N3 represents the number of grid cells in the (r, θ, ϕ) directions respectively. So we do not slice the computational domain in N2 (θ-direction). Figure 2.5 shows the mass accretion rate in parallel runs with different number of CPU cores, and it shows the proper implementation of the parallelization scheme. The accretion rate stays the same value regardless of the number of CPU cores used and it is the case for two different initial conditions we tested.

More detailed performance tests and implementation details of the version of HARM code used in this thesis are presented in some earlier works (e.g. Janiuk et al., 2018; Sapountzis and Janiuk, 2019).

The standard data outputs from the HARM runs can be stored either in ASCII or HDF5 formats. These outputs include the code initialization values (written only at the beginning of the simulations and includes grid shape, coordinates and similar quantities which are constant in time) and periodic outputs which contains the results of the integration and the physical quantities of the flow (like density, internal energy, etc.). We use tools including common Python libraries, and other visualization software (e.g. VisIt) to analyze the data from these outputs. There is also an option to save some physically relevant quantities (e.g. mass accretion rate), more frequently than the data dumps, as part of the code diagnostics.

Hardware resources used

The simulations presented in this thesis were performed with the high-performance computing (HPC) infrastructure available in Poland. A very brief overview of the computational hardware and the resources used for the simulations presented in this thesis is presented here. The 2D simulations presented in Chapter 3 were done with a resolution of 768×512 in the r and θ directions, respectively. The 3D simulations presented in Chapter 4 were done with a resolution of $288 \times 256 \times 128$ in the r, θ and ϕ directions respectively. Since HARM is a CPU-based code, the CPU configuration used in our main runs is mentioned here. The simulations presented in

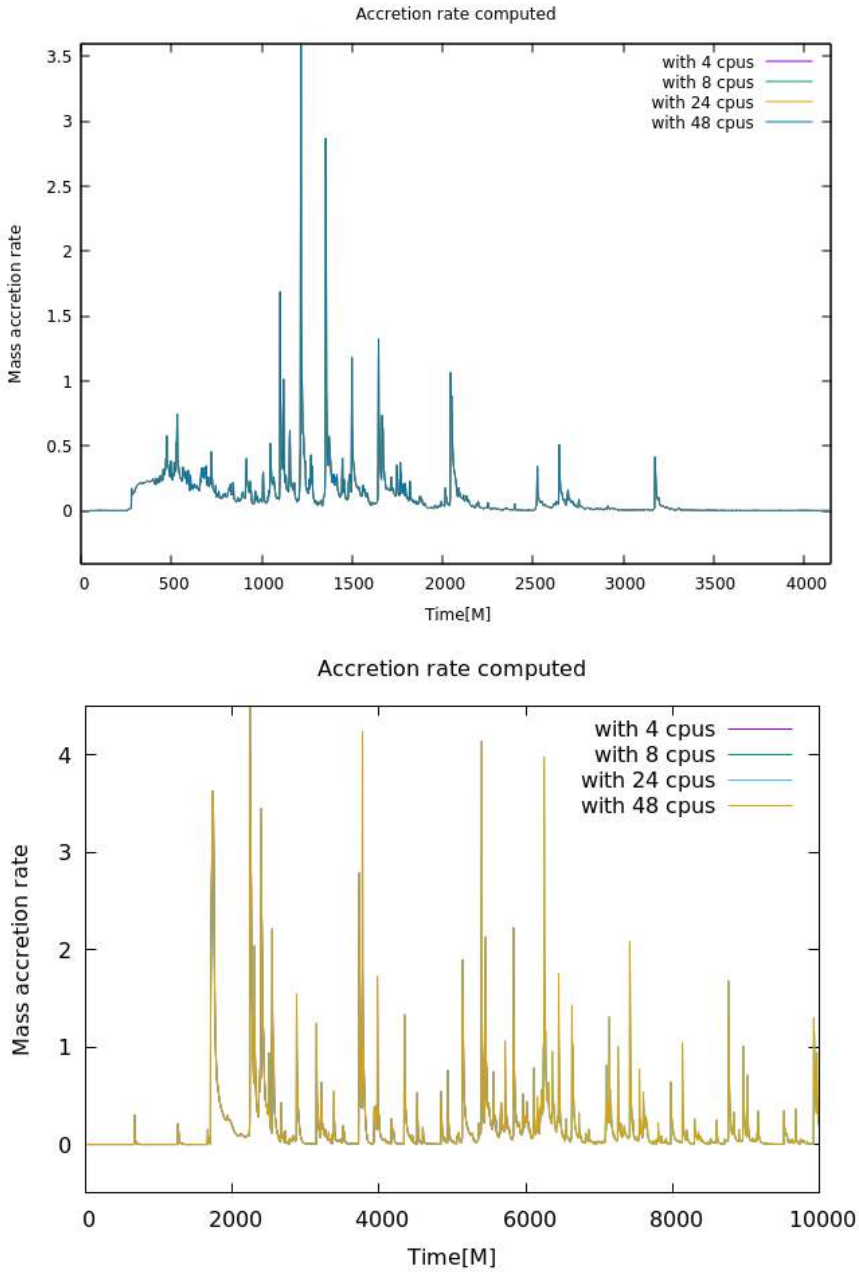

FIGURE 2.5: Mass accretion rate at the black hole horizon for the Fishbone-Moncrief (top) and Chakrabarti initial conditions (bottom) embedded in a poloidal magnetic field, with different number of CPUs in parellel run (at the same resolution)

both the chapters mentioned above were done mainly with the *Okeanos* supercomputer at the Interdisciplinary Center for Mathematical and Computational Modeling of the University of Warsaw (ICM UW). It is a Cray XC40 large-scale processing system with 1084 computational nodes. Each of these nodes possesses 24 cores of Intel Xeon Haswell CPUs, paired with 128 GB RAM. All the computing nodes are interconnected with the Cray Aries network with Dragonfly topology. For each 2D model presented in Chapter 3, 8 CPU nodes were used for about $\sim$ 10 hours. On the other hand, each 3D simulation presented in Chapter 4 used 48 CPU nodes for a period of $\sim$ 2 weeks. The 2D models presented in Chapter 5 were run with a resolution of 600×512 cells in the r and θ directions respectively. For these models, we used the cluster *Topola* at ICM UW which has 28 CPU cores per node and a similar CPU clock speed as of *Okeanos*. These simulations took a time of about $\sim 5-6$ hours for each model. For the 3D simulations presented in this chapter with a resolution of $288 \times 256 \times 128$, we used the *Ares* supercomputer which is part of the PL-grid infrastructure. It is a relatively new cluster presently under expansion and currently possesses 788 CPU nodes with up to 384 GB RAM per node. Each of these nodes includes 24 CPU cores but at a higher clock speed than that of *Okeanos*. Each 3D model presented in Chapter 5 used 48 CPU nodes on *Ares* for a period of $\sim$ 5 days.

Chapter 3

Variability studies of jets from accreting black hole sources at different mass scales

This chapter presents a published article which is based on the work done by me in the first and second years of my doctoral studies.

In this chapter, we present a study of the time variability properties of jets launched from accreting black hole sources at different mass scales. As the HARM code is scale-free (with $G = c = M_{\rm BH} = 1$), we use the results from our simulations for models ranging from stellar-mass black holes to supermassive ones. In this study, we investigated the disk-jet connection in terms of the disk magnetization (quantified by the plasma β parameter) and the black hole spin (quantified by the dimensionless Kerr parameter a) with the jet properties quantified by the jet Lorentz factor and its variability in time. This investigation was motivated by the correlations found between the observed values of jet Lorentz factors and minimum variability timescales as noticed by different authors, for the case of GRBs (Sonbas et al., 2015) and the case of GRBs and blazars together as well (Wu et al., 2016).

This project was done in collaboration with my supervisor Prof. Agnieszka Janiuk and also with Ishika Palit, who was then a PhD student in my group. All the simulations and data analysis in this work were done by me, except for the power density spectral data analysis given in sections 4.1 - 4.2 in the article.

We conducted 2D axisymmetric simulations of magnetized accretion disks around Kerr black holes for this investigation. Our models self-consistently resulted in nonuniform jets, which we analyzed in terms of jet energetics and time variability. We examined three different families of models and determined the idealized time-averaged jet Lorentz factor and its minimum variability timescale (MTS) for each one. Our study illustrates the relationships between jet properties and the characteristics of central engines in gamma-ray bursts and blazars.

The Astrophysical Journal, 917:102 (9pp), 2021 August 20 https://doi.org/10.3847/1538-4357/ac0624

Variability of Magnetically Dominated Jets from Accreting Black Holes

Agnieszka Janiuk, Bestin James, and Ishika Palit
Centrum Fizyki Teoretycznej PAN, Al. Lotników 32/46, 02-668 Warsaw, Poland
Received 2020 December 28; revised 2021 May 25; accepted 2021 May 26; published 2021 August 24

Abstract

Structured jets have recently been invoked to explain the complex emission of gamma-ray bursts (GRBs), such as GW170817. Based on accretion simulations, the jets are expected to have a structure that is more complex than a simple top-hat structure. Also, the structure of the launch regions of blazar jets should influence their large-scale evolution. This was recently revealed by the interactions of jet components in TXS 0506+056, where the jet was observed at a viewing angle close to zero. Observational studies have also shown an anticorrelation between the jet variability, measured, e.g., by its minimum variability timescale, and the Lorentz factor, which spans several orders of magnitude and covers both blazars and GRBs samples. Motivated by those observational properties of black hole sources, we investigate the accretion inflow and outflow properties by means of numerical gamma-ray MHD simulations. We perform axisymmetric calculations of the structure and evolution of a central engine, composed of a magnetized torus around a Kerr black hole that is launching a nonuniform jet. We probe the jet energetics at different points along the line of sight, and we measure the jet-time variability as localized in these specific regions. We quantify our results by computing the minimum variability timescales and power density spectra. We reproduce the MTS–Γ correlation and we attribute it to the black hole's spin as the main driving parameter of the engine. We also find that the power density spectral slope is not strongly affected by the black hole's spin, while it differs for various viewing angles.

Unified Astronomy Thesaurus concepts: Magnetic fields (994); Kerr black holes (886); Accretion (14); Magnetohydrodynamics (1964); Gamma-ray bursts (629); Blazars (164); Relativistic jets (1390)

1. Introduction

Highly variable accretion flows are found in a number of different types of astrophysical black hole sources. At the largest scales, they are present in the cores of active galaxies. In radio-loud objects, such as blazars, the variability of the inflow can be transmitted to the outflow properties. In these sources, the relativistic jets point to our line of sight. In addition, many similarities are found between the jet physics in blazars and in gamma-ray bursts (GRBs). The latter are observed from extragalactic distances, but operate at smaller scales, within stellar-mass accreting black holes and in a collapsing star's environment. Blazars and GRBs share the properties of their jets, despite different Lorentz factors and accreting black hole masses (Wu et al. 2016). Launching and collimation mechanisms are common: thick disk or corona, pressure gradient in a surrounding wall, external (matter-dominated) jet, or toroidal magnetic field. Acceleration of jets occurs due to both a magnetic field action field and accretion-disk rotation (see Fragile 2008 for a review). The blazar jets are Poynting-dominated, and powered by the Blandford–Znajek mechanism which can extract energy from a rotating black hole. This mechanism is now well known and tested for the purpose of a jet launch, but observations show variability in the jet emission. Multiple shocks that collide in the jet can lead to multiple emission episodes and can account for the fluctuating light curves of GRBs (Kobayashi et al. 1997). A reasonable interpretation of this effect is that the variability observed in the jets can directly reflect the central engine variability. The latter is tightly related to the action of magnetic fields in the center of the galaxy, or in the GRB central engine. Furthermore, the structure of a jet at its base is possibly much more complex than a simple top-hat structure and can be revealed by the afterglow observations and interactions of the large-scale jet with the surrounding medium, e.g., with the postmerger wind in GW170817 (Urrutia et al. 2021). Even though the observed light curves and spectra are primarily the result of the jet's interaction with the circumburst medium, the initial structure of the jet at its base also affects the final emission. Also, interactions are possible between the different components of precessing blazar jets, such as in TXS 0506 +056 (Britzen et al. 2019).

The variable energy output from the central engine implies the varying jet Lorentz factor, as shown, e.g., by Sapountzis & Janiuk (2019). This may lead to occurrence of internal shocks, and affect the observed variability of both GRBs and blazars (Begelman et al. 2008; Bromberg & Tchekhovskoy 2016). Unification of the models across the black hole mass scale, from GRBs to blazars, is not straightforward though. The most uncertain aspect is whether the magnetically arrested disk (MAD) state drives the jets in both types of source, or rather halts the GRB emission, as studied by Lloyd-Ronning et al. (2018). In the MAD mode, the flux accumulated at the black hole horizon, and the interchange instability rather than magnetorotational instability (MRI) governs the minimum timescale of variability (Tchekhovskoy et al. 2011, 2014). In contrast, in the standard and normal accretion evolution (SANE) mode, the MRI dives variability of the jets, as directly related to the accretion variability timescales (Penna et al. 2013; Porth et al. 2019). Finally, the blazar disks are subject to different physical conditions than the GRB disks, and in the latter, thermal instabilities of the neutrino-dominated accretion flows may play a role, also triggering the episodic jet ejections (Janiuk & Yuan 2010; Cao et al. 2014)

Here we explore the scenario of magnetically driven accretion and jet variability related to the MRI timescale. We confirm the existence of the correlations between the inferred minimum variability timescale and magnetic field strength as

well as the black hole spin, as expected for the Blandford–Znajek-driven jets. We compare the resulting timescales with observed ones, taken from the sample by Wu et al. (2016), and conclude that they represent both classes of sources, namely blazars and GRBs, well.

2. Model

We present here the two-dimensional magnetohydrodynamical models computed in full general relativity (general relativistic magnetohydrodynamics, GR MHD). The numerical scheme is our implementation of the code HARM (Gammie et al. 2003; Janiuk et al. 2013; Sapountzis & Janiuk 2019). Our initial condition assumes the existence of a pressure equilibrium torus, embedded in the poloidal magnetic field (Figure 2, top). Such 2D studies of a compact magnetized tori around black holes have already been performed by different groups (McKinney et al. 2012; Fernández & Metzger 2013; Sądowski et al. 2015; Qian et al. 2017). Our approach is based on similar methodology, while the focus of the present study is given to measuring the variability of the jet. The novel aspect of our analysis is that we consider a structured jet morphology and we attempt to compare our results with some observables.

The jet launched from the central engine is powered by a rotating black hole and mediated by magnetic fields. The Kerr black hole accretes matter from the torus, and its rotation affects the magnetic field evolution. The models are parameterized with the black hole's spin and the initial magnetization of the matter. Code works in a GR framework, so dimensionless units are adopted, with $G = c = M = 1$. Hence, geometrical time is given as $t = GM/c^3$, where M is the black hole's mass. In this way, we are able to model the launch and variability of jets in both a supermassive black hole environment and in GRBs.

The chosen configuration of the torus structure is that of Chakrabarti (1985). Here, the angular momentum distribution has a power-law (PL) relation with the von Zeipel parameter $\lambda = (l/\Omega)^{1/2}$, where l denotes the specific angular momentum and Ω denotes the angular velocity. The size of the torus is fixed in geometrical units, and its inner radius is located at $r_{\rm in} = 6r_g$, its density maximum at $r_{\rm max} = 16.5r_g$, and the outer edge at about $r_{\rm out} = 40$.

We embed the initial torus in a poloidal magnetic field that was proven to drive the bipolar jets after the initial configuration has been relaxed (see, e.g., Liska et al. 2020, however, for recent results with toroidal field initial configurations). We chose the magnetic field configuration produced by a circular current, the same as in Sapountzis & Janiuk (2019). The only nonvanishing component of the vector potential is given by:

$$A_\phi(r,\,\theta) = A_0 \frac{(2 - k^2)K(k^2) - 2E(k^2)}{k\sqrt{4Rr\sin\theta}} \qquad (1)$$

$$k = \sqrt{\frac{4Rr\sin\theta}{r^2 + R^2 + 2rR\sin\theta}},$$

where E, K are the complete elliptic functions and A_0 is used to scale the magnetic field and the initial gas to the magnetic-pressure ratio, $\beta = p_{\rm gas}/p_{\rm mag}$, across the torus.

We define the family of models with varying magnitudes of β, normalizing them to the maximum value within the torus (the point where β reaches its maximum also depends on the black hole spin parameter, a, because of the properties of torus solution for the gas-pressure distribution). Our family of models is depicted in Figure 1.

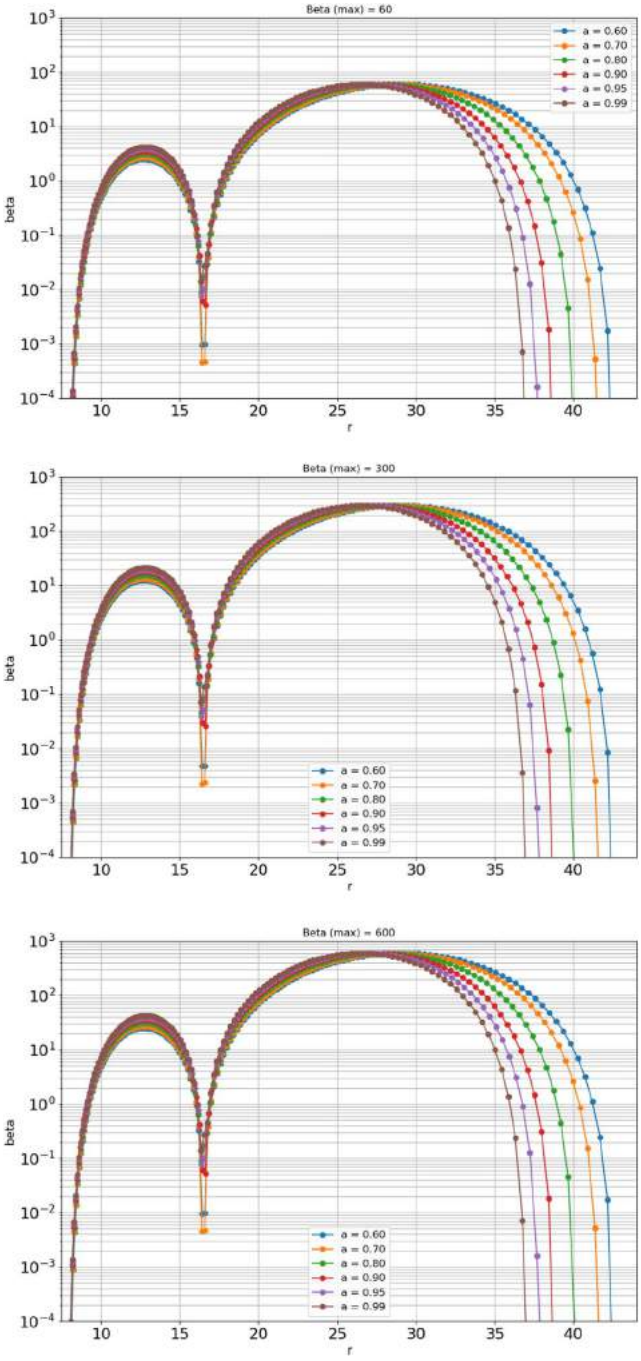

Figure 1. Initial distribution of the gas to magnetic-pressure ratio, β, in the torus at time $t = 0$. The models are normalized to $\beta_{\rm max} = 600$, 300, and 60. Values of the Kerr parameter are $a = 0.6$, 0.7, 0.8, 0.9, 0.95, and 0.99.

In all our simulations we used the resolution of 768×512 grid points in (r, θ) directions. This allowed us to keep a proper MRI resolution, defined as the minimum number of cells per MRI wavelength (Siegel & Metzger 2018).

3. Results

The initial configuration of an equilibrium torus as given by the solution of Chakrabarti (1985) is depicted in Figure 2. The

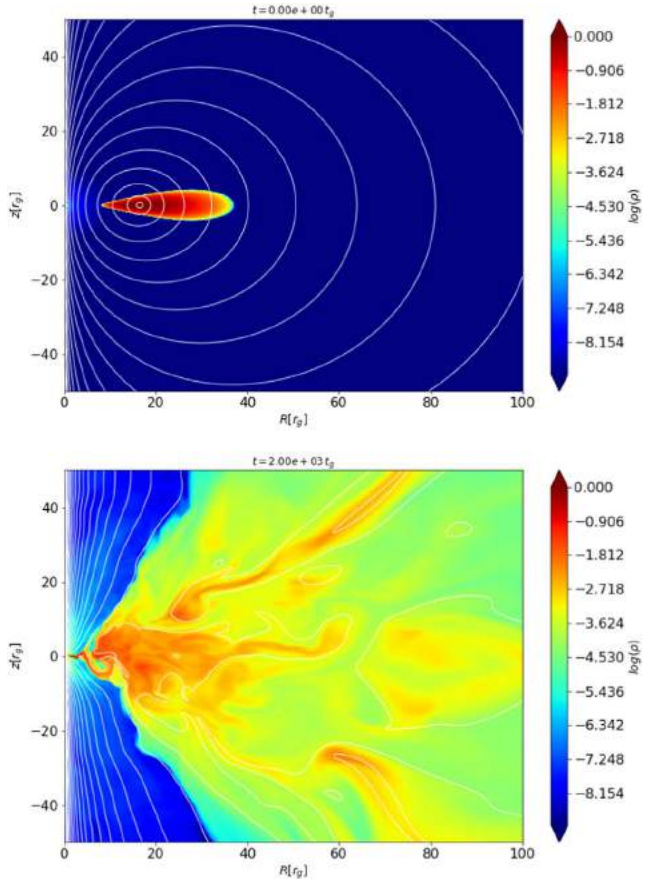

Figure 2. Initial conditions and evolved state. Torus density structure and magnetic field contour lines at time $t = 0$ and at time $t = 2000\,M$ are plotted for the model with $\beta_{\rm max} = 60$ and Kerr parameter $a = 0.99$.

top panel shows the flattened structure of density enclosed within the region of about $40r_g$. The geometrical thickness of the structure is less than $H/r = 0.2$. The solution shown in the plot is parameterized by the black hole spin $a = 0.99$.

The inner edge of the torus is $r_{\rm in} = 6r_g$ and the position of maximum pressure in the torus is $r_{\rm max} = 16.5r_g$. All the simulations start from this initial configuration and evolve afterwards. The value of λ ranges between 0.04–10.21 M within the torus. The outer radius of the torus is affected by change in Kerr parameter a and $r_{\rm in}^{\rm (vonZeipel)}$. The surfaces of constant specific angular momentum l and angular velocity Ω are called the von Zeipel cylinders. With the choice of Chakrabarti's solution for the torus structure, $l = constant$ surfaces become the von Zeipel cylinders. The $r_{\rm in}^{\rm (vonZeipel)}$ parameter represents the true inner edge of the torus and is kept at $8r_g$ for all the models in the simulation to constrain the outer radius of the torus near to $40r_g$. We note that using bigger values for $r_{\rm in}^{\rm (vonZeipel)}$ would reduce the size of the torus. By changing the Kerr parameter from $a = 0.60$ to 0.99, we can change the outer radius of torus from 42.5 to $37r_g$. The average value of β within the torus is calculated from the inner point in the torus where the value rises above 10^{-3} to the outer point in the torus where the value falls below 10^{-3}.

The magnetic field imposed on top of the stationary torus configuration has an electric wire shape, with circular loops concentrated on the pressure maximum radius. This radius was chosen as $16.5r_g$ for all models. The magnetic field allows

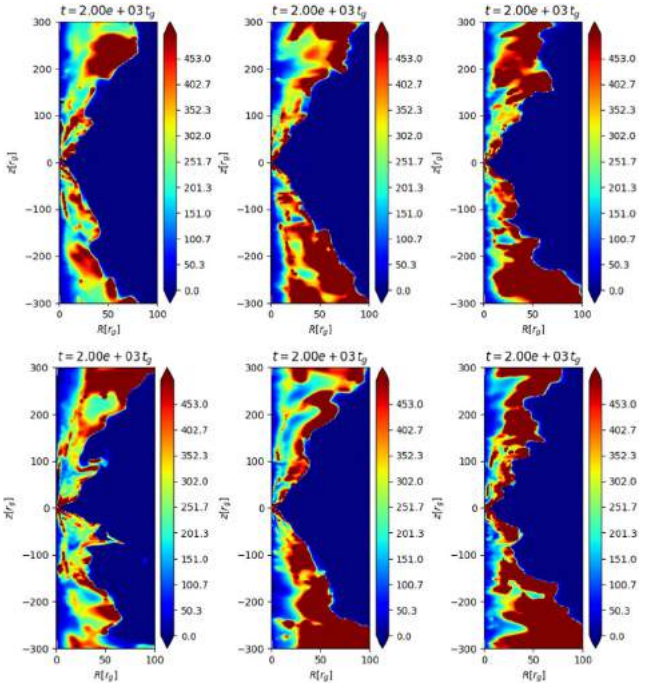

Figure 3. Jet structure at time $t = 2000\,M$. The figure shows the distribution of energetics defined as μ (see Equation (2)). Top row: models with $\beta_{\rm max} = 600$. Bottom row: models with $\beta_{\rm max} = 60$. The models display jets launched from spinning black holes with the Kerr parameter of $a = 0.6$ (left column), $a = 0.8$ (middle column), and $a = 0.95$ (right column).

material to start to accrete onto the black hole. The evolved structure of the flow, which has already relaxed from its initial configuration, is depicted in the bottom panel of Figure 2.

In our simulation the accretion flow has an axisymmetric configuration. To assess the MADness of the dynamical solution, we would need to cover the nonaxisymmetric modes. However, even in our setup we can evaluate the ratio between the magnetic flux and mass-accretion rate on the black hole's horizon. In fact, the magnetically arrested state appears in the most-magnetized models, i.e., those with $\beta_{\rm max} = 60$. At the beginning of the simulation, before time $t = 2000\,t_g$, the parameter $\Phi_{\rm BH} = \frac{1}{2\sqrt{M}}\int |B^r(r_H)| dA_{\theta\phi}$ is greater than 10 (note that in our code we use the Gaussian units, so the factor 4π is not incorporated in the magnetic flux).

The jet energetics determine the Lorentz factor at infinity, and as was shown by Vlahakis & Königl (2003) and Sapountzis & Janiuk (2019) it is given by the μ parameter. It is defined as

$$\mu = -\frac{T_t^r}{\rho u^r} \tag{2}$$

where T_t^r is the energy component of the energy-momentum tensor, which consists of gas and magnetic parts, ρ is the gas density, and u^r is the radial velocity, i.e., the total plasma energy flux normalized to the mass flux. It is therefore given by the sum of the inertial–thermal energy of the plasma and its Poynting flux, which can be transferred to the bulk kinetic energy of the jets at large distances.

The distribution of the jet-energetics parameter in an evolved state of the simulation is shown in Figure 3. The snapshots compare two values of magnetic field normalizations, $\beta = 600$

Table 1
Summary of the Models Studied

$\beta_{\max}$ in Torus	Average β	Spin (a)	MTS	Lorentz Factor Γ		
				Point 1	Point 2	Average
$\beta_{\max} = 600$	145.54	0.99	19.73	347.26	602.29	474.77
	145.86	0.95	26.40	280.66	594.80	437.73
	146.87	0.90	25.34	265.89	505.47	385.68
	148.43	0.80	36.88	268.89	435.86	352.38
	149.70	0.70	35.56	256.27	404.21	330.12
	151.01	0.60	39.66	223.22	343.72	283.47
$\beta_{\max} = 300$	73.35	0.99	24.20	337.80	651.93	494.87
	74.07	0.95	26.55	301.88	584.01	442.94
	73.99	0.90	28.31	281.92	476.51	379.21
	74.76	0.80	31.98	257.70	491.84	374.77
	74.85	0.70	31.61	248.67	428.22	338.44
	75.50	0.60	45.65	228.90	332.53	280.71
$\beta_{\max} = 60$	14.91	0.99	22.91	359.43	1000.72	680.08
	14.93	0.95	23.15	234.38	607.69	421.03
	14.91	0.90	26.73	230.75	479.02	354.89
	15.06	0.80	34.75	225.11	377.68	301.40
	15.41	0.70	31.15	204.59	314.61	259.60
	15.42	0.60	43.14	192.39	309.97	251.18

Note. Three families of models differ with respect to the magnetic field normalization, which is scaled with the maximum value of the gas to magnetic-pressure ratio within the torus (note that $\beta(r_{\max})$, the value at the radius of pressure maximum, can be as small as 10^{-3}–10^{-2}, see Figure 1, so that all our models are essentially representing strongly magnetized tori). We also give the value of the average value of β in the second column. The third column gives the value of the black hole Kerr parameter, a, for each model. The resulting variability timescale and Lorentz factor measured as the averaged energetics parameter at two chosen points in the jet are given in the last two columns.

and $\beta = 60$, in the top and bottom rows, respectively. We show three different values of black hole spin, $a = 0.6$, 0.8, and 0.95. We note highly inhomogeneous outflows, where larger values of μ are reached at the edges of the jets rather than at the z polar axis. From the color scales of the distribution it can already be seen that more energetic jets are produced from rapidly spinning black holes, which confirms our intuitions. The relation with magnetization β is not that clear though, and it seems to be affected by the black hole's spin value. The details of the simulation results are therefore summarized quantitatively in Table 1.

The table shows the minimum variability timescale and Lorentz factor values with the changing black hole spin value. Three models with different magnetic field normalizations are shown here. For our calculations the Lorentz factor is taken as the average of μ in time. The averages were calculated from $t = 600$ to $t = 3100 t_g$. The minimum variability timescale is calculated as the average of peak widths at their half maximum on the μ variability plot.

In Figure 4 we show the time variability of jet energetics (i.e., the μ parameter) for the models with a magnetic field normalization $\beta_{\max} = 300$ and different values of black hole spin. The variability is measured here at a chosen specific point, $r = 150 r_g$ and $\theta = 5°$. Here we show the values of μ, from $t = 1000 t_g$ to $t = 3000 t_g$. For each simulation, the parameter μ is computed at two different points located at $r = 150 r_g$, $\theta = 5°$ and $\theta = 10°$.

4. Jet Properties and Central Engine

Here, we investigate the influence of the central engine properties, as scaled by its magnetization, and the Kerr parameter a of the black hole, on the variability and energetics of the jet. The total energetics are described by the parameter μ, which represents the total, thermal, and Poynting energy in the jet. Note that this parameter is dimensionless, as it is given by the ratio of the r component of the linear momentum, to the mass flux across the radial surface (see Equation (2)). Therefore, it can be related to the maximum achievable Lorentz factor, reached at "infinity", and available under the "infinite" efficiency of conversion to the bulk kinetic energy of particles injected to the jet. We identify therefore the time-averaged value of μ as the proxy of the jet Lorentz factor, Γ. The variability is also measured by μ changes with time, at a given point. We propose that the frequency of these changes, measured in the base of the jet, is related to the frequency of collisions between the shells transported downstream by the jet and is the source of observable gamma-ray pulses, produced in the internal-shock scenario (Kobayashi et al. 1997).

The jet structure is clearly nonuniform, and more energetic blobs are always located in the outer regions, while less energetic ones travel close to the axis. This is revealed by the systematic differences between Γ measured at point $p1$, which ranges between ∼200 and 350, and those measured at point $p2$, which is ranges from ∼300 up to 1000 (see Table 1 and the bottom panel in Figure 6). The jet bulk velocity, and hence its power, increases with the black hole's spin, and reaches remarkably average values if the black hole rotates close to the Kerr limit. This is expected to be a result of Blandford–Znajek-driven process. The dependence on the magnetic pressure in the disk, and the β parameter, is not linear, however. Only in the case of the most spinning black hole, $a = 0.99$, and the most-magnetized disk, with average β in the torus on the order of 15 ($\beta(r_{\max}) < 10^{-3}$ and $\beta_{\max} = 60$), is the jet power the largest, compared to more thermally dominated tori. If the black hole does not rotate at close to the maximum Kerr limit, then the more thermally dominated tori, with an average $\beta_{\max}$ of 300, or

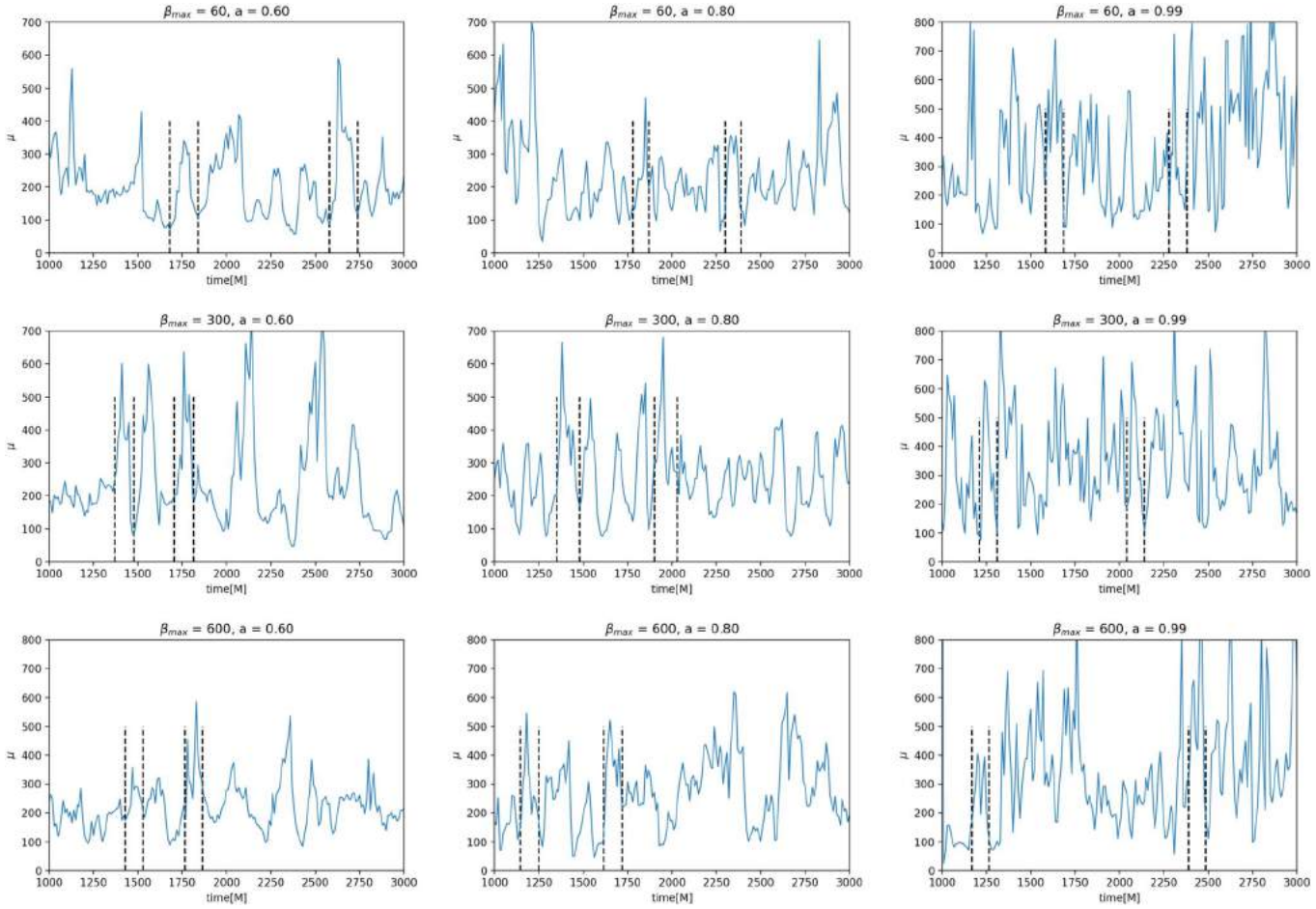

Figure 4. Variability of the jet μ parameter as function of time, for the models with different $\beta_{\max}$ (60, 300, and 600, from top to bottom) and three different values of the Kerr parameter ($a = 0.6$, 0.8, and 0.99, from left to right). The time series are extracted at point p1 in the jet, so at the inclination $\theta = 5°$ to the vertical axis. The dashed lines represent the characteristic timescale of the MRI calculated using the expression for maximum growth rate derived by Gammie (2004).

600 (average β in the torus is 75 or 150, respectively), give more power to the jet. This result can be understood in the frame of magnetically driven transfer of accretion-disk energy to the jet when there is less Poynting flux available in the funnel for less spinning black holes, and while the thermal energy can still be transported through the horizon with enough efficiency. Notably, there is almost no difference between the jet power and angle-averaged Lorentz factors, in the $\beta_{\max} = 300$ and 600 cases. For spins $0.7 \leqslant a \leqslant 0.9$ the point $p2$ meets more energetic blobs for smaller β, while blobs at point $p1$ are found to be more energetic for lager β.

The variability of the jet, studied in terms of the duration of the pulses, is driven by the MRI in the disk. Here, however, some numerical constraints of our simulation, namely spatial resolution and the axisymmetric setup of the models, may also be of some importance. The MRI is resolved in terms of the minimum number of cells per wavelength, as shown in Figure 5. Nevertheless, the duration of the pulses duration only roughly correlates with $t_{\rm MRI}$ (Figure 4), and only the widest pulses clearly show this effect. The narrower pulses, which also contribute to our minimum variability timescale (MTS) and MTS estimate, behave more erratically. Therefore, as displayed in Figure 6 (upper panel), the MTS has a general trend of decreasing with the black hole's spin, but it can either decrease or increase with β, depending on the a value. In particular, we can note that the thermal pulses are shortest for $a = 0.95$ while they are longest for $a = 0.8$.

We note that important information about the jet engine and jet collimation comes from the angular jet structure. Our jet is not uniform and has a distribution of energy content that is both time and angle dependent. Here, we probed how the jet distributes its power and we plot Γ as function of polar angle. We calculated the time-averaged *jet profile* at a radius of $2000\, r_g$, so at a large distance from the black hole. It is presented in Figure 7. The profile shows that most energetic part of the jet is located inside a narrow region at $\theta < 15°$ which is qualitatively very similar to the profiles found in recent 3D black hole jet studies (Kathirgamaraju et al. 2019, see also Nathanail et al. 2021). Compared with those results, our jets are accelerated to a larger Γ, for the same black hole spin. This is due to our magnetization profile and initial different β distribution in the torus, which in those works has been adopted as uniform and larger on average (Fernández et al. 2019).

Finally, we verified whether our results depended on the adopted value of the density floor, i.e., the numerical floor in our simulation. The minimum density in our runs is forced to not drop below $\rho_{\rm min} = 10^{-7}$. As shown already in Sapountzis & Janiuk (2019), the time-averaged value of the energetics μ parameter converged for various adopted density floors (see

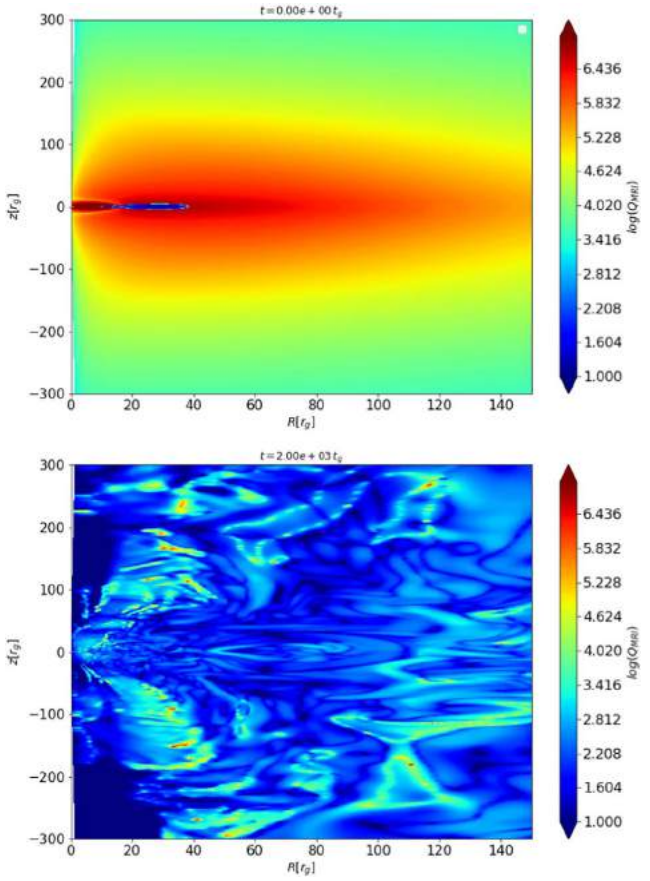

Figure 5. Color contour map of $Q_{\rm MRI}$, defined as the number of grid cells per MRI wavelength, shown in the logarithmic scale at time $t = 0$ and at time $t = 2000\ M$. The plots are made for the model with $\beta_{\rm max} = 300$ and a Kerr parameter $a = 0.9$.

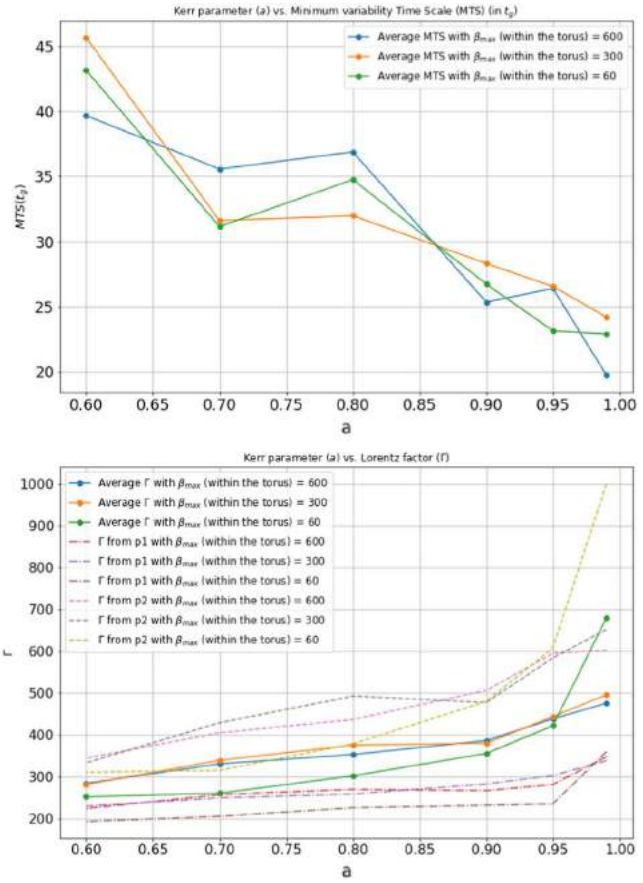

Figure 6. Correlations between (a) the Kerr parameter a and MTS and (b) the Kerr parameter a and Lorentz factor. The upper panel shows results for three families of models, differing with average (and maximum) β parameter: $\beta_{\rm max} = 60$ (green), 300 (orange) and 600 (blue). The MTS is computed as the average duration of the pulses in the μ time series. The values given are averages from the two points p1 and p2. The bottom panel shows results for the Γ factor, defined as the average energetic parameter μ, measured from time 600 until 3000 t_g. Long-dashed lines represent measurements at point p1 in the jet, short-dashed lines are for point p2, and solid lines are the average between two points.

Figure 5 in their paper). Similarly, even though we are using different initial conditions and magnetization in the current models, the density floor value does not significantly affect the time-averaged results, provided it is sufficiently low. We show our testing results in Table 2, where we compare the time-averaged Lorentz factors at two distinct points in the jet. The testing model was used with parameters $a = 0.9$ and $\beta_{\rm max} = 60$.

We also checked that the variability MTS, calculated at different locations in the jet, depended somewhat on the density floor value, however the results do not follow any specific trend. In general, MTS values at point p2 are always smaller than at point p1, and their ratio is about $2/3$ (with an exception of the floor 1×10^{-9}, where the ratio is almost $1/2$).

In order to better understand the jet variability in our models, and also to be able to compare it to observed light curves originating from gamma-ray emission at large distances, we performed a time-series analysis of our modeled sequences.

4.1. Time-series Analysis

We consider the time series of the μ parameter (defined in Equation (2)) in order to carry out a Fourier and power density spectral (PDS) analysis of it. We further impose logarithmic binning to this time series and we plot the averaged values over the bins. Figure 8 shows our simulated data, in a logarithmic scale, corresponding to the model with $\beta_{\rm max} = 60$ and spin

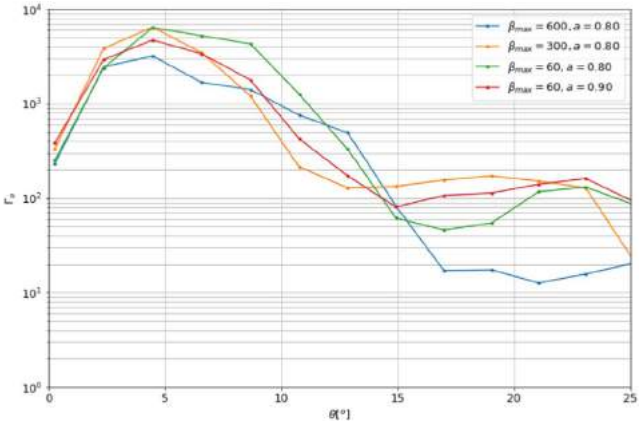

Figure 7. The time-averaged jet Lorentz factor as measured at a distance of 2000 r_g, in the function of polar angle θ. The plot shows the results for four chosen models, differing with the maximum β parameter: $\beta_{\rm max} = 60$ (red and green), 300 (orange), and 600 (blue). The black hole spin was either $a = 0.8$ or $a = 0.9$, as marked in the plot.

Table 2
The Dependence of the Jet Lorentz Factor (Computed from the μ Parameter) on the Adopted Density Floor

Density Floor	Time-averaged Γ	
	From Point p1	From Point p2
1×10^{-17}	258.28	469.20
1×10^{-15}	267.20	577.17
1×10^{-12}	250.00	421.46
1×10^{-9}	237.84	472.90
1×10^{-7} (original simulation)	230.75	479.02
1×10^{-5}	113.15	239.35

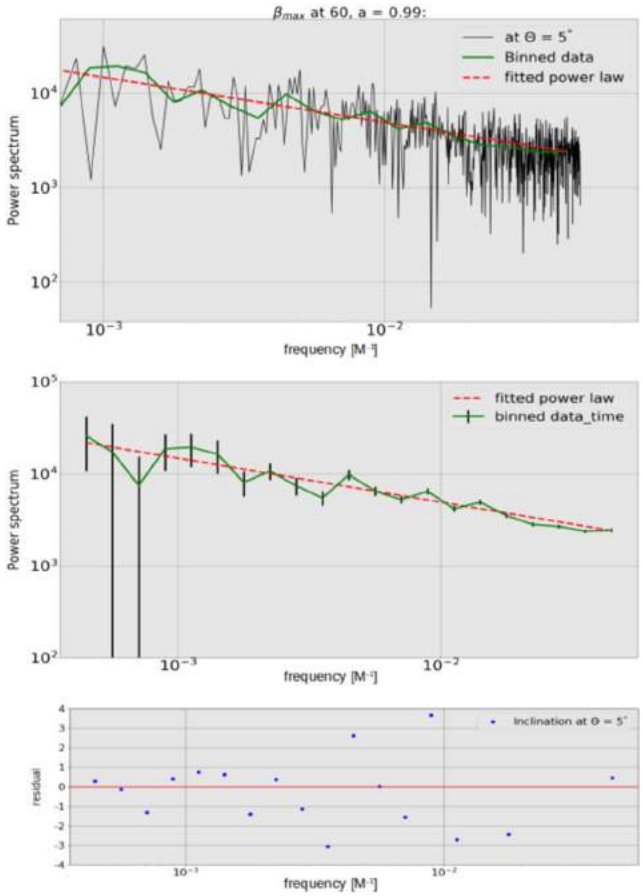

Figure 8. The top panel shows the simulated time series along with the binned data and the fitted PL. The middle panel shows the error bar in the binned data and the bottom panel is the residual plot for the binned data and fitted PL. The plots in this figure correspond to the model with $\beta_{\max} = 60$ and spin $a = 0.99$ at an inclination of $\theta = 5°$.

$a = 0.99$. The jet variability is extracted at an inclination angle of $\theta = 5°$. The plot shows binned data with a PL fitting. The error bars can be seen to be very large at low frequencies in the middle panel of Figure 8 as the data are largely spread around the mean value, but gradually they decrease, giving perfectly binned data. We further fit the binned data with a PL function of $-y(x) = Ax^{\alpha}$. The bottom panel of Figure 8 shows the residuals in the frequency function and it can be seen that the fitting is better in the low-frequency range. Out of our 18

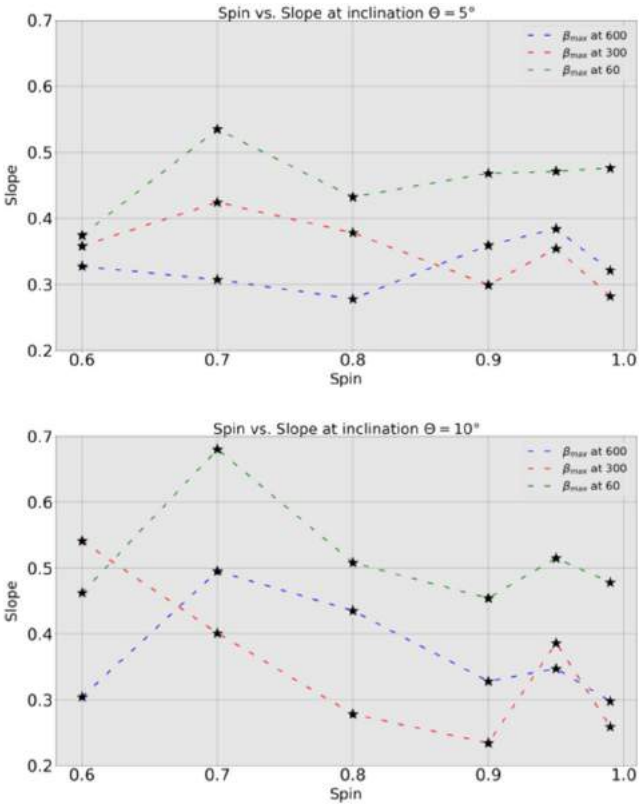

Figure 9. Relation between the black hole spin and the PL slope of the fitted PDS for all models, $\beta_{\max} = 600$ (blue lines), $\beta_{\max} = 300$ (red lines), and $\beta_{\max} = 60$ (green lines). The first panel is chosen at an inclination of 5° and the second one is at 10°.

models, we choose the PDS plot for this model (Figure 8) because its chi-square value is the lowest among all other models (reduced $\chi^2 = 14.21$). We note that in fact the PL model might not be the best way to reproduce the jet variability in this model. On the other hand, there are no significant peaks at specific frequencies, which would be found in the PDS analysis. Also, our aim is to show the general trends and correlations between the central engine properties and variability probes in the modeled jets. Therefore, we limit our study below to the relations between black hole spin and PDS slope.

4.2. Relation between the Central Engine and Jet Variability

In Figure 9 we show the relation between the slope of the PL function and the black hole spin in the jet engine. The time variability of jet energetics (the μ parameter) is measured at two different inclination angles, $\theta = 5°$ and $\theta = 10°$. We show three families of models here, with different magnetization of the torus. The values of the PL slope fitted for all models with different spins are listed in Table 3.

It can be inferred from our analysis that model with the lowest torus magnetization, i.e $\beta_{\max} = 600$, has the steepest PDS, and the highest slope of the PL function is found at spin $a = 0.7$. This is measured at both inclinations chosen for observing the jet variability. The model with the higher magnetization, $\beta_{\max} = 60$, is found to have steeper PDS slopes at a higher spin, $a = 0.95$, when measured at an inclination of $\theta = 5°$. As the inclination increases to $\theta = 10°$, the PDS is steeper at spin $a = 0.7$. For an intermediate model with

Table 3
Slopes of the Fitted PL for All Three Models $\beta_{\max} = 600$, $\beta_{\max} = 300$, and $\beta_{\max} = 60$

$\beta_{\max}$ in Torus	Spin a	Slope	
		Point 1, $\theta = 5°$	Point 2, $\theta = 10°$
$\beta_{\max} = 600$	0.99	0.321 ± 0.053	0.298 ± 0.052
	0.95	0.384 ± 0.068	0.347 ± 0.056
	0.90	0.359 ± 0.081	0.328 ± 0.053
	0.80	0.278 ± 0.066	0.435 ± 0.091
	0.70	0.308 ± 0.063	0.4495 ± 0.051
	0.60	0.327 ± 0.078	0.304 ± 0.052
$\beta_{\max} = 300$	0.99	0.282 ± 0.068	0.259 ± 0.038
	0.95	0.354 ± 0.067	0.386 ± 0.053
	0.90	0.298 ± 0.051	0.234 ± 0.071
	0.80	0.378 ± 0.063	0.278 ± 0.077
	0.70	0.423 ± 0.092	0.401 ± 0.064
	0.60	0.358 ± 0.063	0.542 ± 0.162
$\beta_{\max} = 60$	0.99	0.476 ± 0.073	0.478 ± 0.067
	0.95	0.471 ± 0.095	0.515 ± 0.047
	0.90	0.468 ± 0.101	0.454 ± 0.067
	0.80	0.432 ± 0.049	0.508 ± 0.049
	0.70	0.535 ± 0.074	0.680 ± 0.123
	0.60	0.374 ± 0.094	0.462 ± 0.121

$\beta_{\max} = 300$, the PDS is always steeper at lower spins, $a = 0.7$ and $a = 0.6$, for inclinations of $\theta = 5°$ and $\theta = 10°$, respectively.

We also investigated how the slopes of the PDS behave for different Lorentz factors of the jets in different models (see Figure 10). For particular magnetization values of $\beta_{\max}$, we do not see any particular pattern. The PDS are steep, with slopes $(\alpha) \geqslant 0.55$ for the model with lower magnetization, $\beta_{\max} = 600$, only (see Tables 1 and 3). Other models have quite flat PDS spectra, with slopes $(\alpha) \leqslant 0.55$. The model with $\beta_{\max} = 300$ presents the most varying relation between the slope versus Lorentz factor, as measured at inclination $\theta = 10°$.

On the other hand, a general anticorrelation between the jet Lorentz factor and PDS slope of the PL fit is seen when we abandon the dependence on the central engine magnetization. In other words, if the particular GRBs are treated individually, then most of them follow the trend of a decreasing PL slope with an increasing jet speed. The only outlier from this trend is the GRB which represents the model of most highly magnetized torus around the fastest spinning black hole. Here the jet is very strong, the Lorentz factor even reaches $\Gamma = 1000$ in some parts of the jet, while the slope of its variability PL function is again steeper.

5. Discussion and Conclusions

The variability of emission observed in the GRBs is a complex phenomenon. From the observational point of view, the detected gamma-ray flux exhibits a large variety of patterns that reflect complicated processes governing the high-energy radiation (Fishman et al. 1994). The flux varies on multiple timescales, and power spectral density of the light curves is frequently fitted with the PL function ($P(f) \sim f^{-\alpha}$). The values of the slope fitted to individual PDS spectra have a wide range. For the stochastic process driven by internal turbulence in the jet interior, a slope of $\alpha = 5/3$ is theoretically expected within the internal-shock scenario (Beloborodov et al. 2000). Also,

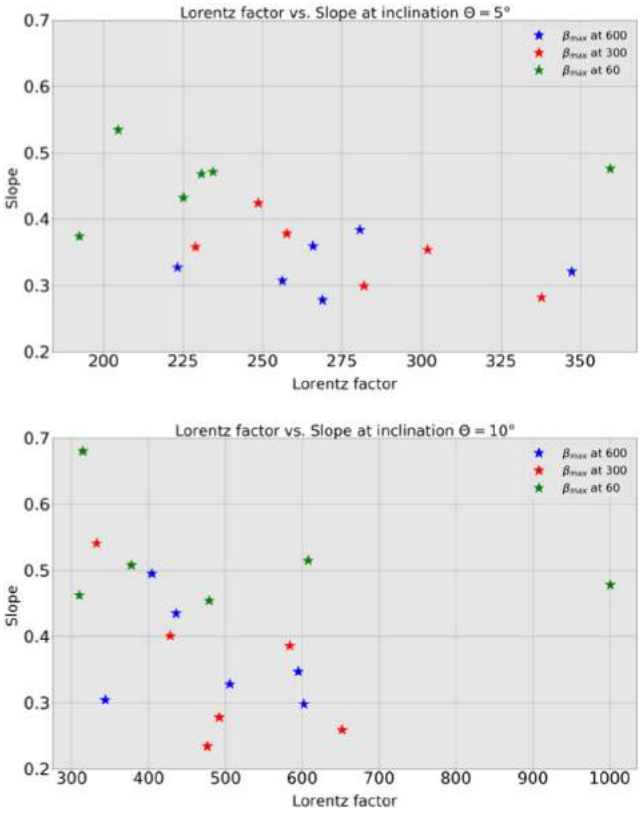

Figure 10. Relation between the Lorentz factor in the remote jet and the slope of the fitted PL for all models, $\beta_{\max} = 600$ (blue stars), $\beta_{\max} = 300$ (red stars), and $\beta_{\max} = 60$ (green stars). The first panel is for the observer's inclination of $\theta = 5°$ and the second one is at $\theta = 10°$.

Zhang & Zhang (2014) proposed a turbulence scenario with magnetic reconnections in the ejected shells to explain a PL PDS shape for the Swift GRBs.

In some GRBs the quasiperiodic oscillations have been tentatively detected with a periodicity between 2–8 s for long events and a few milliseconds for short events. These oscillations can be attributed to the nonsteady accretion in the central engine of a collapsing star (Masada et al. 2007) or to the modulation caused by the spin misalignment of a black hole after the merger with a neutron star (Stone et al. 2013).

Furthermore, several correlations between the variability properties and GRB energetics have been detected. The peak energy is anticorrelated with the PDS index (Dichiara et al. 2016). The general idea behind correlations of this kind invokes the jet Lorentz factor, Γ, being the main driver responsible for relations between both peak energy and luminosity, and GRB duration and its luminosity (Dainotti & Del Vecchio 2017). The duration of the burst, T_{90}, was also found to be related with the MTS. In the sample of long- and short-duration GRBs detected by Fermi, the statistical significance for the bimodal distribution of the events is higher when the MTS is taken into account (Tarnopolski 2015).

In our simulations, the variability in the jet is related to the action of the central engine and the timescale of the MRI. It can be seen that the duration of the pulses in the jet, which reveals the size and speed of blobs containing high thermal and Poynting energy, corresponds to the timescale of the fastest-growing mode of MRI (see Figure 4). Furthermore, we use the average duration of the pulses, measured at their half width, as

a proxy for the MTS. There is an anticorrelation found between this MTS proxy and the black hole spin parameter of the central engine. The latter is directly responsible for the jets launching via the Blandford–Znajek process, so that the jet Lorentz factor will increase with the black hole's spin, while the MTS decreases with it. Thus, the observed anticorrelation between the MTS and Γ is reproduced by our model (see Wu et al. 2016).

In addition, the MTS–T_{90} correlation should be naturally reproduced. However, this is mainly due to the fact that the calculations are done in a dimensionless unit system. Therefore, the simulations we run in dimensionless time units, $t_g = GM_{\rm BH}/c^3$, should be converted to physical timescales, assuming a fixed black hole mass. The time unit for a black hole of $10M_\odot$ will be equal to 4.96×10^{-5} s. The MTSs for this conversion unit are between 1–2 ms, while the timescale of operation of the engine, which we cover in our simulation, is of the order of 0.15 s (it has to be noted that we are not running the models for a longer time because of magnetic field decay and inefficient MRI turbulence at late times, which limits the effective accretion period, while the massive torus is still present and does not replenish, so the engine operation could last $\sim$100 times longer). Therefore, adopting a range of black hole masses driving the central engine of a GRB, from $\sim$3 to $\sim 30M_\odot$, we will automatically be able to cover the range of T_{90} duration times and MTSs in a correlated way. The scatter in this relation will be imposed by the additional factors, such as the mass of the disk available for accretion and its magnetization, hence the accretion rate. Furthermore, we can speculate that the relation between Γ and MTS, which spans $\sim$10 orders of magnitude in the observations presented by Wu et al. (2016), can also reach the blazar sample. The black hole mass in our simulations scales the MTS via the gravitational timescale, up to $\log(T) \sim 5$ for a black hole mass of $10^8 M_\odot$. The smaller values of Lorentz factor should be related mainly with a smaller black hole spin parameter.

We notice that our MTS (measured on average within the jet) is affected by the magnetic field strength, but assuming a given black hole spin we can have either the shortest timescales for the most-magnetized tori (i.e., $a = 0.99$, see Figure 6), or the opposite ($a = 0.7$–0.8). Therefore, we conclude that it is the total efficiency of the Blandford–Znajek process, rather than single parameter of the engine, which drives the jet variability timescales. Its observed value is further regulated by the factors describing the conversion efficiency of the jet bulk kinetic energy into radiation (Granot et al. 2015), which is beyond the scope of our present simulations.

We thank Kostas Sapountzis and Mariusz Tarnopolski for helpful discussions. We also thank the anonymous referee for many valuable suggestions that greatly improved our manuscript. We acknowledge support from the grants 2016/23/B/ST9/03114 and 2019/35/B/ST9/04000 from the Polish National Science Center, and acknowledge computational resources of the Warsaw ICM through grant g85-947, and the PL-Grid through the grant grb4.

ORCID iDs

Agnieszka Janiuk https://orcid.org/0000-0002-1622-3036

References

Begelman, M. C., Fabian, A. C., & Rees, M. J. 2008, MNRAS, 384, L19
Beloborodov, A. M., Stern, B. E., & Svensson, R. 2000, ApJ, 535, 158
Britzen, S., Fendt, C., Böttcher, M., et al. 2019, A&A, 630, A103
Bromberg, O., & Tchekhovskoy, A. 2016, MNRAS, 456, 1739
Cao, X., Liang, E.-W., & Yuan, Y.-F. 2014, ApJ, 789, 129
Chakrabarti, S. K. 1985, ApJ, 288, 1
Dainotti, M. G., & Del Vecchio, R. 2017, NewAR, 77, 23
Dichiara, S., Guidorzi, C., Amati, L., Frontera, F., & Margutti, R. 2016, A&A, 589, A97
Fernández, R., & Metzger, B. D. 2013, MNRAS, 435, 502
Fernández, R., Tchekhovskoy, A., Quataert, E., Foucart, F., & Kasen, D. 2019, MNRAS, 482, 3373
Fishman, G. J., Meegan, C. A., Wilson, R. B., et al. 1994, ApJS, 92, 229
Fragile, P. C. 2008, in Proc. of Science 062, VII Microquasar Workshop: Microquasars and Beyond (Trieste: SISSA), 039
Gammie, C. F. 2004, ApJ, 614, 309
Gammie, C. F., McKinney, J. C., & Tóth, G. 2003, ApJ, 589, 444
Granot, J., Piran, T., Bromberg, O., Racusin, J. L., & Daigne, F. 2015, SSRv, 191, 471
Janiuk, A., Mioduszewski, P., & Moscibrodzka, M. 2013, ApJ, 776, 105
Janiuk, A., & Yuan, Y. F. 2010, A&A, 509, A55
Kathirgamaraju, A., Tchekhovskoy, A., Giannios, D., & Barniol Duran, R. 2019, MNRAS, 484, L98
Kobayashi, S., Piran, T., & Sari, R. 1997, ApJ, 490, 92
Liska, M., Tchekhovskoy, A., & Quataert, E. 2020, MNRAS, 494, 3656
Lloyd-Ronning, N., Lei, W.-h., & Xie, W. 2018, MNRAS, 478, 3525
Masada, Y., Kawanaka, N., Sano, T., & Shibata, K. 2007, ApJ, 663, 437
McKinney, J. C., Tchekhovskoy, A., & Blandford, R. D. 2012, MNRAS, 423, 3083
Nathanail, A., Gill, R., Porth, O., Fromm, C. M., & Rezzolla, L. 2021, MNRAS, 502, 1843
Penna, R. F., Narayan, R., & Sądowski, A. e. 2013, MNRAS, 436, 3741
Porth, O., Chatterjee, K., Narayan, R., et al. 2019, ApJS, 243, 26
Qian, Q., Fendt, C., Noble, S., & Bugli, M. 2017, ApJ, 834, 29
Sapountzis, K., & Janiuk, A. 2019, ApJ, 873, 12
Siegel, D. M., & Metzger, B. D. 2018, ApJ, 858, 52
Sądowski, A., Narayan, R., Tchekhovskoy, A., et al. 2015, MNRAS, 447, 49
Stone, N., Loeb, A., & Berger, E. 2013, PhRvD, 87, 084053
Tarnopolski, M. 2015, MNRAS, 454, 1132
Tchekhovskoy, A., Metzger, B. D., Giannios, D., & Kelley, L. Z. 2014, MNRAS, 437, 2744
Tchekhovskoy, A., Narayan, R., & McKinney, J. C. 2011, MNRAS, 418, L79
Urrutia, G., De Colle, F., Murguia-Berthier, A., & Ramirez-Ruiz, E. 2021, MNRAS, 503, 4363
Vlahakis, N., & Königl, A. 2003, ApJ, 596, 1080
Wu, Q., Zhang, B., Lei, W.-H., et al. 2016, MNRAS, 455, L1
Zhang, B., & Zhang, B. 2014, ApJ, 782, 92

Chapter 4

Structure and variability studies of gamma-ray burst jets with magnetically arrested disks

This chapter presents a published article investigating the properties of gamma-ray burst jets considering magnetically arrested disks (Narayan, Igumenshchev, and Abramowicz, 2003; Tchekhovskoy, Narayan, and McKinney, 2011) as their central engines. It is based on the work done by me in the second and third years of my doctoral studies.

In this project, we extended the work done in our previous project to fully non-axisymmetric 3D simulations of gamma-ray burst central engines. Many observational studies suggest the existence of structured jets in gamma-ray bursts and such configurations are often taken into consideration to explain their complex variability in time (e.g. Margutti et al., 2018; Kathirgamaraju, Barniol Duran, and Giannios, 2018). It is also widely accepted that the emission we observe from both the classes of gamma-ray bursts results from an accretion disk around a central compact object, which forms during the initial phases of the event (Gehrels, Ramirez-Ruiz, and Fox, 2009). Also, magnetically arrested accretion disks are nowadays considered to explain properties of accreting compact sources, more widely in the context of AGNs (e.g. Chael, Narayan, and Johnson, 2019; Dexter et al., 2020; Event Horizon Telescope Collaboration et al., 2021). In this work, we consider the magnetically arrested accretion disks for the central engines of gamma-ray bursts and investigate how successfully they can explain the observed jet emission properties.

This project was done in collaboration with my supervisor Prof. Agnieszka Janiuk and Dr. Fatemeh Hossein Nouri, who is currently a postdoc in my group. I performed all the simulations and the data analysis presented in this work, with guidance from my supervisor at various stages. My colleague also provided some helpful insights in the final stages of this work.

The Astrophysical Journal, 935:176 (14pp), 2022 August 20 https://doi.org/10.3847/1538-4357/ac81b7

Modeling the Gamma-Ray Burst Jet Properties with 3D General Relativistic Simulations of Magnetically Arrested Accretion Flows

Bestin James, Agnieszka Janiuk, and Fatemeh Hossein Nouri
Center for Theoretical Physics, Polish Academy of Sciences, Al. Lotników 32/46, 02-668 Warsaw, Poland; bestin@cft.edu.pl
Received 2022 April 1; revised 2022 July 6; accepted 2022 July 16; published 2022 August 24

Abstract

We investigate the dependence of the gamma-ray burst (GRB) jet structure and its evolution on the properties of the accreting torus in the central engine. Our models numerically evolve the accretion disk around a Kerr black hole using three-dimensional general relativistic magnetohydrodynamic simulations. We use two different analytical hydrodynamical models of the accretion disk, based on the Fishbone–Moncrief and Chakrabarti solutions, as our initial states for the structure of the collapsar disk and the remnant after a binary neutron star (BNS) merger, respectively. We impose poloidal magnetic fields of two different geometries upon the initial stable solutions. We study the formation and evolution of the magnetically arrested disk state and its effect on the properties of the emitted jet. The jets produced in our models are structured and have a relatively hollow core and reach higher Lorentz factors at an angle $\gtrsim 9^\circ$ from the axis. The jet in our short GRB model has an opening angle of up to $\sim 25^\circ$ while our long GRB engine produces a narrower jet, of up to $\sim 11^\circ$. We also study the time variability of the jets and provide an estimate of the minimum variability timescale in our models. The application of our models to the GRB jets in the BNS postmerger system and to the ultrarelativistic jets launched from collapsing stars are briefly discussed.

Unified Astronomy Thesaurus concepts: Accretion (14); Gamma-ray bursts (629); Magnetohydrodynamics (1964); Jets (870); Relativistic jets (1390); Magnetohydrodynamical simulations (1966); Black hole physics (159); Stellar mass black holes (1611)

1. Introduction

Gamma-ray bursts (GRBs) are transient phenomena observed in the high-energy sky at cosmological distances. The emission of high-energy photons is released at the jet photosphere and presents nonthermal spectral distribution (Piran 2004). Their bimodal duration distribution suggests separate classes of progenitors being responsible for short and long events (Kouveliotou et al. 1993). The first class, long GRBs, were already identified with bright supernovae in the 1990s, e.g., for GRB 980425 (Galama et al. 1999). According to the collapsar model (Woosley 1993) a jet emerges after the collapse of a massive, rotating star and formation of a black hole in its core. The accompanying explosion gives supernova-like signatures in the emission spectra, up to several weeks after the GRB. Magnetohydrodynamic (MHD) simulations have been performed for such a model of GRBs as early as Proga et al. (2003) and found that MHD effects alone are able to launch, accelerate, and sustain strong polar outflows. The second class of bursts, whose duration is typically below a couple of seconds, originates from compact binary merger events. Here the central compact object remnant is surrounded by an accretion disk that is created from remnant matter of a tidally disrupted neutron star (Duez 2010). As a result, a Poynting-flux-dominated jet can be generated self-consistently as part of the MHD processes in the merger (Rezzolla et al. 2011; Ruiz et al. 2020). A confirmation of this type of progenitor came recently with the discovery of gravitational-wave event, GW170817, associated with a short GRB of duration 1.7 s in its prompt phase (Abbott et al. 2017). The accompanying observations showed clearly the multimessenger characteristics of this object (Margutti & Chornock 2021).

GRBs are seen as relativistic jets pointing toward our line of sight, when observed from Earth. Relativistic jets are ubiquitous phenomena in many accreting black hole sources. It is widely assumed that the properties of the accretion inflow affect the properties of the jet. The process which is responsible for driving accretion in magnetized disks is considered to be magnetorotational instability (MRI). as described by Balbus & Hawley (1991). The formation of a magnetically arrested disk (MAD) has been invoked recently to explain the properties of the jets observed (see Abramowicz 2013 and Bisnovatyi-Kogan 2019, for a review). In this scenario a large-scale bipolar field is accumulated around the central object due to the inward accretion of the plasma. Such a large-scale field is unable to dissipate locally by magnetic diffusivity, unlike a small-scale field, and cannot be absorbed if the central object is a black hole. The field thus accumulates in the innermost region of the accretion disk and results in the formation of a MAD (Narayan et al. 2003). The accumulation of magnetic flux which impedes with the accretion was noted even before in MHD simulations, which was later termed as the formation of a MAD (Igumenshchev et al. 2003; Proga & Begelman 2003). In this situation, the interchange instability comes into play subsiding the MRI which already should have developed initially due to the turbulence in the magnetized accretion flow (Proga & Zhang 2006). The accretion further proceeds in a MAD state mainly due to this interchange instability. The presence of large-scale bipolar fields in the accretion disks is often associated with the formation of astrophysical jets observed at various scales. Depending on the mass load, the magnetically driven jets can be classified into Poynting jets or

hydromagnetic jets. Poynting jets are naturally self-collimated and are powered either by the disks themselves or by the rotation of the black hole (Blandford & Znajek 1977; Li 2000). The existence of the MAD state can be linked to the production of powerful Poynting jets (Igumenshchev 2008). Tchekhovskoy et al. (2011) showed the formation of a relativistic jet from a MAD state and the extraction of the rotational energy of the black hole by the emitted jet according to the Blandford–Znajek mechanism. The other possible mechanism for jet launching in short GRBs is explained by neutrino-dominated accretion flows (NDAFs; Popham et al. 1999; Di Matteo et al. 2002; Janiuk et al. 2004; Liu et al. 2017). Since the post-merger disks are transparent for neutrinos, NDAFs are cooled continuously by neutrino emissions. This scenario proposes that some emitted neutrino energy can be transferred to a pair fireball through neutrino–antineutrino annihilations to generate collimated jets along the axis perpendicular to the disk plane (Paczynski 1991; Jaroszynski 1996; Richers et al. 2015; Just et al. 2016; Perego et al. 2017).

MAD models have been studied previously to explain the jet formation and time variability's dependencies on black hole's spin (Narayan et al. 2021), and the formation of the blazar gamma-ray flares in active galactic nuclei and supermassive black holes at galaxy centers such as M87 (Mizuta et al. 2018; Chael et al. 2019). Liska et al. (2020) investigated the effects of the initial magnetic field configuration and White et al. (2019) performed numerical convergence studies of MADs. Moreover, MADs were applied in the context of GRB observations explaining the variability of long GRB's luminosity during the prompt phase (Lloyd-Ronning et al. 2016), and constraining the magnetic field and black hole mass required to power Blandford–Znajek jets (Lloyd-Ronning et al. 2019).

In this article, we aim to explain the jet properties of long and short GRB engines considering a MAD as the central engine. We use the method of Janiuk et al. (2021) to determine the variability properties of these jets, now extending our previous work to the long-time, three-dimensional (3D) simulation of MADs. We investigate the properties of the relativistic jets produced by an accreting system around a Kerr black hole with two different hydrodynamical models of the accertion disk, using 3D general relativistic magnetohydrodynamic (GRMHD) simulations. We impose the initial magnetic field configurations such that the inner region of the disk builds up a substantial amount of poloidal flux in a short amount of time. Our intention was to achieve the MAD state rather quickly and to study the dependence of the jet properties on such a central engine configuration.

The article is organized in the following way. In Section 2 we present the numerical setup and initial configuration of our models. In Section 3 we describe the evolution of the disk, the formation of the MAD state, the properties of the resulting jet structure, and some analysis of our results. The astrophysical implications of our models, the application of our results to the short and long GRBs, and some further analysis are given in Section 4. Finally, we give a short summary and conclusions in Section 5.

2. Numerical Setup and Models

2.1. Code

We use our implementation of the GRMHD code HARM (Gammie et al. 2003; Noble et al. 2006; Sapountzis & Janiuk 2019) for evolving our models in a fixed Kerr metric. It is a conservative and shock-capturing scheme for evolving the equations of GRMHD. The code follows the flow evolution by numerically solving the continuity, energy-momentum conservation, and induction equations in the GRMHD scheme:

$$\nabla_\mu(\rho u^\mu) = 0, \tag{1}$$

$$\nabla_\mu(T^{\mu\nu}) = 0, \tag{2}$$

$$\nabla_\mu(u^\nu b^\mu - u^\mu b^\nu) = 0. \tag{3}$$

Here, u^μ is the four-velocity of the gas, u is the internal energy, ρ is the gas density, p is the gas pressure, and b^μ is the magnetic four vector. The stress–energy tensor is comprised of the gas and electromagnetic parts, $T^{\mu\nu} = T^{\mu\nu}_{\rm gas} + T^{\mu\nu}_{\rm EM}$, where

$$T^{\mu\nu}_{\rm gas} = \rho h u^\mu u^\nu + p g^{\mu\nu} = (\rho + u + p) u^\mu u^\nu + p g^{\mu\nu}, \tag{4}$$

$$T^{\mu\nu}_{\rm EM} = b^2 u^\mu u^\nu + \frac{1}{2} b^2 g^{\mu\nu} - b^\mu b^\nu,\ b^\mu = u^*_\nu F^{\mu\nu}. \tag{5}$$

Here, F is the Faraday tensor, and, in a force-free approximation, we have $E_\nu = u^\nu F^{\mu\nu} = 0$. We adopt dimensionless units in the code, with $G = c = M = 1$ for our simulations. Thus the length in the code units is given by $r_g = GM/c^2$ and the time is given by $t_g = GM/c^3$, where M is the mass of the black hole. As such, our models can represent the central engines of both the short and long GRBs.

The initial equilibrium torus state is prescribed in the Boyer–Lindquist coordinates (Boyer & Lindquist 1967) in the original solutions and they are transformed into Kerr–Schild (KS) coordinates in the code (see Weinberg 1972 and Visser 2007). The integration is done in the code in modified Kerr–Schild coordinates. So, in the code, the KS radius r has been replaced by a logarithmic radial coordinate $x^{[1]}$ such that $r = e^{x^{[1]}}$, the KS latitude θ has been replaced by $x^{[2]}$ such that $\theta = \pi x^{[2]} + \frac{(1-h)}{2}\sin(2\pi x^{[2]})$, and the azimuthal angle ϕ remains the same, $\phi = x^{[3]}$. Here the parameter h can be adjusted to concentrate the numerical resolution near to the midplane and we use a value of 0.5 for it in our models.

2.2. Models

The initial state of our models is assumed to be a pressure equilibrium torus, which is embedded in a poloidal magnetic field. The Kerr black hole will accrete matter onto it due to the development of MRI in the disk, and this will in turn affect the evolution of the magnetic field. Our models have a black hole spin characterized by the Kerr parameter $a = 0.9$; this is in the range of equilibrium spin values estimated by Gammie et al. (2004) for the models with stellar-mass black holes. The simulations are run with a resolution of $288 \times 256 \times 128$ in the r, θ, and ϕ directions, respectively. We use the γ-law equation of state, $p_g = (\gamma - 1)u$, in all our models, where p_g is the gas pressure, ρ is the gas density, and u is the internal energy. We use a value of $4/3$ for γ.

For our first model (FM76), the initial state of the accreting torus is prescribed according to Fishbone & Moncrief (1976, hereafter FM) who gave an analytic solution of a constant-angular-momentum steady state. We specify the initial size of the torus in geometrical units, where the inner edge, $r_{\rm in}$, is located at 6 r_g and the radius of pressure maximum, $r_{\rm max}$, is located at 13 r_g. This solution corresponds to a constant specific angular momentum $l = 7.414$ in the torus. For this model the outer edge of the disk is located around 60 r_g. We embed this initial torus configuration in a poloidal magnetic field, where the field lines follow the isocontours of density (see the top-left

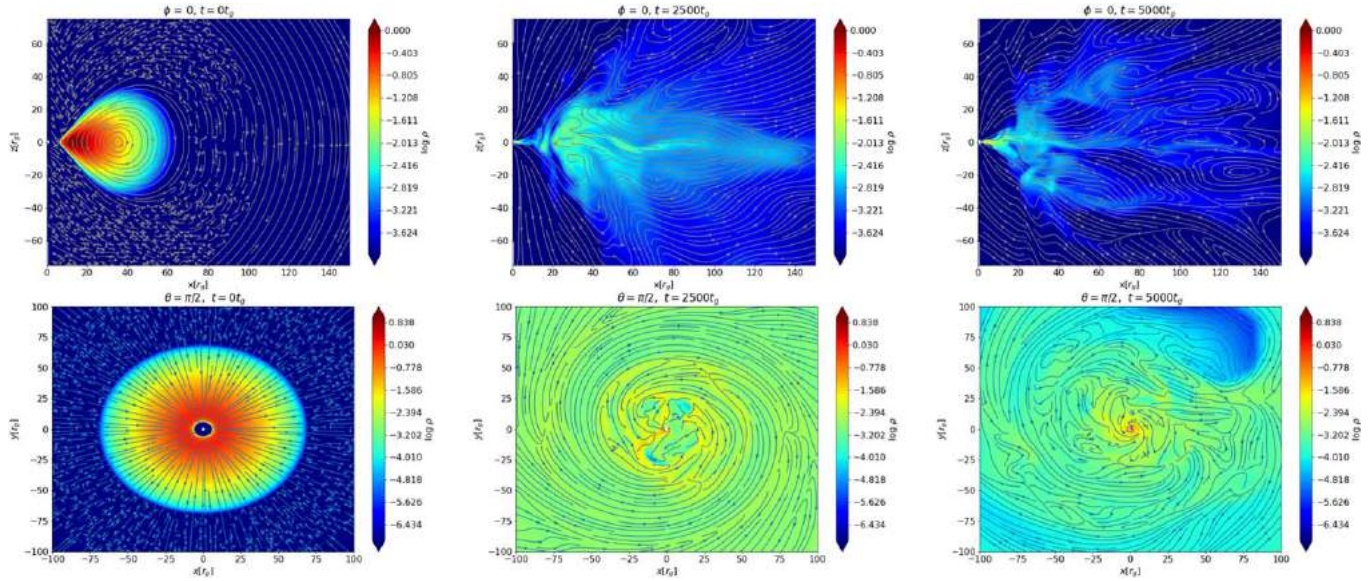

Figure 1. Snapshots of torus density structure along a poloidal plane ($\phi = 0$ slice) (top panel) and along the equatorial plane ($\theta = \pi/2$ slice) (bottom panel) with streamlines of magnetic field at $t = 0$ (left), 2500 (middle), and 5000 t_g (right), for the model with initial $\beta = 100$ and Fishbone–Moncrief configuration with Kerr parameter $a = 0.90$.

panel in Figure 1). For this field, the only nonzero component of the magnetic vector potential is given by

$$A_\phi(r, \theta) = r^5(\rho_{\rm avg}/\rho_{\rm max}) - 0.2, \tag{6}$$

which has a dependence on the disk density structure as well as a power of radius. Here, $\rho_{\rm max}$ is the initial density maximum inside the torus and $\rho_{\rm avg}$ is the average of the density value from the adjacent cells in the computational grid. We choose this field configuration with the intention of eventually bringing a large poloidal flux to the vicinity of the black hole. We use the initial gas to magnetic pressure ratio, $\beta = p_{\rm gas}/p_{\rm mag}$, to normalize the magnetic field in the torus. Here $p_{\rm gas} = (\gamma - 1)u_{\rm max}$ and $p_{\rm mag} = b^2_{\rm max}/2$, where $u_{\rm max}$ is the internal energy of the gas at the radius of maximum pressure. We normalize β to a value 100 at the radius of maximum gas pressure, $r_{\rm max}$, in the torus.

Our second hydrodynamical model (Ch85) of the accreting torus uses the Chakrabarti (1985) solution as the initial state. In this model the angular momentum has a power-law relation along the radius with the von Zeipel parameter $\lambda = (l/\Omega)^{1/2}$, where l denotes the specific angular momentum and Ω denotes the angular velocity. We adjust the size of the torus in geometrical units using the parameters $r_{\rm in(vonZeipel)}$, which is the true inner edge of the disk in this model, with a value of 6 r_g, and the radius of pressure maximum $r_{\rm max}$ with a value of 16.95 r_g. We use different values here from those of the FM model, due to the different hydrodynamical structure of the torus. The initial masses of the disks in both models are in the same range. The initial state of this model is shown in the left panel of Figure 2. In this model the outer edge of the torus is located around 80 r_g. In order to compare the size of the disk in both models, we calculate the total mass of the disk at the initial time. Using the appropriate density unit scaling, for the physical models we are considering, these values are estimated as 0.925 $M_\odot$ and 0.132 $M_\odot$, respectively, for the FM and Chakrabarti solutions. In our scenario, these models represent separately the long and short GRB central engines. In our second model, we embed the initial torus configuration in a poloidal magnetic field. Here, the field is given as the magnetic field produced by a circular current. The only nonvanishing component of the vector potential in such a configuration is given by (e.g., in Jackson 1998)

$$A_\phi(r, \theta) = A_0 \frac{(2 - k^2)K(k^2) - 2E(k^2)}{k\sqrt{4Rr\sin\theta}}$$
$$k = \sqrt{\frac{4Rr\sin\theta}{r^2 + R^2 + 2rR\sin\theta}}, \tag{7}$$

where E and K are the complete elliptic functions and A_0 is a quantity which can be used to scale the magnetic field. In our model the radius of the circular wire, R, is taken as the radius of pressure maximum $r_{\rm max}$ of the disk. We scale the magnetic field across the torus using the initial gas to magnetic pressure ratio, $\beta = p_{\rm gas}/p_{\rm mag}$. It has a maximum value of 480 inside the disk and has an average value of 100 within the disk. Therefore both our models are embedded in initial magnetic fields of comparable strength. A summary of the initial parameters used in our models is given in Table 1.

In order to break the axisymmetry, we introduce a 2% amplitude random perturbation (as similar to Mizuta et al. 2018) to the internal energy such that $u = u_0(0.98 + 0.1X)$, where u_0 is the equilibrium internal energy in our models and X is a random number in the range $0 \leqslant X \leqslant 1$. This perturbation breaks the initial axisymmetry of the system and helps in the development of nonaxisymmetric modes.

3. Results

3.1. Initial Configuration and Evolution of the Magnetized Tori

We start our simulations with a stable equilibrium analytic torus solution, as described in the previous section. The imposed magnetic field on the initial stable configuration causes turbulence inside the plasma and results in MRI. This acts as a mechanism which transports angular momentum outwards from the torus.

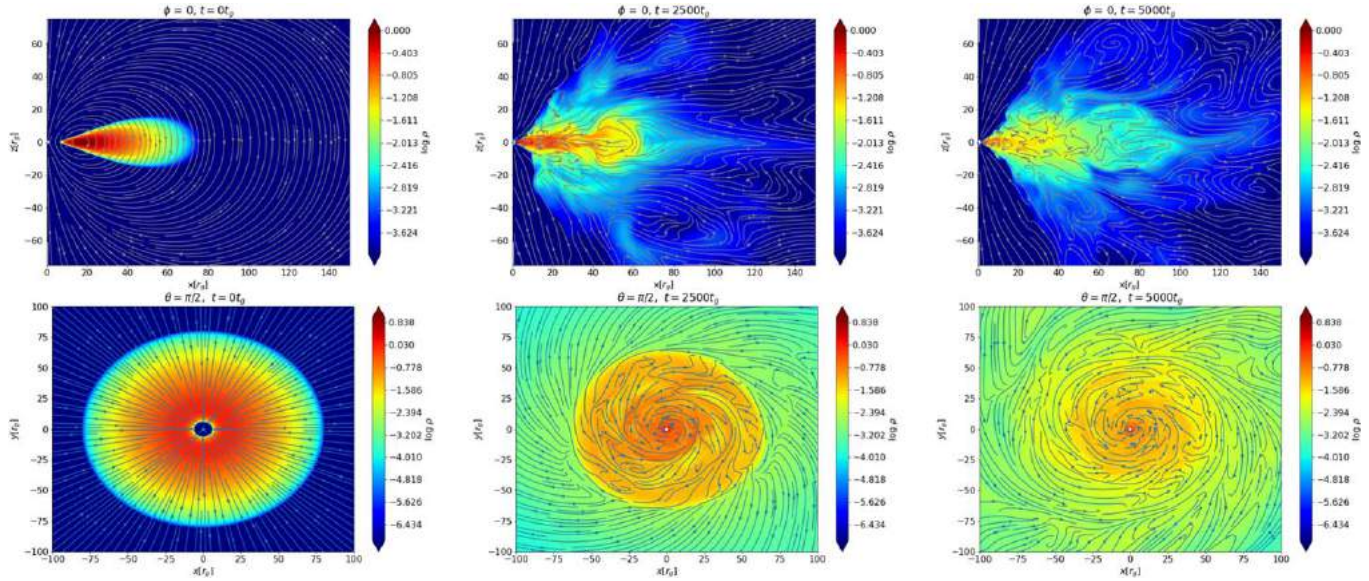

Figure 2. Snapshots of torus density structure along a poloidal plane ($\phi = 0$ slice) (top panel) and along the equatorial plane ($\theta = \pi/2$ slice) (bottom panel) with streamlines of magnetic field at $t = 0$ (left), 2500 (middle), and 5000 t_g (right), for the model with initial average $\beta = 100$ and Chakrabarti configuration with Kerr parameter $a = 0.90$.

Thus matter starts to accrete into the black hole. The geometry of the imposed magnetic field has some pronounced effect on the further evolution of the system. In our first model, the imposed field is based on the magnetic vector potential, which is dependent on the fifth power of the radius. So the poloidal field is smoothed out over a large distance and it takes a certain time for the plasma to bring the flux nearer to the black hole horizon. Such a configuration is plausible for collapsar central engines, where core collapse leads to magnetic flux compression (e.g., Burrows et al. 2007; see also Tchekhovskoy et al. 2011). On the other hand, in our second model the initial poloidal field is already strong near the horizon since it has the maximum value at the radius of pressure maximum ($r_{\rm max}$) of the disk. Such a configuration is adequate to describe the magnetic field in a post-merger remnant torus (see Paschalidis et al. 2013).

The evolved states of the flow after some time has elapsed, illustrated by the density structure, are shown in the middle and right panels of Figures 1 and 2, at times $t = 2500\ t_g$ and $t = 5000\ t_g$, respectively. The overplotted lines show the magnetic field. It can be noticed that the initial conditions have relaxed and the accretion has started due to the action of the magnetic field. We observe a couple of azimuthal modes of the Rayleigh–Taylor instability developing in the turbulent region of the inner disk. Hence, the accretion is steadily driven and proceeds despite the formation of a magnetic barrier. When we plot the streamlines of velocity similarly at the same time instances, the velocity field lines loosely follow the structure of the density distribution inside the disk, and along the equatorial region we can see the matter going in to the black hole. In the regions away from the disk, we observe outflows. In the poloidal slices for the evolved stages, we observe that the velocity streamlines always point outward near to the polar axis from the black hole, which shows the direction of the jet flows in the model.

In Figure 3 we show the evolution of the azimuthally averaged toroidal component of the magnetic field and its expansion with the polar angle (θ) over time. Initially, there is no magnetic field in the poles in either of the models, while the strong toroidal field is generated at the equatorial plane in the accreting torus due to its differential rotation. The field is transported to the black hole horizon with the MRI turbulence and is present there shortly after the beginning of the simulation. The average shown in the plots is taken at $\phi = (0,\ 2\pi)$ and at a radius of 10 r_g. With time, the toroidal field develops also at the polar regions, where it is being wound-up by the rotation of the black hole. It is also transported from the accretion disk toward the intermediate latitudes, via magnetic buoyancy, but in these regions the strength of the field is smaller than at the poles. In both our models we observe strips showing the periodic changes of the toroidal field component toward the polar regions. They seem to be anticorrelated with the pulses of the poloidal magnetic field, depicted in Figure 4, discussed below. In the second model, we notice also the field reversal in the regions near to the equator, which occurs predominantly at the initial period of the simulation ranging from time 1500 t_g to 6000 t_g. This is not noticed in our FM model evolution; however, Mizuta et al. (2018) noted field reversals also in their FM simulations, albeit with twice smaller resolution than in our models.

In Figure 4 we show the time evolution of the poloidal and toroidal components of the magnetic field in our models. The strength of the field components is calculated at the equator ($\theta = \pi/2$) by averaging it over the whole range of ϕ ($0 \leqslant \phi \leqslant 2\pi$) and also averaged for the radius in the range $r_{\rm hor} \leqslant r \leqslant 10\ r_g$, where the magnetic field is mostly concentrated. The plots show that the initially imposed poloidal field gets amplified with time due to the turbulence in the plasma in both the models. It can also be observed that the torodial component is initially zero but reaches a considerable strength (up to an order of $\sim 10^{-2}$ in code units) over time due to winding by the black hole rotation. The strength of the developed toroidal component remains higher in the disk than the poloidal counterpart for most of the simulation. The jet is launched thanks to the development of the toroidal magnetic field, which also helps in collimation of the jet base, in addition to the ram pressure acting at larger scales.

Table 1
Summary of Initial Parameters Used in Our Models

Model	Initial Magnetic Field Geometry	Kerr Parameter (a)	Inner Edge of the Disk $r_{\rm in}$ (in r_g)	Radius of Pressure Maximum $r_{\rm max}$ (in r_g)	Mass of the Disk in $M_\odot$	Initial β in the Disk
1. FM76	Poloidal field, following the disk density structure	0.90	6.0	13.0	0.925	100
2. Ch85	Poloidal field, due to a circular current at $r_{\rm max}$	0.90	6.0	16.95	0.132	100

In Figure 5 we show the mass accretion rate near the black hole horizon as a function of time for both our models. The accretion starts after a short amount of time due to the development of the magnetic turbulence. This brings in plasma to the black hole horizon along with the magnetic flux. The sudden increase in the accretion rate in the beginning of the simulation can be attributed to the development of magnetic turbulence, which begins to bring the matter in the disk to the horizon, and relaxation of the initial stationary conditions. But when a substantial amount of magnetic flux is built up near the horizon, the accretion significantly reduces shortly afterwards, which can be seen as the sudden drop in the accretion rate after around 1500 t_g. This trend is observed in both our models but is more pronounced in the second one due to the specific geometry of the initially applied field. This is connected to the formation of the MAD. Thus our second model reaches the magnetically arrested state much quicker than the first one. The mass accretion proceeds and sustains in time due to the plasma instabilities further developed in the disk.

3.2. Formation of the Magnetically Arrested Disk

In our simulations the accretion of matter onto the black hole is initiated due to MRI and proceeds further due to sustained turbulence in the plasma. Depending on the initial geometry and strength of the magnetic field, it is probable that the accreting material brings a substantial amount of poloidal flux to the vicinity of the black hole over time. In such cases, after a certain time, the strength of the magnetic field threading the black hole horizon increases considerably. A strong poloidal magnetic field developed in such a way will impede with the accretion and push away the plasma coming into the black hole. Thus the smooth flow of matter along the equatorial axis is halted and the further accretion proceeds mainly in short episodes due to the interchange instability developed in the plasma afterwards. Such a state of the accreting torus is often called the magnetically arrested disk (MAD) state. We observe the MAD state in both of our models with full 3D simulations. To parameterize the amount of magnetic flux on the black hole horizon as compared to the inward flow of matter, we calculate the normalized and averaged magnetic flux threading each hemisphere of the black hole horizon. It is computed as

$$\phi_{\rm BH}(t) = \frac{1}{2\sqrt{\dot{M}}} \int_\theta \int_\phi |B^r(r_H, t)| dA_{\theta\phi}. \quad (8)$$

The magnetic flux threading the black hole horizon, normalized to the mass flux, is shown in Figure 6 for both our models (in our code we use Gaussian units and so a factor of 4π is not included in this flux). It can be seen that our models have dynamically evolving magnetic fields in the inner disk region. In the model with the FM initial configuration, we notice from the plot that the magnetic flux builds up as the accretion proceeds, even though the initially applied field is not extremely strong, quantified by the plasma β value as high as 100 inside the disk. After around 1000 dynamical times, the normalized magnetic flux reaches the highest value of up to 50. The mass inflow is thus hindered due to the buildup of the field and the disk reaches a magnetically arrested state. The mass accretion rate considerably reduces from above 10 to the range of 10^{-1}–10^{-3} (in code units) after such a state is achieved (see Figure 5). This normalized magnetic flux on the horizon always remains 10 times or more larger than the mass flux as the model further evolves and the disk stays in a magnetically arrested configuration. In the model with the Chakrabarti initial state, we see such an effect more immediately after the accretion starts. The normalized magnetic flux threading the black hole horizon reaches a value of up to 120, as compared to the mass flux. This higher value as compared to the previous model can be attributed to the different initial magnetic field configuration we use in this model, even though the strengths are comparable. But here, also, the accretion proceeds due to the instabilities developed in the plasma later, especially due to the interchange instability. The magnetic flux normalized to the mass flux at the horizon remains higher than 20 in this model for most parts of the simulation and has a more dynamic nature. The time-averaged values of this magnetic flux at the horizon are 15.33 for the FM76 model and 25.49 for the Ch85 model, respectively.

3.3. Jet Power and Energetics

We use the jet energetics parameter μ to estimate the Lorentz factor at infinity (Γ), assuming all energy is transformed to the baryon bulk kinetic, as shown by Vlahakis & Königl (2003). It is defined as

$$\mu = -\frac{T_t^r}{\rho u^r}. \quad (9)$$

Here, T_t^r is the energy component of the energy-momentum tensor, which comprises matter and electromagnetic parts, ρ is the gas density, and u^r is the radial velocity. Thus it is the total plasma energy flux normalized to the mass flux. We also use the magnetization parameter, σ, to estimate the degree of magnetization in the jet funnel region:

$$\sigma = \frac{(T_{\rm EM})_t^r}{(T_{\rm gas})_t^r}. \quad (10)$$

In Figure 7, we plot the logarithmic contours of σ at time snapshots $t = 500\, t_g$ and $5000\, t_g$, that is, approximately at the jet launching phase and at an evolved time. The plots show that the jet funnel region is significantly magnetized already at the initial launch phase. In particular, in the Ch85 model, the maximum magnetization reaches $\log \sigma = 2.5$, at the base of the jet. This high magnetization persists at later times, and also

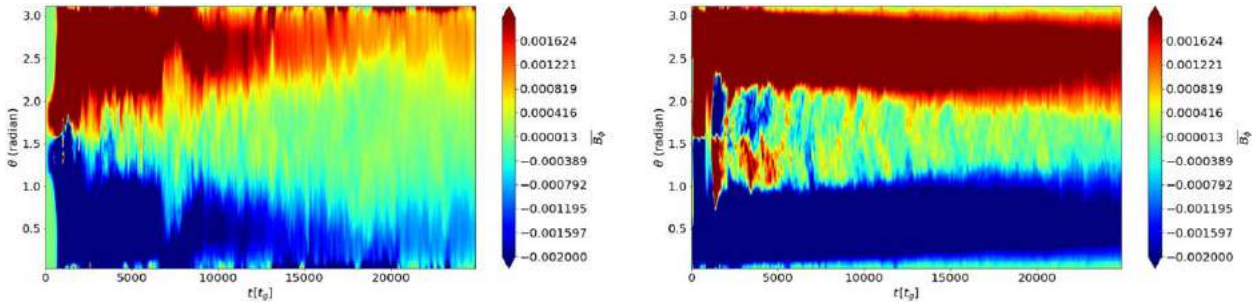

Figure 3. Butterfly diagram: showing the spatiotemporal evolution of the azimuthally averaged toroidal field $\bar{B}_\Phi\,(r = 10\ r_g, \theta, t)$ in our models with (a) FM initial disk and (b) Chakrabarti initial disk configuration.

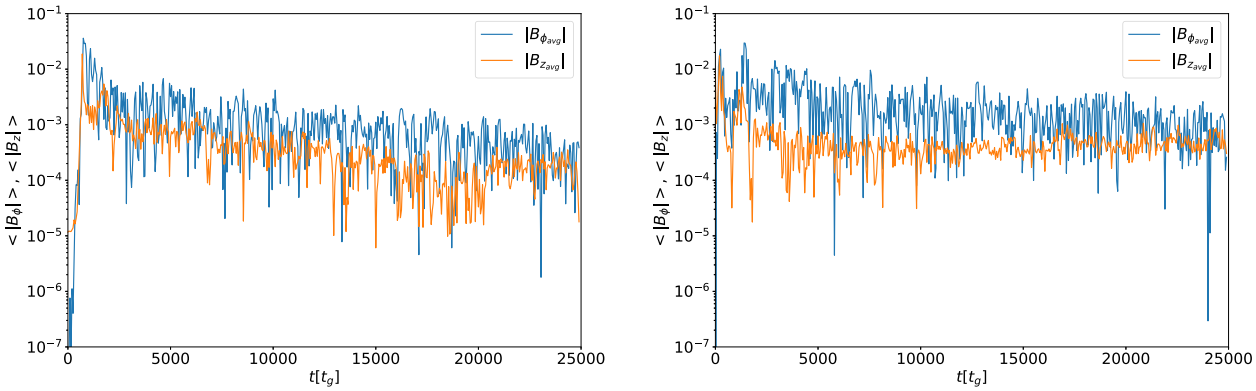

Figure 4. Strengths of the toroidal and poloidal components of the magnetic field at the equator ($\theta = \pi/2$) averaged over $r_{\rm hor} \leqslant r \leqslant 10 r_g$ and $0 \leqslant \phi \leqslant 2\pi$, with time (a) for model with initial Fishbone–Moncrief configuration (FM76), and (b) with initial Chakrabarti configuration (Ch85).

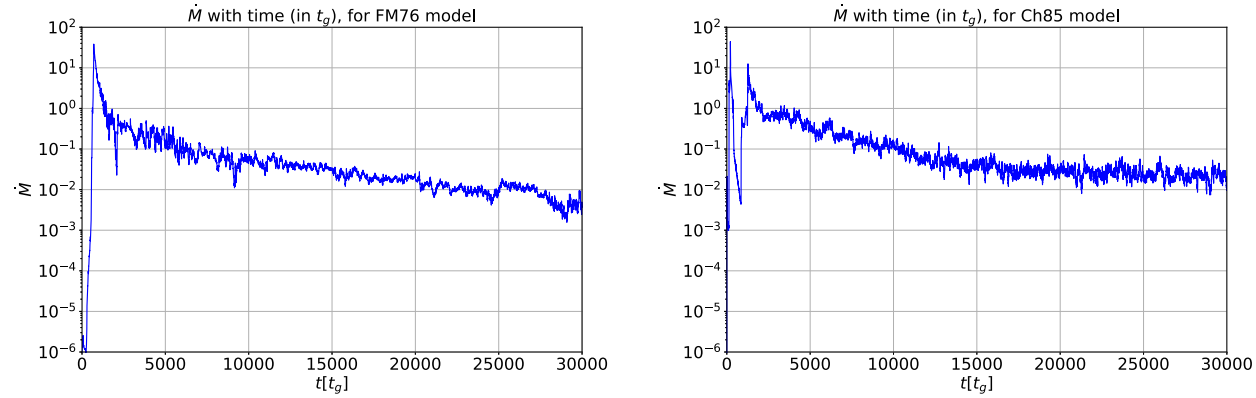

Figure 5. Mass accretion rate at the event horizon ($\approx$1.4 r_g) with time (in t_g) for (a) model with initial Fishbone–Moncrief configuration (FM76), and (b) with initial Chakrabarti configuration (Ch85).

develops eventually in the FM76 model, which was initially slightly less magnetized in the jet region.

Figure 8 shows the azimuthally averaged, angular profiles of the magnetization parameter, taken at different time instances of evolution. It can be seen that the initially negligible magnetization increases eventually toward the jet walls, and the launching phase starts in both models around 500–1000 t_g. The level of magnetization fluctuates slightly in the jet funnel region due to the episodic accretion events.

Figure 9 shows the structure of the jet by the distribution of the μ parameter at 5000 t_g for both models. We choose two locations along the jet direction and estimate the value of the jet energetic parameter μ at these locations. The chosen location 1 is at $r = 150\ r_g$, $\theta = 5°$, which is in the inner region of the jet close to the polar axis, while the location 2 is at $r = 150\ r_g$, $\theta = 10°$, which is toward the outer region of the jet. The values we get from these locations are averaged over the whole toroidal angle ϕ. We calculate the Lorentz factor of the observed jets from our models as the time average of μ (after the jet has launched) at these chosen locations. The Lorentz factor averaged from the two locations for the FM model is 97.71 and for the Chakrabarti model is 131.85. So both the jets are accelerated to high relativistic velocities. The higher Lorentz factor in the second model may be attributed to the

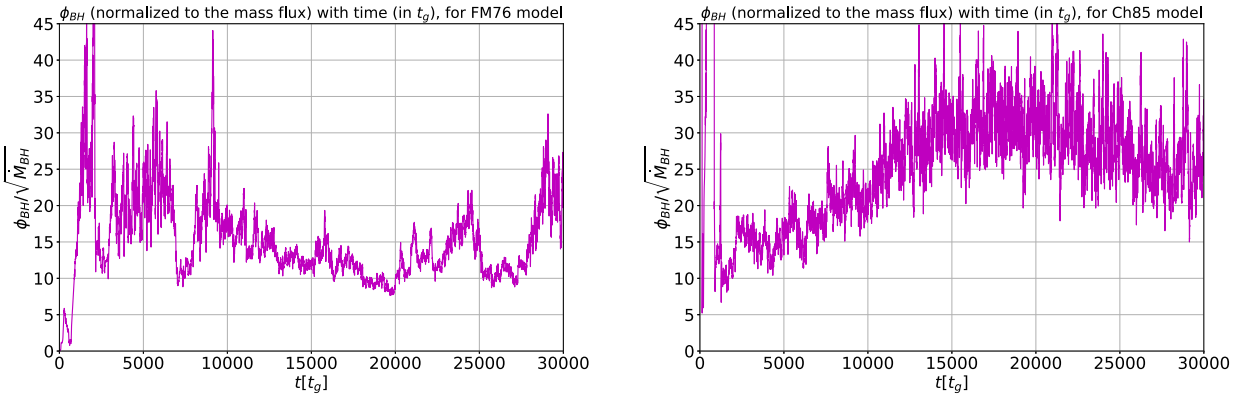

Figure 6. Time evolution of the magnetic flux on the black hole horizon normalized to the mass flux (a) with initial Fishbone–Moncrief configuration (FM76), and (b) with initial Chakrabarti configuration (Ch85).

different initial structure of the magnetic field, which extends beyond the disk.

The time variability of the jet referring to the jet energetic parameter μ is discussed in the next subsection.

In order to estimate the Blandford–Znajek luminosity of the emitted jet, we compute the radial energy flux by (see McKinney & Gammie 2004)

$$\dot{E} \equiv \int_0^{2\pi} \int_0^{\pi} d\theta d\phi \sqrt{-g} F_E, \tag{11}$$

where $F_E \equiv -T_t^r$. This can be further subdivided into matter, $F_E^{(\mathrm{MA})}$, and electromagnetic, $F_E^{(\mathrm{EM})}$, parts. The electromagnetic part only, which we consider in our computation above, is given by (see McKinney et al. 2012)

$$T^{(\mathrm{EM})\,\mu}_{\ \ \nu} = b^2 u^\mu u_\nu + p_b \delta^\mu_\nu - b^\mu b_\nu. \tag{12}$$

We show the evolution of the jet power with time estimated from the Blandford–Znajek luminosity in Figure 10. Notice that the plots are also marked with physical units assuming a central black hole mass of 3 $M_\odot$ for the short GRB central engine and a mass of 10 $M_\odot$ for the long GRB progenitor central engine (see Sharma et al. 2021 for an estimated range of black hole masses for observed GRB samples). It can be noted from the plots that the jet power rises after a certain amount of time after the simulations have begun; the jet formation time is actually coincident with the development of the toroidal magnetic field component in the disk, as described in Section 3.1.

3.3.1. Variability of the Jet and Accretion Rate

Figure 11 shows the variability of the jet energetics parameter with time as measured at the location 1, that is, at the inner region closer to the axis of the jet, for our two models. We calculate the average duration of the peak widths at their half maximum and use it as a proxy for the minimum variability timescale (MTS) of the jet. The MTSs computed from the above chosen locations and their averages are given in Table 2. The variability timescale has a smaller value in the inner region of the jet for both the models and thus the peaks have shorter duration at smaller angles from the rotation axis of the black hole. To better understand the time variability of the jet emission we also computed the power density spectra (PDS) of the μ variability data from these chosen locations. We fit this data to a power-law (PL) function of the form $y(x) = Ax^\alpha$ and calculate its slope. Figure 12 shows the PDS and the power-law fit for the μ data from both the locations for our models. The slopes of the fitted power-law curves are also given in Table 2.

3.3.2. Jet Profile

Figure 9 shows the 3D distribution of the jet energetics parameter μ for both of our models up to a radius of 200 r_g at a dynamical time 5000 t_g. These plots represent the evolved structure of the jet after a certain time after the jet has launched. Both of our models clearly produce structured jets rather than a simple top hat, similar to what we have seen in our previous study with two-dimensional (2D) simulations. However, our current models evolve the nonaxisymmetric structure of the jet. Larger values of Lorentz factor are obtained farther from the axis, as can be seen from the plots. So, the jets produced by our models have a comparatively hollow core, with small Lorentz factors ($\sim$10) up to an angle of $\sim$5°. Higher Lorentz factors are reached far from the axis of the jet and the jet is faster along the edges. This is similar to those observed in previous simulations of MHD jets, as described in Nathanail et al. (2020). Further description of the jet structure is provided in the next section where we discuss it in the context of short GRBs.

In order to qualitatively understand the energy distribution in the jet, we calculated the jet Lorentz factor as a function of the polar angle at a very large distance from the center. Figure 13 shows the time-averaged jet Lorentz factor estimated at a large distance (2000 r_g) as a function of the polar angle for both the models. For the FM model, the most energetic parts of the jet are confined mostly within an angle of $\sim$11°–12° and the highest Lorentz factors are reached around 9° from the axis. We discuss this model in the context of long GRBs. On the other hand, the model with Chakrabarti initial configuration, which we consider as the central engine for short GRBs, has a somewhat different jet profile. In this model, the jet does not clearly confine to an angle of $\lesssim$15° but instead spreads up to 25°. It is worth noting that the inner part near to the axis of rotation is much less energetic in this model. The outer regions of the jet, which are away from the rotational axis of the black hole, are also more structured in this model. The values of the Lorentz factor along different ϕ slices vary significantly between each other.

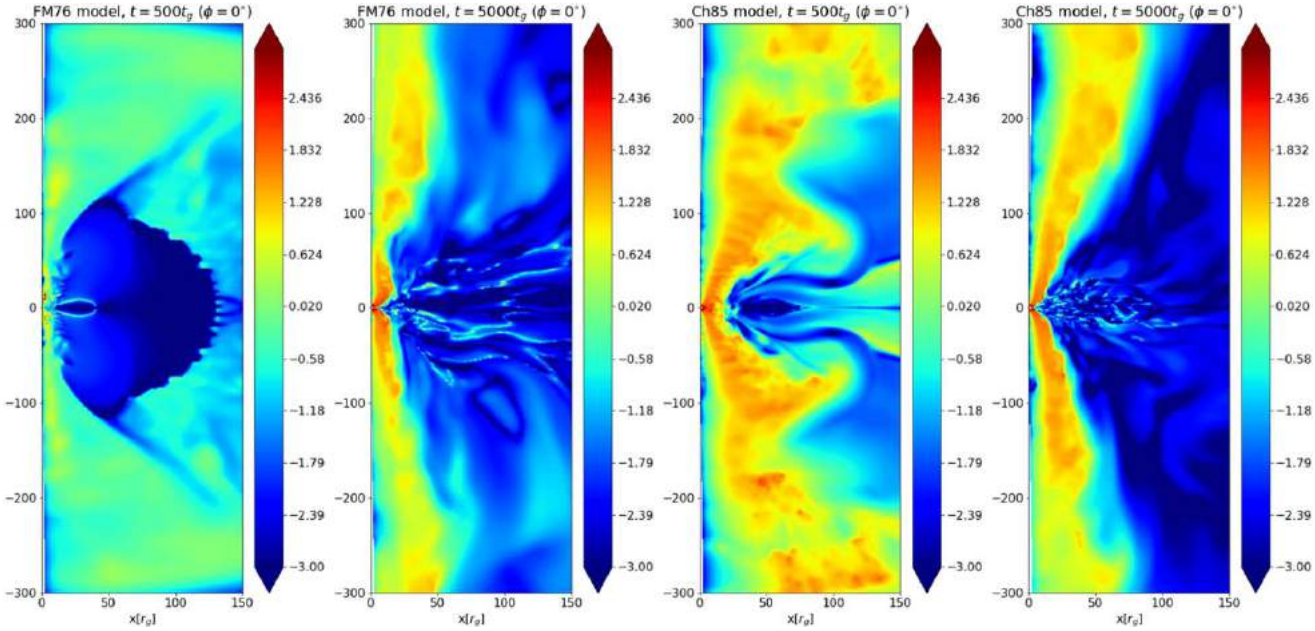

Figure 7. Two-dimensional contours of jet magnetization parameter σ in log scale (see Equation (10)) for (a) FM76 and (b) Ch85 models at time $t = 500\,t_g$ (at the very beginning of the jet launching) and $t = 5000\,t_g$ (at an evolved time), respectively. The plots show that the jet funnel region is magnetized from the initial times of jet launching.

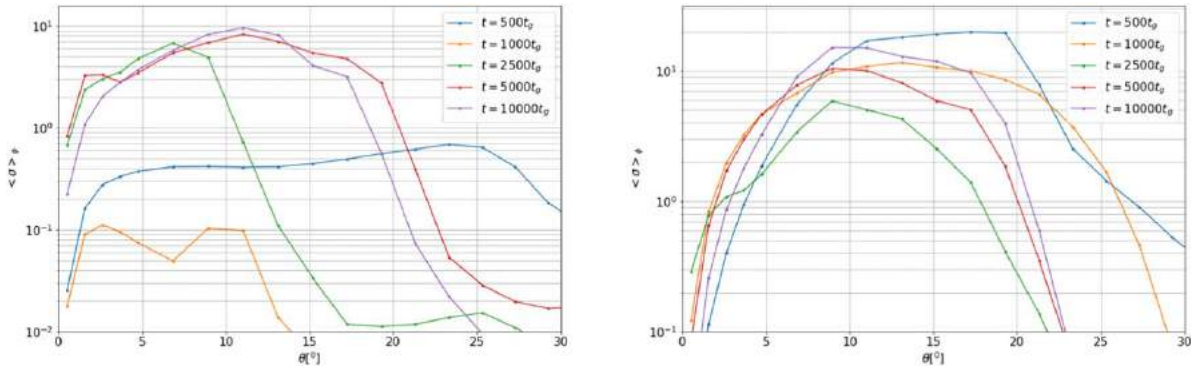

Figure 8. The profile of jet magnetization parameter σ (see Equation (10)) for (a) FM76 model and (b) Ch85 model, computed at $r = 150\,r_g$, with the polar angle θ at different time instances. The plots show that the magnetization is negligible along the polar axis at the initial time but increases fast in the jet funnel region as the jet launches. This shows that the jet is magnetized from the launching phase.

3.4. Effect of the Resolution and the Initial Magnetic Field Geometry in Achieving the Magnetically Arrested Disk State

The resolution study of White et al. (2019) was particularly focused on the MAD scenario. They found that certain global properties converge with resolution such as the mass accretion rate, jet efficiency, and the MRI suppression factor. We note that our global resolution of $288 \times 256 \times 128$ is at least at the level of their level 2 resolution, which satisfactorily resolves these quantities.

The wavelength of the fastest growing mode of the MRI is given by (Siegel & Metzger 2018):

$$\lambda_{\rm MRI} = \frac{2\pi}{\Omega}\frac{b}{\sqrt{4\pi\rho h + b^2}}. \tag{13}$$

Initially, accretion is initiated and driven by MRI, as described previously. The MRI is then suppressed in our models at an evolved time by the fact that a very strong magnetic barrier is formed near the black hole horizon. This halts the MRI-driven accretion, and interchange instabilities drive the process, resulting in the formation of a MAD state. The suppression of MRI can be quantified by the parameter $S_{\rm MRI}$, which is the ratio of the MRI's fastest growing mode wavelength over the disk scale height (see White et al. 2019 and McKinney et al. 2012):

$$S_{\rm MRI} = \frac{2H}{\lambda_{\rm MRI}}, \tag{14}$$

where $H = c_s/\Omega_K$ with the sound speed $c_s = \sqrt{\gamma p_g/(\rho_0 + u_g + p_g)}$ and Ω_K is the Keplerian angular velocity. Figure 14 shows a comparison of the disk scale height and the MRI wavelength in our models at an evolved time $t = 5000\,t_g$. We can see that the MRI wavelength is much larger in comparison to the disk scale height in both cases, indicating that $S_{\rm MRI} < 1$ and the suppression of the MRI.

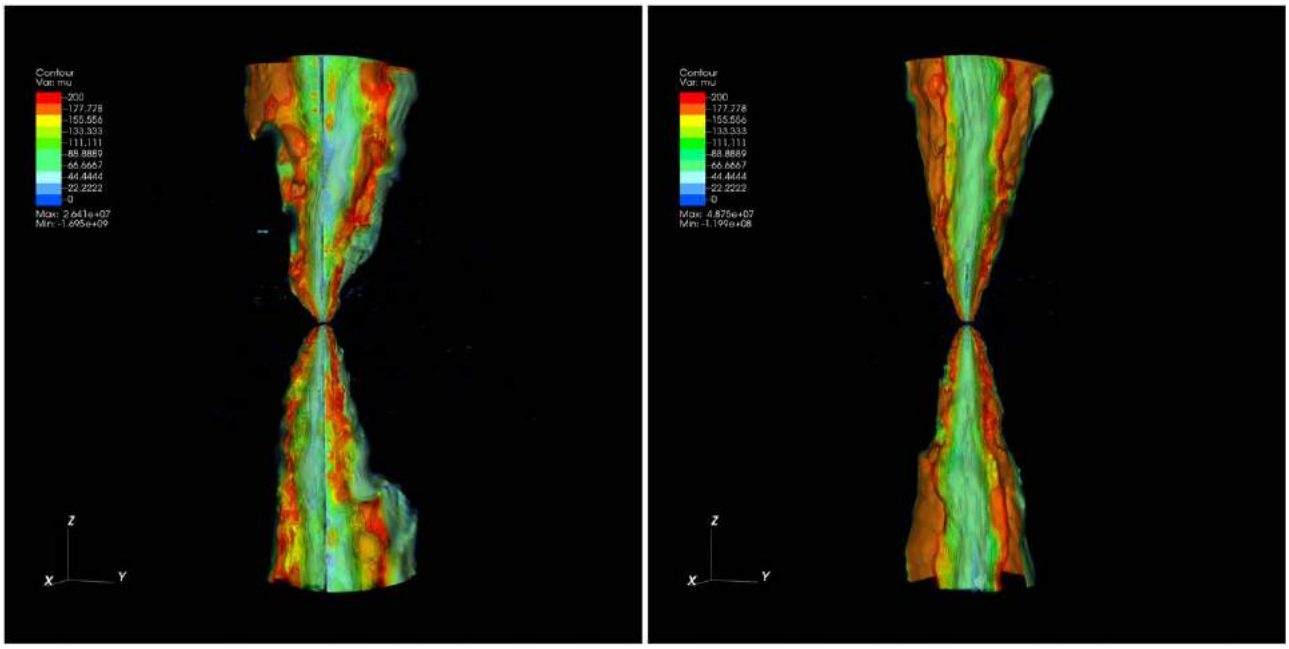

Figure 9. 3D jet structure at time $t = 5000\ t_g$ for (a) Fishbone–Moncrief (FM76) model (left panel), and (b) Chakrabarti (Ch85) model (right panel). The plots show the contours of the energetics parameter defined as μ (see Equation (9)) up to a radius of 200 r_g in both directions. The plots are clipped along the Y–Z plane to show the inner structure of the jet.

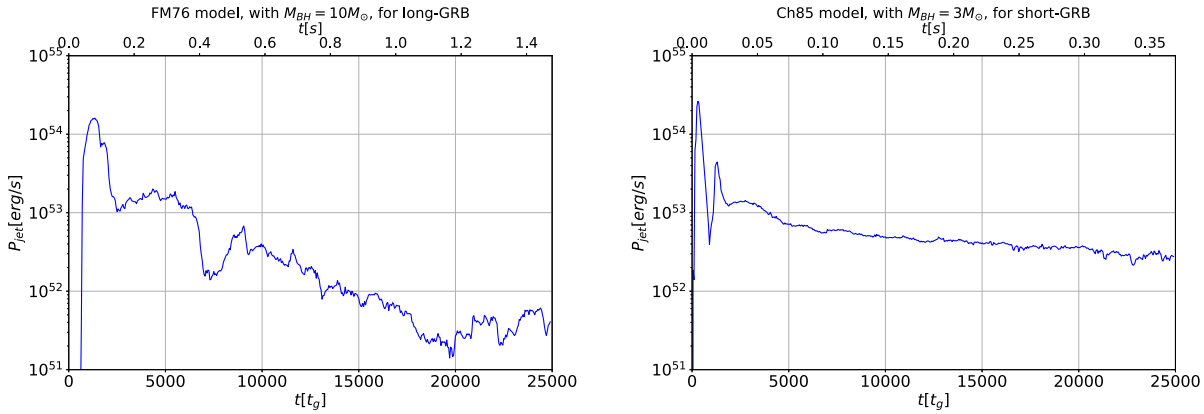

Figure 10. Jet power estimated by the Blandford–Znajek luminosity (see Equation (11)) in physical units (erg s^{-1}) as a function of time (in t_g). We also show the physical timescales scaled with the assumed black hole masses of long and short GRBs: (a) with initial Fishbone–Moncrief configuration (FM76), and (b) with initial Chakrabarti configuration (Ch85).

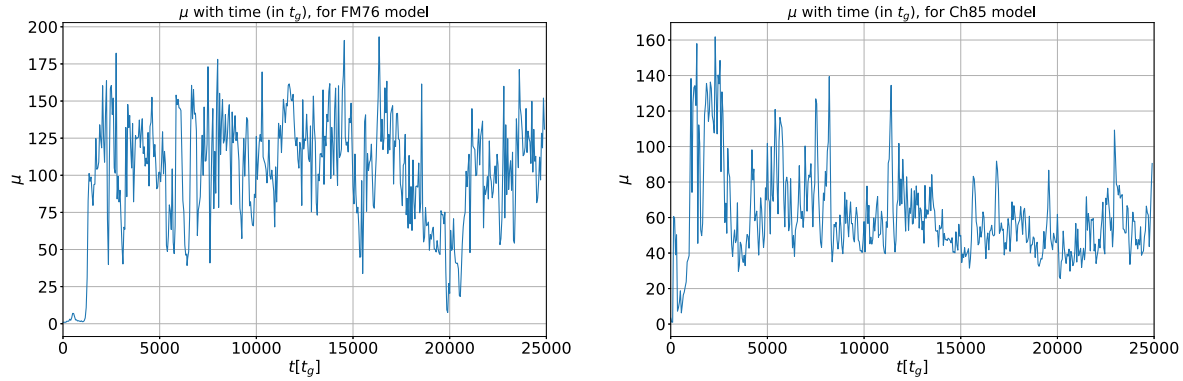

Figure 11. The time evolution of the jet energetics parameter μ at a chosen location $r = 150\ r_g$ and $\theta = 5°$ (location 1), averaged over the toroidal angle ϕ for the models (a) with initial Fishbone–Moncrief configuration (FM76) and (b) with initial Chakrabarti configuration (Ch85).

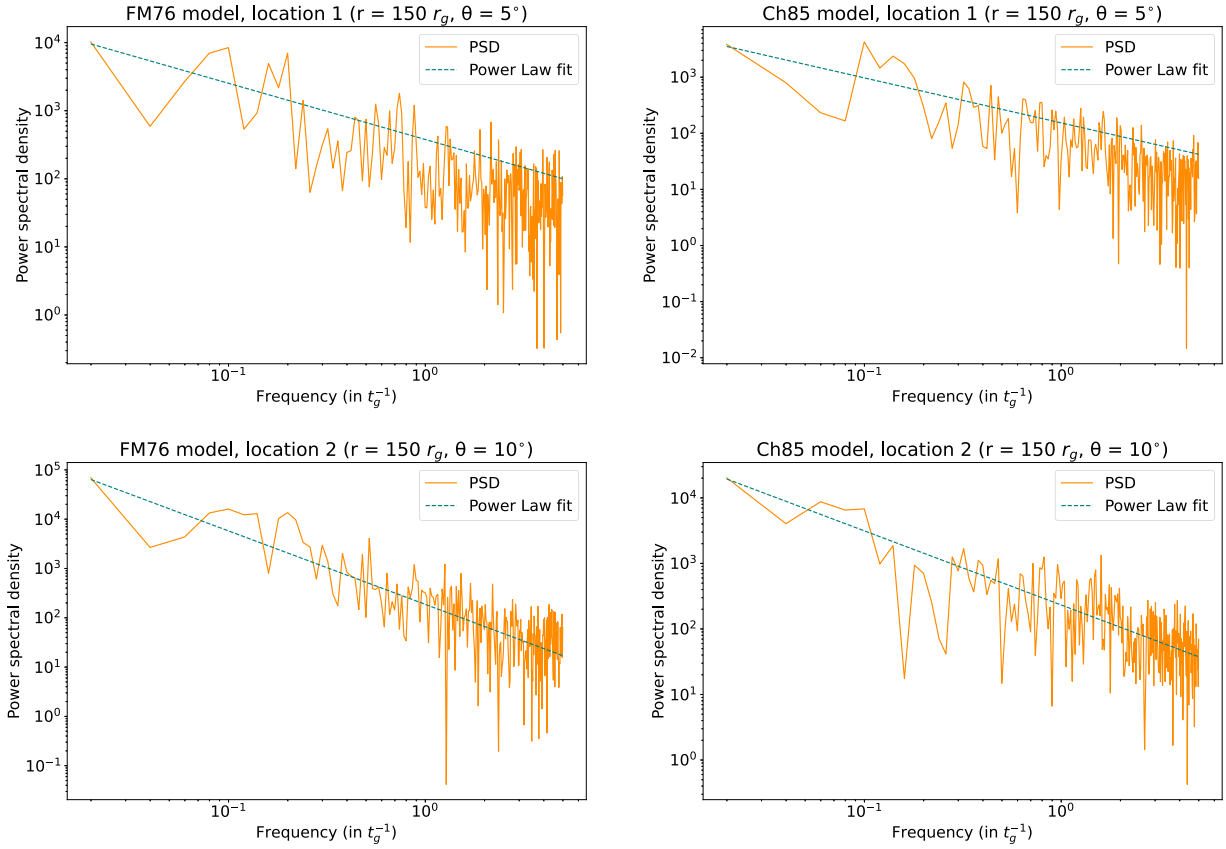

Figure 12. The power spectral density computed from the μ time variability data at the chosen locations 1 and 2 and the corresponding power-law fit for the models (a) with initial Fishbone–Moncrief configuration (FM76), and (b) with initial Chakrabarti configuration (Ch85).

Table 2
The Values of Γ, MTS (in t_g), and the Slopes of the Power-law Fit to the PDS, at the Two Chosen Locations inside the Jet for Our Models

Model	Lorentz Factor (Γ)			MTS Estimated (in t_g)			Slope of the PDS	
	Location 1	Location 2	Average	Location 1	Location 2	Average	Location 1	Location 2
FM76	105.96	89.45	97.71	178.63	269.80	224.21	−0.8253	−1.4899
Ch85	61.33	202.36	131.85	147.01	147.72	147.37	−0.8016	−1.1310

Following White et al. (2019), we assume that the accumulated flux on the horizon, $\phi_{\rm BH}$, is not affected by the resolution. Thus we argue that the large-scale structures of the MAD flows are correctly described by our models. Our models have sufficiently enough resolution to properly catch the base of the jet structure and Lorentz factor profiles as well.

We initialize our models with single large poloidal loops of magnetic field. Such configurations are proved to result in the development of strong poloidal flux in the vicinity of the black hole horizon as the accretion proceeds (McKinney et al. 2012; Penna et al. 2013). This helps in achieving the MAD state within a short time (∼1500–2000 t_g) after the simulation has begun (as can be seen from Figure 6). We note that some recent simulations have shown that the development of such strong poloidal flux happens even with much weaker initial fields (Liska et al. 2020) and also develops a MAD state. In order to see such effects, we would need much higher resolutions and longer runs as compared to the ones presented in this paper. However, some of our models, previously run in 2D and for shorter amounts of time with weaker initial magnetic field configurations, also showed the buildup of strong poloidal flux after a certain time (Janiuk et al. 2021).

4. Application to the Engine Modeling of Short and Long Gamma-Ray Bursts

4.1. Comparison with Previous Models for Gamma-Ray Bursts

We use our Ch85 model in the context of short GRBs, as a post-merger system in which an accretion disk has been formed. In a realistic scenario of a BNS system, the disrupted neutron star material is nonaxisymmetic and composed of clumps of matter with propagating shock waves (Foucart et al. 2014). Therefore, breaking the initial axisymmetry of the disk with the introduction of random perturbations in the ϕ-direction is justified.

Proga & Zhang (2006) used their hyperaccretion models for GRBs at late times and proposed that the episodic energy output in the jets is connected with changes in the mass supply driven by the accretion rate. They propose this as a model to

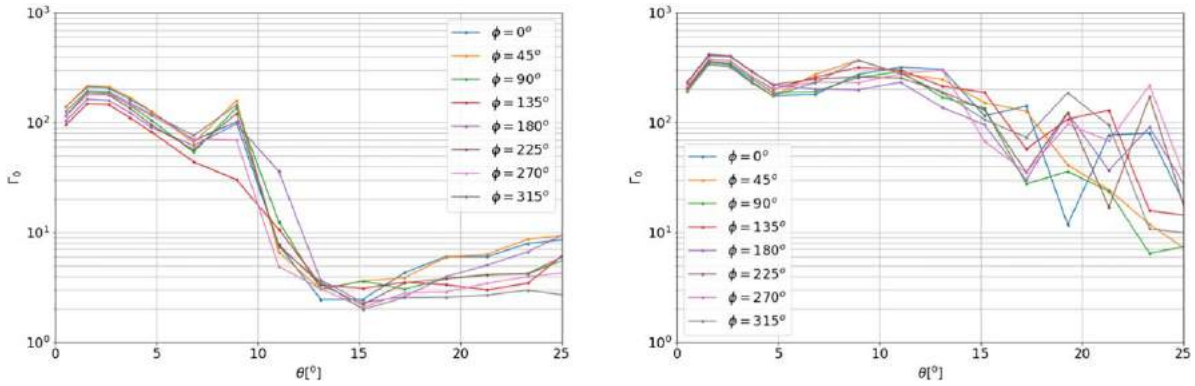

Figure 13. Time-averaged jet Lorentz factor measured at a large distance of 2000 r_g, as a function of the polar angle θ. Figure shows the jet profile at different selected slices of ϕ for the model with (a) Fishbone–Moncrief initial configuration (FM76), and (b) Chakrabarti initial configuration (Ch85).

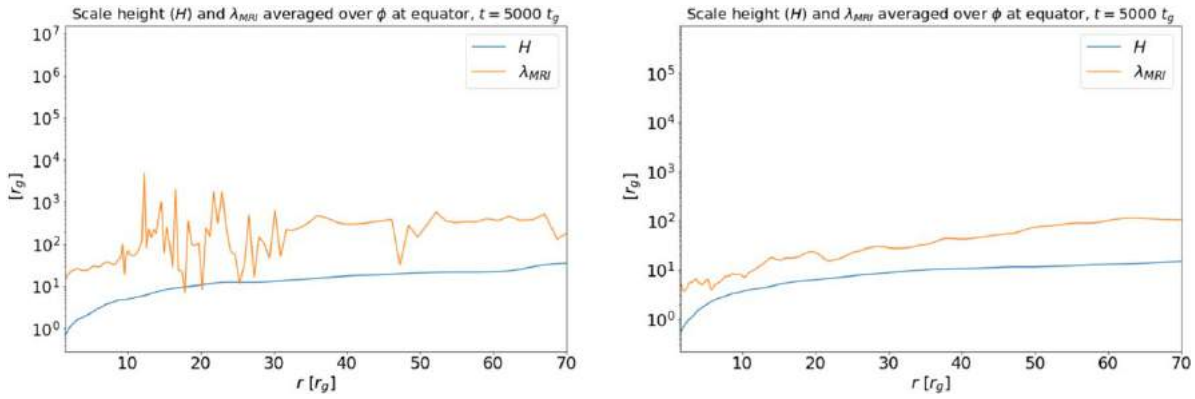

Figure 14. Comparison of the disk scale height (H) and the MRI wavelength at the equator, averaged over the azimuthal angle ϕ, at an evolved time $t = 5000\ t_g$ for (a) the FM76 model, and (b) the Ch85 model. We have $\lambda_{\rm MRI} \geqslant H$ throughout most part of the disk in both cases, indicating that the magnetic field is strong enough to suppress the MRI.

explain the X-ray flares observed from GRBs. They show with their chosen models that the energy release is repeatedly halted and restarted given the mass supply rate decreases with time, which is the case in both binary merger and collapsar scenarios. This is similar to the behavior observed in our previous work (Janiuk et al. 2021). In our current models there is no mass supply to the outer edge of the disk. The short episodic rise in the mass accretion rate in the initial stages is due to the dynamic nature of the magnetic field, and relaxation of the initial, stationary conditions, which was derived for a nonmagnetized disk. After the initial condition is relaxed, i.e., around time 5000 t_g, the variability of the accretion rate driven by interchange instabilities developed in the plasma continues in the MAD. The jet power is also varying and its magnitude is slowly decreasing with time. This can be partly connected to the falling mass accretion rate, which is decreasing at a slightly different rate. The rate of decrease of the jet power in both the models differs substantially. In the FM76 model it falls by three orders of magnitude as the simulation proceeds, while in the Ch85 model it falls by two orders of magnitude. The differences can be connected to the varying strength of magnetic flux on the black hole horizon.

Lloyd-Ronning et al. (2019) put limits on the magnetic field strength and the black hole mass needed to power Blandford–Znajek jets from the observed luminosities of short and long GRBs. They assume a central engine with black hole mass in the range of 0.5–4 $M_\odot$ for short GRBs and 2–10 $M_\odot$ for long GRBs, and they find that magnetic field strengths in the range of $\sim 5 \times 10^{14}$ to up to $\sim 10^{17}$ G (for the long GRBs) and $\sim 10^{15}$ to $\sim 10^{17}$ G (for the short GRBs) are needed to power the observed GRBs with the assumed mass of the central engine. The magnetic fields inferred from their analysis are extreme and in practice such fields can be generated and sustained only through special mechanisms. Generally, a small extant magnetic field in a disk can be amplified by the MRI. But, the MRI is suppressed in our simulations due to the magnetic arresting of the disk, which is evident from the growth of magnetic flux at the black hole horizon. The magnetic field strength at the black hole horizon at an evolved time (5000 t_g) in our long GRB model (FM76) is estimated as 3.51×10^{14} G and in our short GRB model (Ch85) it is 7.74×10^{14} G. This is in the range of previous estimations. Our simulations show that the disk can sustain such an amount of flux near the black hole horizon over time and presents such a configuration as a viable candidate for explaining the jet variability properties of the GRBs. For comparison, Kiuchi et al. (2014) evolve a high-resolution BNS merger scenario. In their simulations the magnetic field is amplified within multiple mechanisms including Kelvin–Helmholtz instability during the merger and MRI during post-merger evolution. They show it is possible to have a highly magnetized disk with magnetic field stronger than $10^{15.6}$ G over a big region of the disk.

Our FM76 model (model 1) is embedded in a poloidal magnetic field which follows the disk density structure with a dependence on the fifth power of radius. This analytic solution is a standard initial condition for a thick disk and the imposed

magnetic field is in such a way that it takes a short amount of time to accrete more poloidal flux to the black hole horizon. We consider this model as a candidate for the central engine of long GRBs. On the other hand, we consider our Ch85 model (model 2) embedded in a poloidal magnetic field due to a circular current at the radius of pressure maximum of the disk as a candidate for the central engine of short GRBs. In this model, the imposed magnetic field is in such a way that it takes shorter time to develop more poloidal magnetic flux on the black hole horizon, which results in a MAD. At a later time of the simulation ($t \sim 2500\ t_g$), the strength of the poloidal magnetic field at the inner region of the disk is $B_z = 1.53 \times 10^{-3}$ for the FM76 model and $B_z = 1.09 \times 10^{-3}$ for the Ch85 model (in code units), which is comparable.

4.2. Jet Opening Angles in Short and Long Gamma-Ray Bursts

Our numerical simulations can give a picture of the jet structure in the long and short GRBs based on the models we are considering for the two scenarios. The time-averaged jet Lorentz factor profile with θ gives information about where most of the energy in the jet is concentrated and the jet opening angles in our models. Based on their hydrodynamic and MHD simulations Nathanail et al. (2020) focused particularly on the properties of GRB 170817A. They observed a self-consistent jet launching in their MHD simulations. Their MHD jets have a hollow core of up to ∼4°–5° and the jets carry a significant amount of matter. When comparing to our models, we have a clearly hollow core up to an angle of 5° in our Ch85 model. On the other hand, the jet launched in our FM76 model has higher Lorentz factors closer to the axis, as well, compared to the Ch85 model. Yet in our FM76 model, also, even higher Lorentz factors are reached at a significant angle ($\theta \gtrsim 10°$) from the axis. Compared to their models, the jets in both of our models do not contain any considerable amount of matter. This is apparent from the density plots on the top-middle and right panels given in Figures 1 and 2.

Margutti et al. (2018) studied different models based on hydrodynamic simulations of the jet interaction with BNS ejecta to get opening angle values from GRB 170817A afterglow observations. They show two representative scenarios for jet opening angles of 5° and 15° considering a top-hat structure for the jet, assuming off-axis viewing angles $\theta_{\rm obs} \sim 15°$–$25°$. However, the top-hat jets viewed off-axis failed to reproduce the larger X-ray and radio luminosities in the early days after the prompt emission from the source and also failed to account for the mild and steady rise of the nonthermal emission observed. Thus, a simple top-hat structure is not a likely scenario for the afterglows of GW170817. Rather, a structured and collimated relativistic outflow is considered as the probable scenario for this observation, with the GRB assumed to be seen off-axis. Many other authors also support the scenario of a structured jet that is seen off-axis based on their models for this source (e.g., Kathirgamaraju et al. 2018). If we assume the inference of Margutti et al. (2018) that the GRB 170817A was a "classical" short GRB with a structured collimated jet and reached up to an energy of $\sim 10^{50}$ erg, observed off-axis, to be correct, we can consider the jet structure described by their models. The jet produced in their representative models with this assumption has a narrow ultra-relativistic core of $\theta_c \sim 9°$ with $\Gamma \sim 100$ surrounded by a mildly relativistic sheath up to angle of $\lesssim 60°$. In our models, the time-averaged terminal Lorentz factor profile computed at $\sim 2000\ r_{\rm g}$ (shown in Figure 13) also clearly shows the existence of structured jets. The Ch85 model, which we consider as a candidate for a short GRB central engine, also shows a complex structured jet profile with no clearly defined core region when averaged over time. In this model, the jet is confined to a rather broader angle of $\theta \lesssim 25°$. But, the jet produced in this model reaches the highest Lorentz factors at around an angle of ∼9°, which is in coincidence with the values of the narrow jet core in the models of Margutti et al. (2018). Figure 9 shows the internal substructure of the base of the jet from our simulations at a given time. Both these plots show the evolved nonaxisymmetric structured nature of the jet. They also qualitatively depict the jet core with higher Lorentz factors (∼150–200) at some certain angle away from the axis.

Another possible scenario, explaining why GRB 170817 is dimmer than a classical short GRB, is based on the fact that post-merger remnants are surrounded by high-speed, neutron-rich dynamical ejecta which produce heavy elements with high opacity through *r*-process nucleosynthesis. Therefore emissions from the inner parts can be partially masked by outer opaque material (Kasen et al. 2015). GRB 080503 is another example of a faint GRB accompanied by an extremely bright extended prompt X-ray emission. The faintness of this GRB can be explained by an off-axis jet, similar to GRB 170817 (Perley et al. 2009; Fong et al. 2015).

Fong et al. (2015) considered 11 short GRB events with equal weighting (see their Table 5) and calculated the jet opening angles by giving Gaussian probability distributions to the measurements they considered. Employing a realistic upper bound of $\theta_{j,\max} = 30°$ on the opening angles (obtained from the previously available post-merger black hole accretion simulations), they obtained a median value of $\langle \theta_j \rangle = 16° \pm 10°$. The jet from our Ch85 model has a value which tends toward the upper limit of this value. In the FM76 model we have a structured jet with most of the energetic part confined to $\theta \sim 11°$–$12°$. The profile for this model shows an ultra-relativistic core with $\Gamma \sim 100$ peaking around $\theta_c \sim 9°$. Fong et al. (2015) also computed the jet opening angles for long GRBs from the measurements of 248 samples and found a median value of $\langle \theta_j \rangle = 13^{+5}_{-9}$ degrees. The value of 11° obtained from our FM76 model matches with the lower bound of the estimated value from the observations.

4.3. Jet Variability Timescale in Short and Long Gamma-Ray Bursts

When we consider our model with a Chakrabarti initial torus (Ch85) as a plausible central engine for short GRBs, we can use a black hole mass of 3 $M_\odot$ to scale the physical quantities and compute the minimum variability time in seconds. We get an average value of 147.37 t_g for the minimum variability timescale from two chosen locations along the jet direction for this model. This scales to a value of 2.178 ms in physical units. Similarly, when we consider our FM76 model as a collapsar remnant disk and use a value of 10 $M_\odot$ for the central black hole, we can estimate the resulting minimum variability timescale. We get an average value of 224.21 t_g for the minimum variability timescale in code units from this model, which gives a value of 13.257 ms in physical units. MacLachlan et al. (2013) present a wavelet analysis using a collection of observed samples from Fermi data to show that the variability timescales of the short and long GRBs differ from each other. In their study, they found a marginal positive

correlation between the minimum variability timescale and burst duration for both classes of bursts. The lowest variability timescale from their study is 3 ms. Our results are in agreement with these observations.

Golkhou et al. (2015) put constraints on the minimum variability timescales for the GRBs observed by the Fermi/Gamma-ray Burst Monitor instrument. They found a median minimum timescale for long GRBs of 45 ms and for short GRBs of 10 ms. Only less than 10% of their selected samples show variability smaller than 2 ms, and this requires Lorentz factors higher than 400. The minimum variability timescales obtained from our models are in the lowest range of these observed values.

The power density spectra (PDS) computed for our models also reveal information about the time variability data. The variability of the energy blobs ejected close to the inner regions of the jet in both models have a smaller PDS slope as compared to the variability measured at the outer regions for the fitted power law. So, in general, the outer wall of the jet shows higher variability as compared to the inner part closer to the jet axis. Also, the power-law fit for the long GRB model has a steeper slope as compared to the short GRB model at both the locations in which the variability is measured. The slope (α) values are in the range though smaller than $5/3$, which is predicted by the turbulence model (Beloborodov et al. 2000). More recent observational studies give PDS slope values, with a power-law fit, in the range of 1.347–2.874 (Guidorzi et al. 2016) and 1.42–4.95 (Dichiara et al. 2016) for the long GRBs and in the range of 1.398–2.507 (Dichiara et al. 2013) for the short GRBs. Our results of the jet variability measured at the outer part are consistent with the lower limit of the observed PDS slopes.

Sonbas et al. (2015) found an anticorrelation between the minimum variability timescale and the bulk Lorentz factor for the GRB samples they considered from Swift and Fermi data. We have not calculated a sufficient number of models to do a parameter study for obtaining a correlation between the variability timescale and Lorentz factor. However, our models do systematically give smaller minimum variability timescales for higher Lorentz factors from our two models and also from different regions of the jet.

5. Summary and Conclusions

We have performed 3D GRMHD simulations of the accretion disk around a Kerr black hole considering two different initial analytical equilibrium solutions. The Chakrabarti initial solution has an angular momentum distribution constant over specific surfaces and changes with the radius rather than being constant over the entire disk. This arguably gives a more realistic scenario as compared to the initial FM solution. These solutions are imposed upon by poloidal magnetic fields that result in magnetic turbulence and MRI, which initially drives accretion. As the accretion proceeds the plasma brings more magnetic flux to the black hole horizon and results in a magnetically arrested accretion state which prevents further falling of matter into the black hole. We consider the MAD state as the plausible central engine of GRBs and investigate its effect on the time variability properties and the structure of the ejected jet. Our models self-consistently produce structured jets with a relatively hollow core, up to an angle of $\sim 5^\circ$, and higher Lorentz factors are reached on the edges of the jets. The two initial models and the imposed magnetic field geometry affect the jet structure, which is evident from the different profiles and internal structures of the jets. The models give a jet opening angle of $\sim 11^\circ$ and $\sim 25^\circ$, respectively, for the short and long GRBs, which is consistent with observations. Also, the minimum variability timescale is computed for both of our models, and they are found to be in the lower range of the variability timescale from observations. Finally, the PDS spectral slopes are somewhat flatter than the classical $\alpha = 5/3$ slope, but within the observed range.

From our work, it can be seen that the MAD model can serve as a plausible central engine in the context of both classes of GRBs. In the collapsar scenario, our models can be considered as an initial approximation, as we do not evolve it for longer timescales observed for such systems. In the short GRB regime, our models show that a MAD can be formed in such short timescales if the initial magnetic fields are strong enough near to the black hole horizon. The structured jets and the opening angles from our models are in agreement with the values from observations of a collection of GRB samples in both cases. However, jet structure and opening angles vary significantly between each individual burst and such differences need further investigation of more possible initial configurations. Our models are also able to explain the subsecond time variability, and the MTS values are in good agreement with observations. The observed correlations between the MTS and bulk Lorentz factor of the jets can be investigated by a further parameter study of our models with different initial magnetic field strengths and black hole spin values. This can also help in understanding the dependence of the jet structure and opening angles on the varying initial conditions. There is also the possibility of more detailed studies of time variability from our models to detect coherent fluctuations at various radii and propagating signals or time lags (e.g., as in Bollimpalli et al. 2020).

We thank the anonymous referee for the valuable comments that helped to improve our manuscript. We thank Kostas Sapountzis and Om Sharan Salafia for helpful discussions and comments. This research was supported in part by grant No. DEC-2019/35/B/ST9/04000 from the Polish National Science Center. This research was carried out with the support of the Interdisciplinary Center for Mathematical and Computational Modeling at the University of Warsaw (ICM UW) under the grant Nos. g85-986 and g86-987.

Software: `Matplotlib` (Hunter 2007), `NumPy` (Harris et al. 2020), `SciPy` (Virtanen et al. 2020), and `VisIt` (Childs et al. 2012).

ORCID iDs

Bestin James https://orcid.org/0000-0003-2088-7713
Agnieszka Janiuk https://orcid.org/0000-0002-1622-3036
Fatemeh Hossein Nouri https://orcid.org/0000-0003-1449-0824

References

Abbott, B. P., Abbott, R., Abbott, T. D., et al. 2017, PhRvL, 119, 161101
Abramowicz, M. A., & Fragile, P. C. 2013, LRR, 16, 1
Balbus, S. A., & Hawley, J. F. 1991, ApJ, 376, 214
Beloborodov, A. M., Stern, B. E., & Svensson, R. 2000, ApJ, 535, 158
Bisnovatyi-Kogan, G. S. 2019, Univ, 5, 146
Blandford, R. D., & Znajek, R. L. 1977, MNRAS, 179, 433
Bollimpalli, D. A., Mahmoud, R., Done, C., et al. 2020, MNRAS, 496, 3808
Boyer, R. H., & Lindquist, R. W. 1967, JMP, 8, 265
Burrows, A., Dessart, L., Livne, E., Ott, C. D., & Murphy, J. 2007, ApJ, 664, 416

Chael, A., Narayan, R., & Johnson, M. D. 2019, MNRAS, 486, 2873
Chakrabarti, S. K. 1985, ApJ, 288, 1
Childs, H., Brugger, E., Whitlock, B., et al. 2012, in High Performance Visualization-enabling Extreme-scale Scientific Insight (Boca Raton, FL: CRC Press), 357
Di Matteo, T., Perna, R., & Narayan, R. 2002, ApJ, 579, 706
Dichiara, S., Guidorzi, C., Amati, L., Frontera, F., & Margutti, R. 2016, A&A, 589, A97
Dichiara, S., Guidorzi, C., Frontera, F., & Amati, L. 2013, ApJ, 777, 132
Duez, M. D. 2010, CQGra, 27, 114002
Fishbone, L. G., & Moncrief, V. 1976, ApJ, 207, 962
Fong, W., Berger, E., Margutti, R., & Zauderer, B. A. 2015, ApJ, 815, 102
Foucart, F., Deaton, M. B., Duez, M. D., et al. 2014, PhRvD, 90, 024026
Galama, T. J., Vreeswijk, P. M., van Paradijs, J., et al. 1999, A&AS, 138, 465
Gammie, C. F., McKinney, J. C., & Tóth, G. 2003, ApJ, 589, 444
Gammie, C. F., Shapiro, S. L., & McKinney, J. C. 2004, ApJ, 602, 312
Golkhou, V. Z., Butler, N. R., & Littlejohns, O. M. 2015, ApJ, 811, 93
Guidorzi, C., Dichiara, S., & Amati, L. 2016, A&A, 589, A98
Harris, C. R., Millman, K. J., van der Walt, S. J., et al. 2020, Natur, 585, 357
Hunter, J. D. 2007, CSE, 9, 90
Igumenshchev, I. V. 2008, ApJ, 677, 317
Igumenshchev, I. V., Narayan, R., & Abramowicz, M. A. 2003, ApJ, 592, 1042
Jackson, J. D. 1998, Classical Electrodynamics (3rd ed; New York: Wiley), doi:10.1063/1.56557
Janiuk, A., James, B., & Palit, I. 2021, ApJ, 917, 102
Janiuk, A., Perna, R., Di Matteo, T., & Czerny, B. 2004, MNRAS, 355, 950
Jaroszynski, M. 1996, A&A, 305, 839
Just, O., Obergaulinger, M., Janka, H. T., Bauswein, A., & Schwarz, N. 2016, ApJL, 816, L30
Kasen, D., Fernández, R., & Metzger, B. D. 2015, MNRAS, 450, 1777
Kathirgamaraju, A., Barniol Duran, R., & Giannios, D. 2018, MNRAS, 473, L121
Kiuchi, K., Kyutoku, K., Sekiguchi, Y., Shibata, M., & Wada, T. 2014, PhRvD, 90, 041502
Kouveliotou, C., Meegan, C. A., Fishman, G. J., et al. 1993, ApJL, 413, L101
Li, L.-X. 2000, ApJL, 531, L111
Liska, M., Tchekhovskoy, A., & Quataert, E. 2020, MNRAS, 494, 3656
Liu, T., Gu, W.-M., & Zhang, B. 2017, NewAR, 79, 1
Lloyd-Ronning, N. M., Dolence, J. C., & Fryer, C. L. 2016, MNRAS, 461, 1045
Lloyd-Ronning, N. M., Fryer, C., Miller, J. M., et al. 2019, MNRAS, 485, 203
MacLachlan, G. A., Shenoy, A., Sonbas, E., et al. 2013, MNRAS, 432, 857
Margutti, R., Alexander, K. D., Xie, X., et al. 2018, ApJL, 856, L18
Margutti, R., & Chornock, R. 2021, ARA&A, 59, 155
McKinney, J. C., & Gammie, C. F. 2004, ApJ, 611, 977
McKinney, J. C., Tchekhovskoy, A., & Blandford, R. D. 2012, MNRAS, 423, 3083
Mizuta, A., Ebisuzaki, T., Tajima, T., & Nagataki, S. 2018, MNRAS, 479, 2534
Narayan, R., Chael, A., Chatterjee, K., Ricarte, A., & Curd, B. 2021, MNRAS, 511, 3795
Narayan, R., Igumenshchev, I. V., & Abramowicz, M. A. 2003, PASJ, 55, L69
Nathanail, A., Gill, R., Porth, O., Fromm, C. M., & Rezzolla, L. 2020, MNRAS, 495, 3780
Noble, S. C., Gammie, C. F., McKinney, J. C., & Del Zanna, L. 2006, ApJ, 641, 626
Paczynski, B. 1991, AcA, 41, 257
Paschalidis, V., Etienne, Z. B., & Shapiro, S. L. 2013, PhRvD, 88, 021504
Penna, R. F., Narayan, R., & Sądowski, A. 2013, MNRAS, 436, 3741
Perego, A., Yasin, H., & Arcones, A. 2017, JPhG, 44, 084007
Perley, D. A., Metzger, B. D., Granot, J., et al. 2009, ApJ, 696, 1871
Piran, T. 2004, RvMP, 76, 1143
Popham, R., Woosley, S. E., & Fryer, C. 1999, ApJ, 518, 356
Proga, D., & Begelman, M. C. 2003, ApJ, 592, 767
Proga, D., MacFadyen, A. I., Armitage, P. J., & Begelman, M. C. 2003, ApJL, 599, L5
Proga, D., & Zhang, B. 2006, MNRAS, 370, L61
Rezzolla, L., Giacomazzo, B., Baiotti, L., et al. 2011, ApJL, 732, L6
Richers, S., Kasen, D., O'Connor, E., Fernandez, R., & Ott, C. D. 2015, ApJ, 813, 38
Ruiz, M., Tsokaros, A., & Shapiro, S. L. 2020, PhRvD, 101, 064042
Sapountzis, K., & Janiuk, A. 2019, ApJ, 873, 12
Sharma, V., Iyyani, S., & Bhattacharya, D. 2021, ApJL, 908, L2
Siegel, D. M., & Metzger, B. D. 2018, ApJ, 858, 52
Sonbas, E., MacLachlan, G. A., Dhuga, K. S., et al. 2015, ApJ, 805, 86
Tchekhovskoy, A., Narayan, R., & McKinney, J. C. 2011, MNRAS, 418, L79
Virtanen, P., Gommers, R., Oliphant, T. E., et al. 2020, Nat. Methods, 17, 261
Visser, M. 2007, arXiv:0706.0622
Vlahakis, N., & Königl, A. 2003, ApJ, 596, 1080
Weinberg, S. 1972, Gravitation and Cosmology: Principles and Applications of the General Theory of Relativity (New York: Wiley)
White, C. J., Stone, J. M., & Quataert, E. 2019, ApJ, 874, 168
Woosley, S. E. 1993, ApJ, 405, 273

Chapter 5

Black hole outflows driven by accretion of large scale magnetic fields

This chapter presents the initial results from an unpublished work that is still in progress at the time of writing this thesis. In this project, we investigate and explore properties of outflows driven by large-scale magnetic fields in the vicinity of an accreting black hole. This chapter does not focus solely on jets, but rather investigate the magnetized accretion in the central engines and the associated outflows mainly in the equatorial region. Such outflows may form mainly in the equatorial region, even if the accretion flow does not contain any angular momentum. They are driven by the repulsive effects of black hole magnetosphere for extremely fast spinning black holes.

We examine the competing effects of mass inflows and outflows driven by a large scale asymptotically uniform magnetic field in the Kerr geometry starting from a spherically symmetric inflow. This in turn results in the accretion of magnetic field lines along with the plasma while intermittent outflows develop mainly in the equatorial region. If the flow possess some angular momentum, then for its super-critical values, a mini-disk may form, and help launching also bi-polar jets, as studied e.g. by Murguia-Berthier et al., 2020. This work provides new insights into the effects of magnetized accretion onto rotating black holes and the associated outflows.

This work is done in collaboration with Prof. Vladimír Karas from the Astronomical Institute, Czech Academy of Sciences, and my supervisor. I performed all the numerical simulations and data analysis presented in this work. The initial configurations and the results were discussed during our weekly meetings with by Prof. Karas and my supervisor.

5.1 Introduction

Black holes attract the gaseous material from their surrounding environment (Rees and Volonteri, 2006). The accretion of plasma onto the black hole due to its gravitational effect produces various observable phenomena like relativistic jets and outflows in the form of winds (Fender and Gallo, 2014). We have seen in the previous chapters that plasma at large scales is magnetized due to its environment. As the accretion proceeds, very high magnetic pressures can develop near the black hole horizon, which can act against the accretion itself. This sometimes leads to the formation of the Magnetically Arrested Disk (MAD; Narayan, Igumenshchev, and Abramowicz, 2003; Tchekhovskoy, Narayan, and McKinney, 2011; Event Horizon Telescope Collaboration et al., 2021) as previously discussed. The accumulated magnetic flux

can inhibit the further accretion and it plays a role in the formation of relativistic jets and other outflows observed in the black hole sources. The velocity of the plasma acquires a significant azimuthal component close to the event horizon of the black hole, even when it is a purely spherical Bondi-type inflow at a large distance from the black hole. This effect is due to a combination of the requirement for angular momentum conservation of the infalling medium and the frame-dragging effect of the Kerr black hole.

Blandford and Znajek, 1977 described a now widely known mechanism which supports the formation and collimation of jets from a Kerr black hole surrounded by a magnetic field as discussed already in Section 1.6. By this mechanism, the jet formed can extract energy from the rotation of the black hole, which was later demonstrated in GRMHD simulations (Tchekhovskoy, Narayan, and McKinney, 2011). On the other hand, in the case of rapidly spinning black holes a Meissner-like expulsion of magnetic field lines from the horizon is expected that can adversely affect the operability of the BZ mechanism (Bicak and Janis, 1985; King, Lasota, and Kundt, 1975). But later, it was shown that this expulsion effect diminishes by the inward force of accretion and the BZ mechanism is often sustained (Komissarov and McKinney, 2007). The black hole does not hold the magnetic field by itself. When the accretion rate decreases, the magnetic field lines can force plasma clumps away from the black hole. It can lead to an outflow in the disk, where a current sheet forms as the inflow is inhibited magnetically (Ripperda, Bacchini, and Philippov, 2020; Ripperda et al., 2022).

Even though the occurrence of the magnetically arrested state is frequently observed in GRMHD simulations of accreting black holes, the development of the system is rather sensitive to the conditions at the outer boundary, the dimensionality of the computation, and other initial assumptions about the flow. In their study, El Mellah et al. (2022) identified a separatrix and current sheet in such flows where particles can be accelerated along a characteristic inclination angle. This can also be seen in the synchrotron emission when radiation losses were included in the computations. Similarly, Crinquand et al. (2022) discovered a persistent equatorial current sheet and flaring activity in a low accretion state. Meanwhile, Kwan, Dai, and Tchekhovskoy (2022) explored Bondi-type accretion and found that even in that system, the flow can be magnetically arrested, producing episodic jets launched along the common rotation axis of the black hole and the accretion disk. Lastly, Ressler et al. (2021) examined zero angular momentum accretion onto a rapidly rotating black hole, finding that the jet power peaks when the magnetic field is initially tilted with respect to the black hole's spin axis, as this maximizes the magnetic flux across the event horizon.

In this work, we focus on the equatorial outflows in an accreting plasma around a central black hole mediated by the presence of large-scale magnetic fields. Outflows like these are considered recently to explain the observed properties of M87*, with an in-fall of matter at a larger radius and an ejection disc at a smaller radius (Blandford and Globus, 2022). Here, we are interested in a gradually evolving structure of the magnetic field and the mass flow in the regions near the black hole horizon in the presence of a large-scale uniform magnetic field (e.g. Wald, 1974). We use an initially spherically symmetric inflow, such that it develops into a Bondi-type solution (Bondi, 1952), as we evolve it in time. In the next section, the numerical setup and the models used for our investigations are described.

5.2 Numerical setup and models

5.2.1 Code setup

For all the models in this work, we evolve the accretion onto a black hole in a fixed Kerr metric. The metric is not evolved in time with the assumption that the accreted mass is negligible in comparison to the black hole mass over the timescale considered. This is the same assumption as in the previous chapters. For other possibilities, e.g. studies with evolving Kerr metric and black hole spin and mass changes due to massive accretion in collapsars, see the study by Król and Janiuk, 2021. We assume the ideal MHD and evolve its equations with the numerical code HARM. The basic description of the code is the same as given in Chapter 2.

The outer boundary of the computational domain is set at $10^5\ r_g$ and the inner boundary is located at $0.98\ r_H$, i.e. a fraction inside the event horizon radius, for the corresponding value of black hole spin a. The 2D grid domain has a resolution of 600×512 in the (r, θ) directions. For the 3D grid, we use a resolution of $288 \times 256 \times 128$ in the (r, θ, ϕ) directions. We use a uniform angular resolution for the grid by setting the h_{slope} parameter to the value 1.0, in contrast to the models studied in the previous chapters where we used smaller h_{slope} values to focus the grid cells in the equatorial region.

The adiabatic index is assumed to be that of an ideal gas with $\gamma = 4/3$. We use the plasma β parameter which is defined as the gas to magnetic pressure ratio $(p_{\rm gas}/p_{\rm mag})$ to initially set the maximum magnetic field strength in the models as the field is enabled, where, $p_{\rm gas} = (\gamma - 1)u_{\rm max}$ and $p_{\rm mag} = b^2_{\rm max}/2$. Here, $u_{\rm max}$ is the maximum of the internal energy of the gas, which is located nearest to the black hole horizon.

5.2.2 Models

We begin all our models with a uniform density over the entire computational grid with a Kerr black hole at the center and with no magnetic field around. This configuration is evolved with time, as we see the gas starts accreting to the black hole, and the mass accretion rate rises and reaches a quasi-steady value. The evolution of the accretion rate at this stage is plotted in Figure 5.1. At this point (at 1000 t_g in our models), we introduce the magnetic field of the chosen strength and geometry in our code.

The magnetic field in our models is prescribed according to the solution for an asymptotically uniform magnetic field around a Kerr black hole in vacuum given by the Wald (1974) solution. The field given by this solution is symmetrically aligned with the rotation axis of the black hole. For this configuration, the magnetic field can be fully described by the only non-vanishing components of the vector potential

$$A_t = B_0 a [r\Sigma^{-1}(1 + \cos^2\theta) - 1] \tag{5.1}$$

$$A_\phi = B_0 [\frac{1}{2}(r^2 + a^2) - a^2 r\Sigma^{-1}(1 + \cos^2\theta)] \sin^2\theta, \tag{5.2}$$

with $\Sigma = r^2 + a^2 \cos^2\theta$.

The instance when we turn on the magnetic field (at t = 1000 t_g), for one typical model, are depicted in the left panels of Figures 5.2 and 5.3, showing the density contours in log-scale with overplotted magnetic field lines and velocity streamlines. At this point, the plasma distribution posses a Bondi-type steady accretion rate it acquired from the earlier part of the simulation. The velocity streamline plot in the

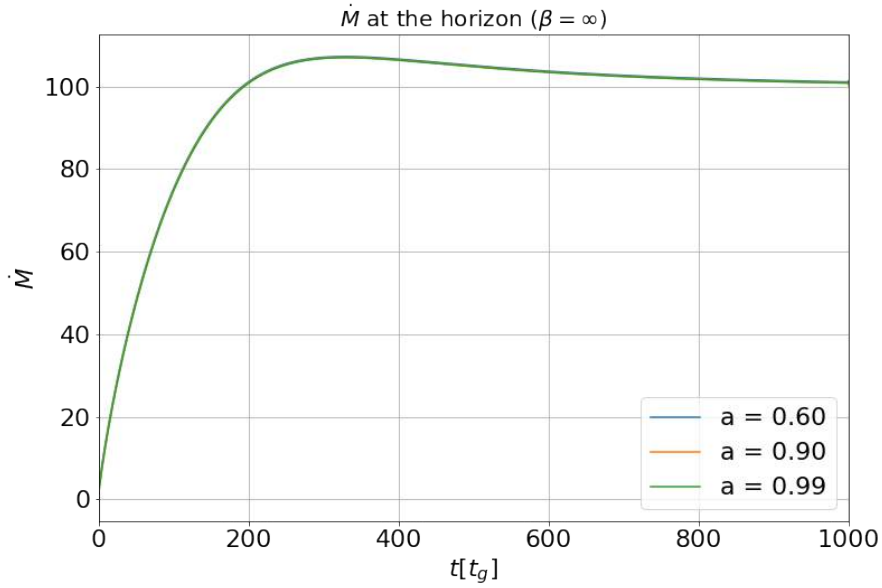

FIGURE 5.1: Mass accretion rate rate on the black hole horizon for the initial part of the simulation before the magnetic field is turned on ($\beta = \infty$). The value initially grows and saturates to a quasi-stationary value as the time proceeds. It is in geometric units which can be scaled with the black hole mass M. The accretion rate for all the black hole spin values are the same as we use the same initial conditions for the density.

top panel of Figure 5.3 shows the uniform spherical inward accretion state at this instance. At the instance we turn on the magnetic field, the field lines are expelled from the black hole horizon similar to the standard Meissner effect. This effect is expected for any rotating black hole with the maximally spinning case showing the highest degree of expulsion (Bicak and Janis, 1985; King, Lasota, and Kundt, 1975). This effect is clearly visible on the top panel of Figure 5.2 . All our models are evolved further and studied in detail from this instance when we turn on the magnetic field.

5.3 Results and discussion

A summary of models we studied are listed in Table 5.1 and their names reflect the parameter values used for them and the setup (2D or 3D). The middle and bottom panels of Figure 5.2 show the evolved states of a fiducial model b01.a90.2D up to a radius of 20 r_g. In regions below 5 r_g in the top panels, we can notice frozen in magnetic field lines reconnected while being accreted onto the black hole. These plots also show the disappearance of the Meissner-like expulsion of magnetic field lines, and thus the magnetic flux is accumulated nearby the black hole horizon as the accretion proceeds. The density structures in the middle and bottom panels of Figure 5.3 show the mass outflows developed in the equatorial region and their velocity directions. This is more clear in the velocity streamlines overplotted in the Figure. All our magnetized models develop equatorial mass outflows similar to the model depicted in Figure 5.3.

Figure 5.4 shows the time-evolution of magnetic flux on the black hole horizon for the models with initial maximum $\beta = 0.1$. The magnetic flux on the black hole

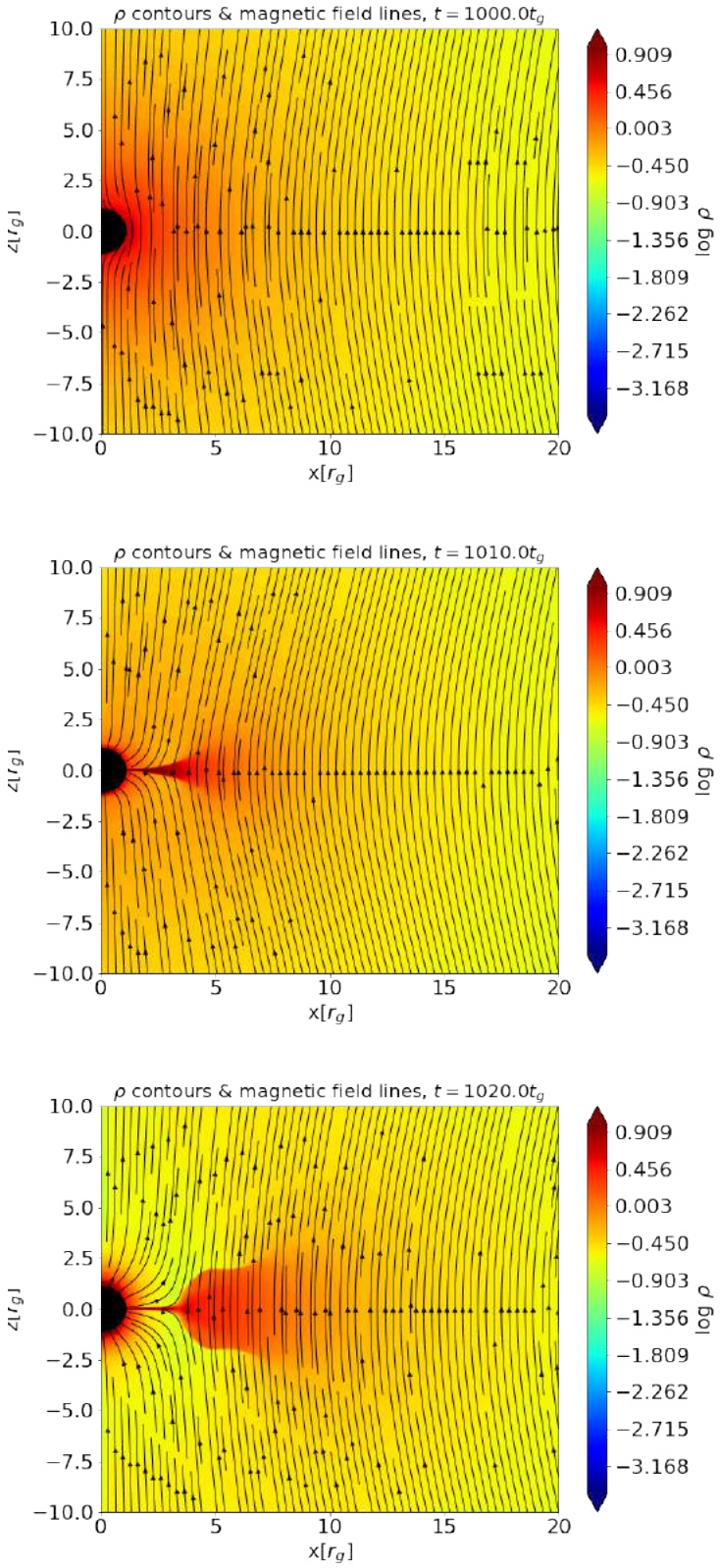

FIGURE 5.2: The initial and evolved states for the 2D model with β = 0.1 and a = 0.90 after the magnetic field is turned on, with fluid density in color contours and the magnetic field lines plotted on top.

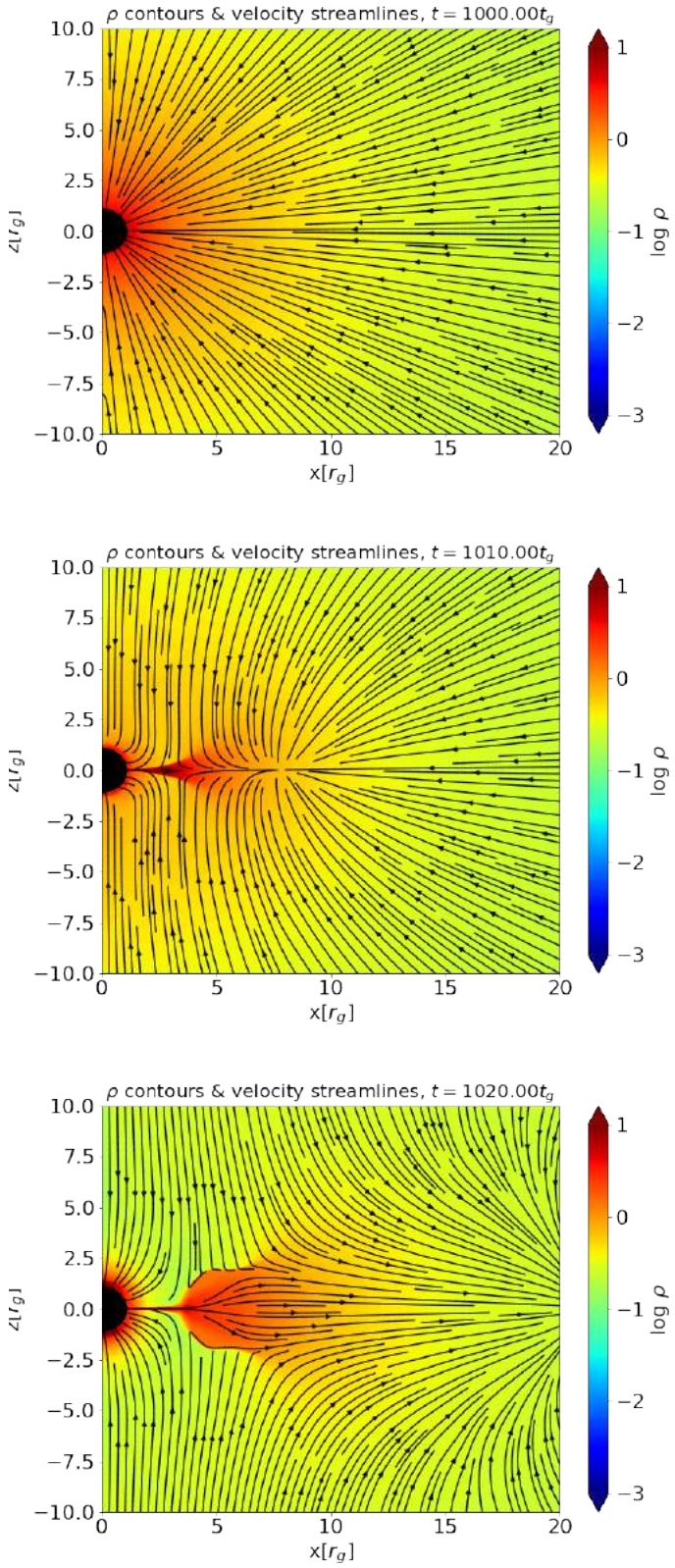

FIGURE 5.3: The initial and evolved states for the 2D model with β = 0.1 and a = 0.90 after the magnetic field is turned on, with fluid density in color contours with velocity streamlines plotted on top.

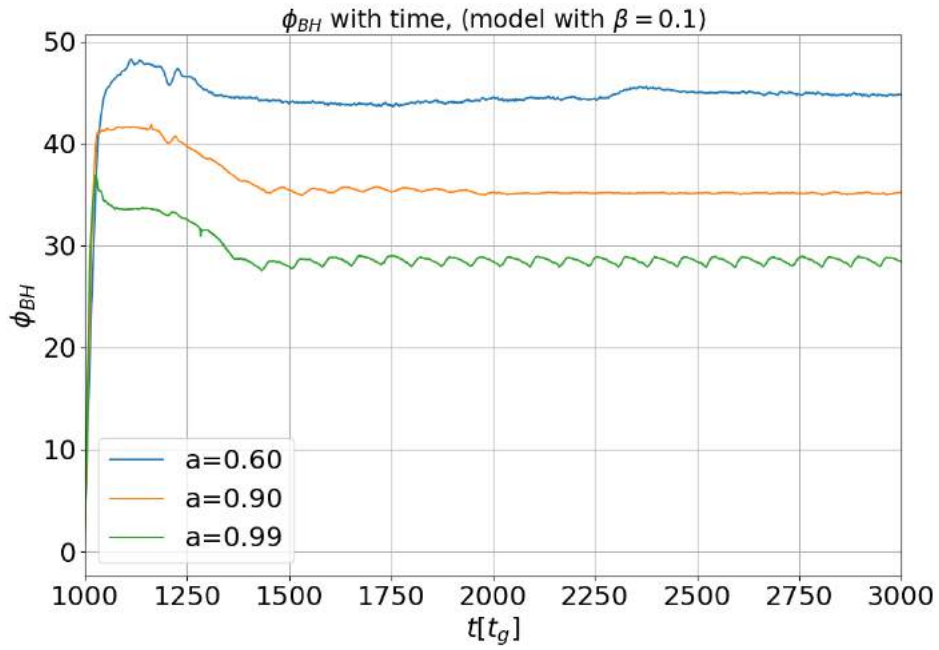

FIGURE 5.4: The evolution of magnetic flux on the black hole horizon with time for the 2D models with $\beta = 0.1$ and with different spin values from time $t = 1000\ t_g$.

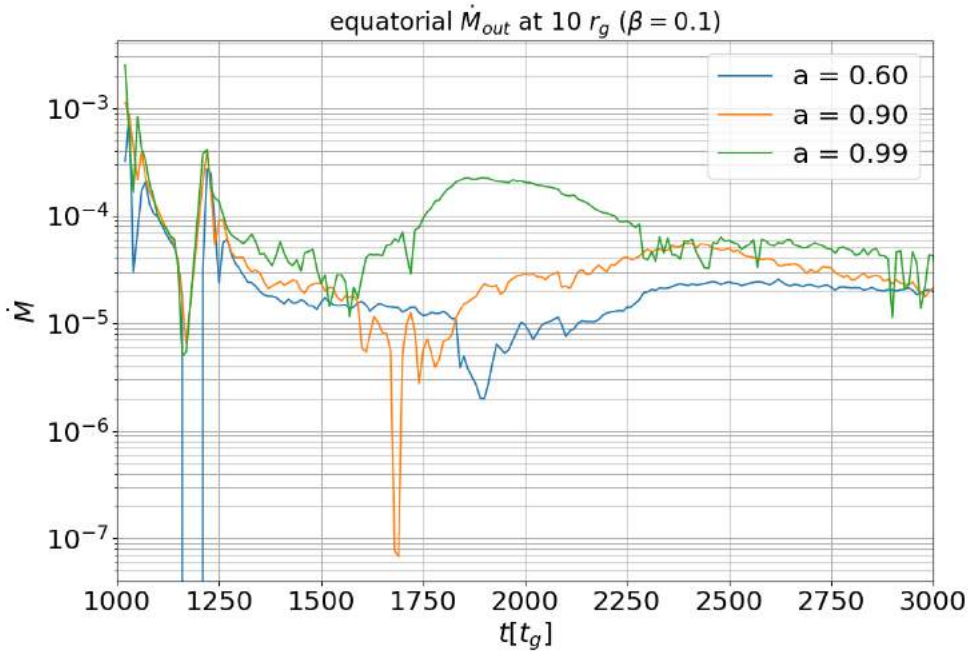

FIGURE 5.5: The equatorial mass outflow rate with time at 10 r_g, after the magnetic field is turned on, for the 2D models with $\beta = 0.1$ and different spin values.

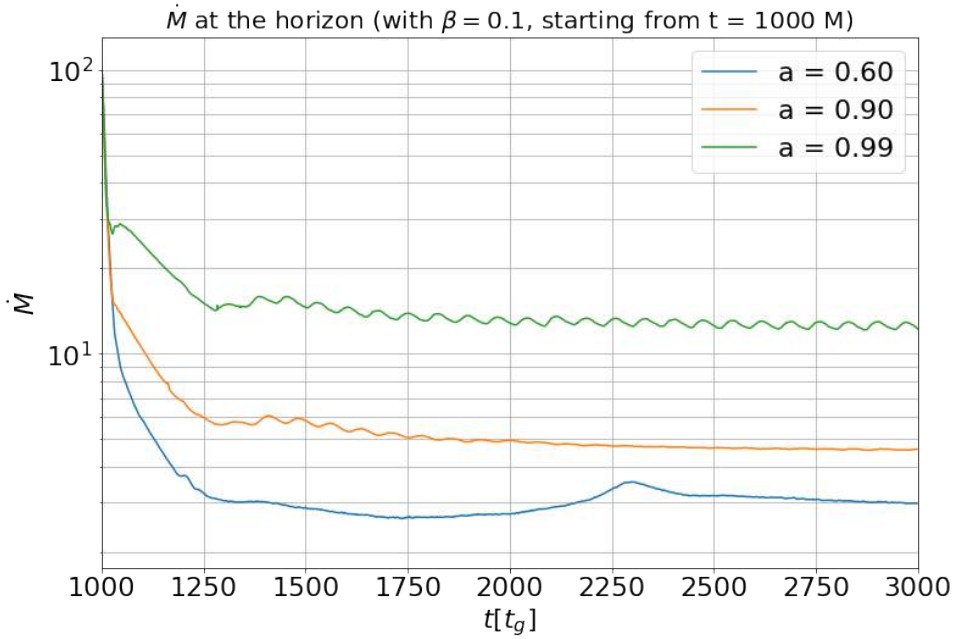

FIGURE 5.6: The evolution of inward mass accretion rate at the black hole horizon with time, after the magnetic field is turned on, for the 2D models with $\beta = 0.1$ and different spin values.

TABLE 5.1: Summary of models investigated.

Model	β_{max}	a	$\langle \dot{M}_{\rm in,H} \rangle_t$ (code units)	$\langle \phi_{\rm BH} \rangle_t$	$\langle \dot{M}_{\rm out,10r_g} \rangle_t$ (code units)	$\langle \dot{M}_{\rm out,10r_g} \rangle_t$ ($M_\odot$ yr^{-1})
b1.a0.2D	1.0	0	4.58	43.08	3.00×10^{-5}	1.060×10^{-7}
b1.a60.2D	1.0	0.60	2.18	41.95	3.07×10^{-5}	1.084×10^{-7}
b1.a90.2D	1.0	0.90	2.30	35.06	4.82×10^{-5}	1.703×10^{-7}
b1.a99.2D	1.0	0.99	4.41	28.72	8.11×10^{-5}	2.864×10^{-7}
b05.a0.2D	0.5	0	3.06	45.73	2.36×10^{-5}	8.325×10^{-8}
b05.a60.2D	0.5	0.60	1.92	43.44	2.45×10^{-5}	8.666×10^{-8}
b05.a90.2D	0.5	0.90	2.44	35.57	3.99×10^{-5}	1.410×10^{-7}
b05.a99.2D	0.5	0.99	4.56	28.88	6.87×10^{-5}	2.429×10^{-7}
b01.a0.2D	0.1	0	3.60	46.78	2.16×10^{-5}	7.645×10^{-8}
b01.a60.2D	0.1	0.60	3.60	44.67	2.81×10^{-5}	9.941×10^{-8}
b01.a90.2D	0.1	0.90	5.53	35.68	4.29×10^{-5}	1.515×10^{-7}
b01.a99.2D	0.1	0.99	14.34	29.04	9.18×10^{-5}	3.243×10^{-7}
b01.a90.3D	0.1	0.90	3.94	43.36	8.50×10^{-5}	3.003×10^{-7}
b01.a99.3D	0.1	0.99	9.34	32.41	12.65×10^{-5}	4.468×10^{-7}

Note: The models are parameterized by the initial maximum plasma β and the dimensionless Kerr parameter a. The time-averaged mass accretion rate at the horizon and the equatorial mass outflow rate at 10 r_g are computed after the magnetic field is turned on (i.e. from 1000 t_g). The outflow rate given in the last column is the estimated value in physical units considering our model of mass ejection for the M87 central engine.

horizon is quantified by integrating the radial component of the magnetic field over the horizon and by normalizing it to the inward mass flux,

$$\phi_{BH}(t) = \frac{1}{2\sqrt{\dot{M}}} \int_{\theta} \int_{\phi} \mid B^{r}(r_H, t) \mid dA_{\theta\phi}. \tag{5.3}$$

The initial flux is very high as the initial uniform field strength is 10 times higher than the gas pressure. As the accretion proceeds, this flux diminishes a slight extend, but still keeps high with values of $\phi_{BH} \sim 30 - 45$. Values in this range can suggest that the accretion is magnetically arrested and further inflow of matter can occur through magnetic reconnections and interchange instabilities as discussed in Section 1.5.

The mass outflows are sustained in time as can be seen from the outflow rates plot (again for the models with $\beta = 0.1$) shown in Figure 5.5, computed at 10 r_g. This is the case with all our models, with the highly magnetized models showing the highest outflow rates when averaged over time.

Figure 5.6 shows the inward mass accretion rate at the black hole horizon for the models with $\beta = 0.1$. We can notice some quasi-periodic fluctuations in the mass accretion rate as well as the magnetic flux on the horizon (in Figure 5.4) and these effects seem to depend on the black hole spin. From these plots, it is also evident that the model with highest black hole spin shows the highest mass outflow rate as well the highest mass accretion rate.

From the models presented in Table 5.1, we note that the black hole spin has a clear influence on the rate of mass outflows. The outflows rates show an increasing pattern with the black hole spin parameter ranging from $a = 0.60$ to 0.99, systematically in all models with varying magnetic field strength. This can be attributed partially to the Meissner-like expulsion of magnetic field lines by the rotating black holes which increases with the spin of the black hole, which in turn reflects in the outflow rates. At the same time, the strength of magnetization does not show a clear influence on the rate of outflows. All the models varying from $\beta = 0.1$ to 1 show similar outflow rates without a clear trend. On the other hand, the black hole spin shows a less pronounced effect on the inward mass accretion rate. The accretion rates have similar values for the dimensionless spin values of $a = 0.60$ and 0.90 in all levels of magnetization. And it shows slightly higher values for the near to maximally spinning cases. But, the Schwarzchild cases show higher accretion rates than the Kerr black holes, except in the most highly magnetized case. The table also lists the time averaged values of the dimensionless flux of the magnetic field on the black hole horizon ($\phi_{\rm BH}$).

In the last column of Table 5.1, we give the estimated mass outflow rate for a realistic system considering its known physical parameters. For this, we converted our results from the code units into physical units as follows. Since we use a unit convention of $G = c = M = 1$ in the code, the length and time units for the simulations results are given by $L_{\rm unit} = GM/c^2$ and $T_{\rm unit} = GM/c^3$ respectively. So the length and time values can be converted to physical units by using the relevant value of the black hole mass. Table 5.2 lists the conversion of geometric to physical units considering the black hole mass for M87*. Now, the density unit of the plasma around the black hole is related to the length unit by $\rho_{\rm unit} = M_{\rm scale}/L^3_{\rm unit}$ so that $M_{\rm scale}$ will depend on the environment under consideration. This density scaling for the AGN accreting environments is rather arbitrary (than for GRBs) as the spatial extension of the plasma is large and the density drops by many orders of magnitude from the black hole to the broad line region (Czerny et al., 2016). In Table 5.1, we give the outflow rates from our model for the M87 central engine assuming a black hole mass

TABLE 5.2: Example for the conversion of geometric to cgs units. Here we adopt a black hole mass of $M = 6.2 \times 10^9 M_\odot$ considering the M87*

Physical quantity	Geometric units	cgs units
Length	$r_g = GM/c^2$	9.159×10^{14} cm
Time	$t_g = GM/c^3$	3.055×10^4 s

of $6.2 \times 10^9 M_\odot$ and a density scaling of $\rho_{\rm unit} = 8.85 \times 10^{-18}$g cm^{-3} (Janiuk and James, 2022).

We also investigated two models in 3D, with the same initial configuration (for $a = 0.90$ and 0.99) for the most highly magnetized case ($\beta = 0.1$) to more correctly account for the evolution of the system. These models are more computationally expensive and hence we did not make a study on a family of models as in the 2D cases. Figures 5.7 and 5.8 show the initial (the instance when the magnetic field is turned on; 1000 t_g) and evolved density states from the 3D models. The first set of plots (Fig. 5.7) show the magnetic field lines from the models plotted on top of the density contours (on poloidal and equatorial slices). The second set of show the velocity streamlines at similar time instances. As similar to the 2D models, here also we can notice equatorial outflows developed due the magnetic reconnection events in the equatorial region in the nearest vicinity of the black hole. By analyzing the equatorial slices, we can notice the outflows expanding in time. We also notice than there are discontinuities in velocity, but the outflow is expanding, which also means that the eruptions are discontinuous. But with time, the outflows expand and continue towards the outer boundary of the computational domain. In Figure 5.10, we plot the magnetic flux on the black hole horizon in the case of the 3D models. The values from the 2D models with the same parameters are included for comparison. From this we notice that the flux is slightly lower for the 3D models with the same parameters, but they both are in the same order of magnitude as well as in the magnetically arrested accretion state. We can also notice that there are less fluctuations in these values for the 3D models. Figure 5.11 shows the azimuthally averaged equatorial outflow rate with time, computed at 10 r_g, for the 3D models. They are in the same order of magnitude as in the 2D ones, and the time averaged values are given in Table 5.1. From the values given the table, we notice that the outflow rate is systematically higher in both the 3D models compared to their 2D counterparts. The possibility for outflows along different azimuthal directions might be a reason for this. More investigations are required to be done to establish the reasons for this behavior. Finally, Figure 5.12 shows the inward mass accretion rate at the black hole horizon for the 3D models. We can notice the quasi-periodic fluctuations in the accretion rate are more smoothed out in the 3D models similar to the fluctuations in the magnetic flux.

Analytic models similar to the configuration we are considering, in which a spherically symmetric inflow at a large radius and an ejection disk at a smaller radius, are recently considered to account for the observed variability in M87 (Blandford and Globus, 2022). The numerical study of outflows presented in this chapter can be relevant in this context. We use our models to explain the basic mechanism behind these outflows and provide estimates for the outflow rates. Kwan, Dai, and Tchekhovskoy, 2023 also investigated Bondi-type low specific angular momentum

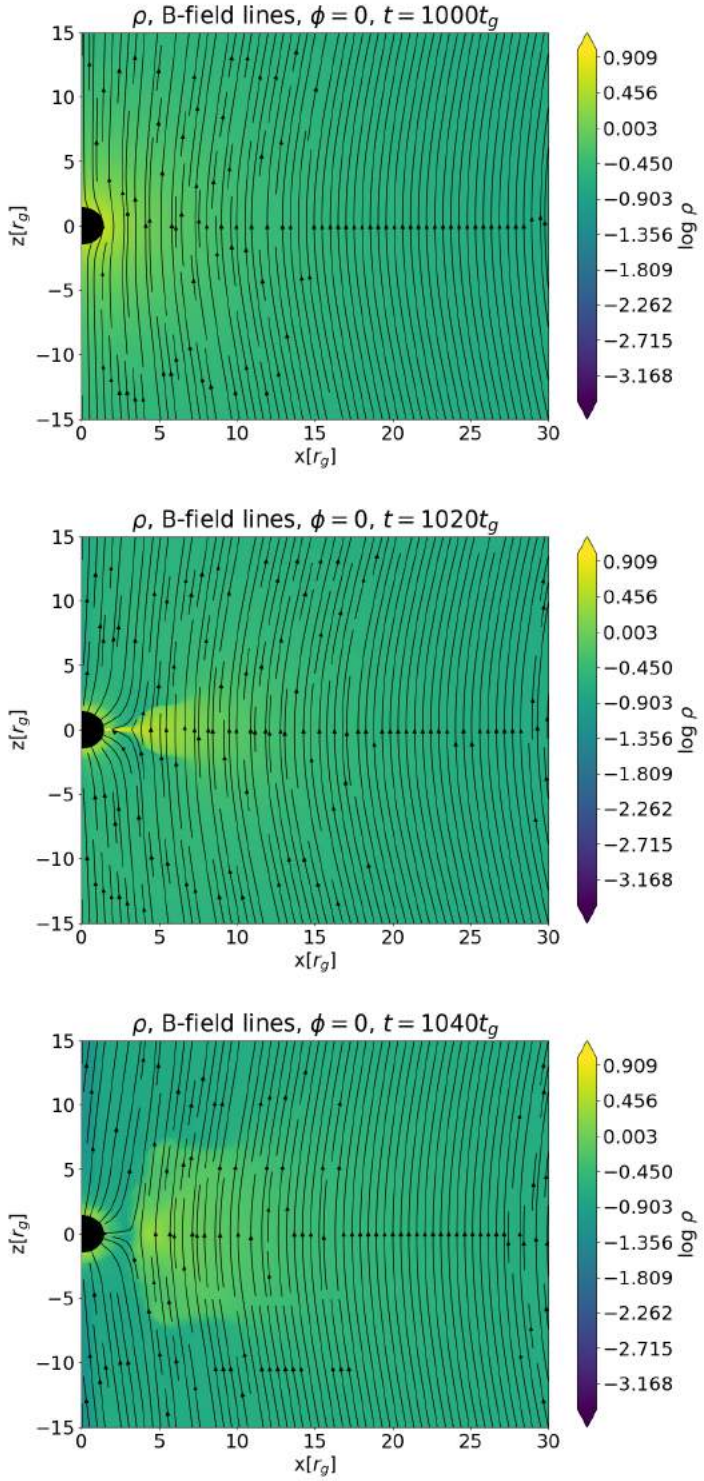

FIGURE 5.7: Plots of density and magnetic field from the 3D uniform field model b01.a90.3D at chosen time instances (poloidal slice)

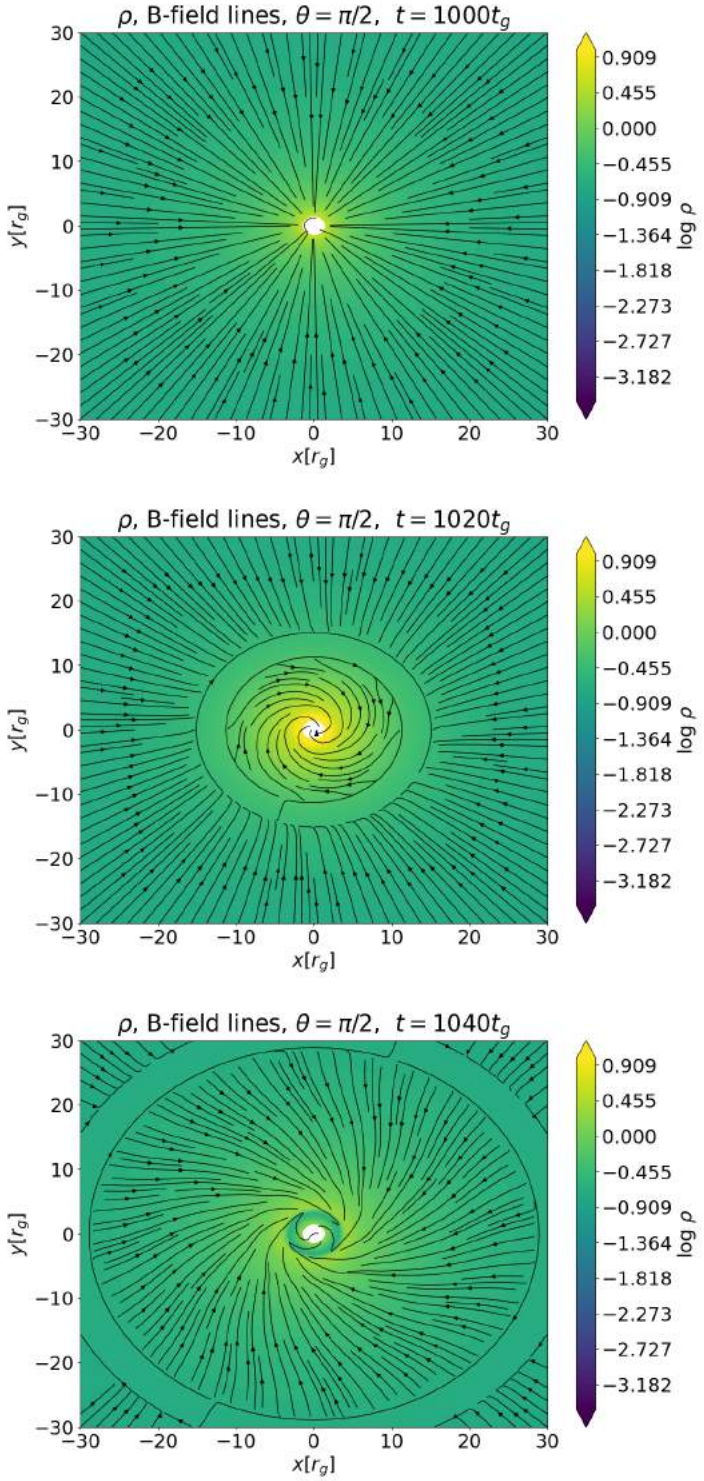

FIGURE 5.7: Plots of density and magnetic field from the 3D uniform field model b01.a90.3D at chosen time instances (contd.) (equatorial slice)

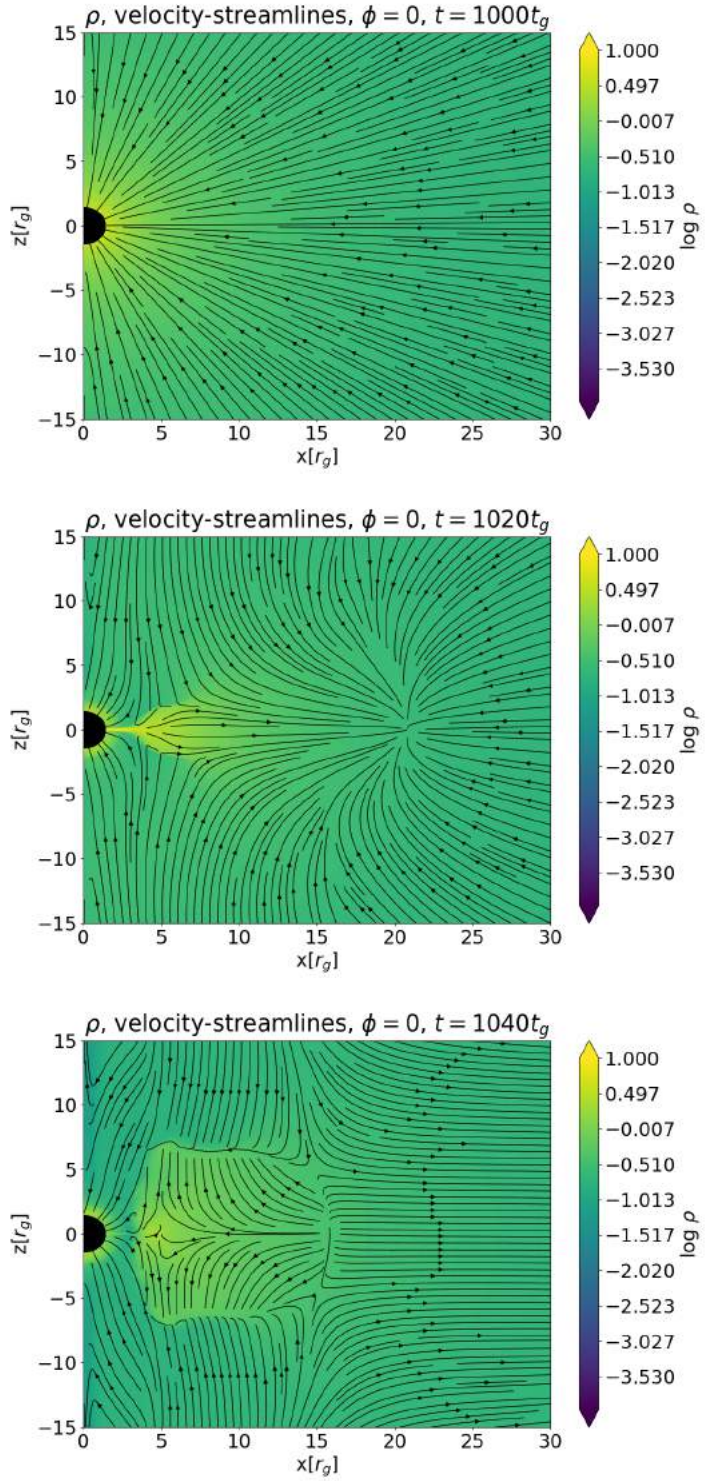

FIGURE 5.8: Plots of density and velocity stream lines from the 3D uniform field model b01.a90.3D at chosen time instances (poloidal slice)

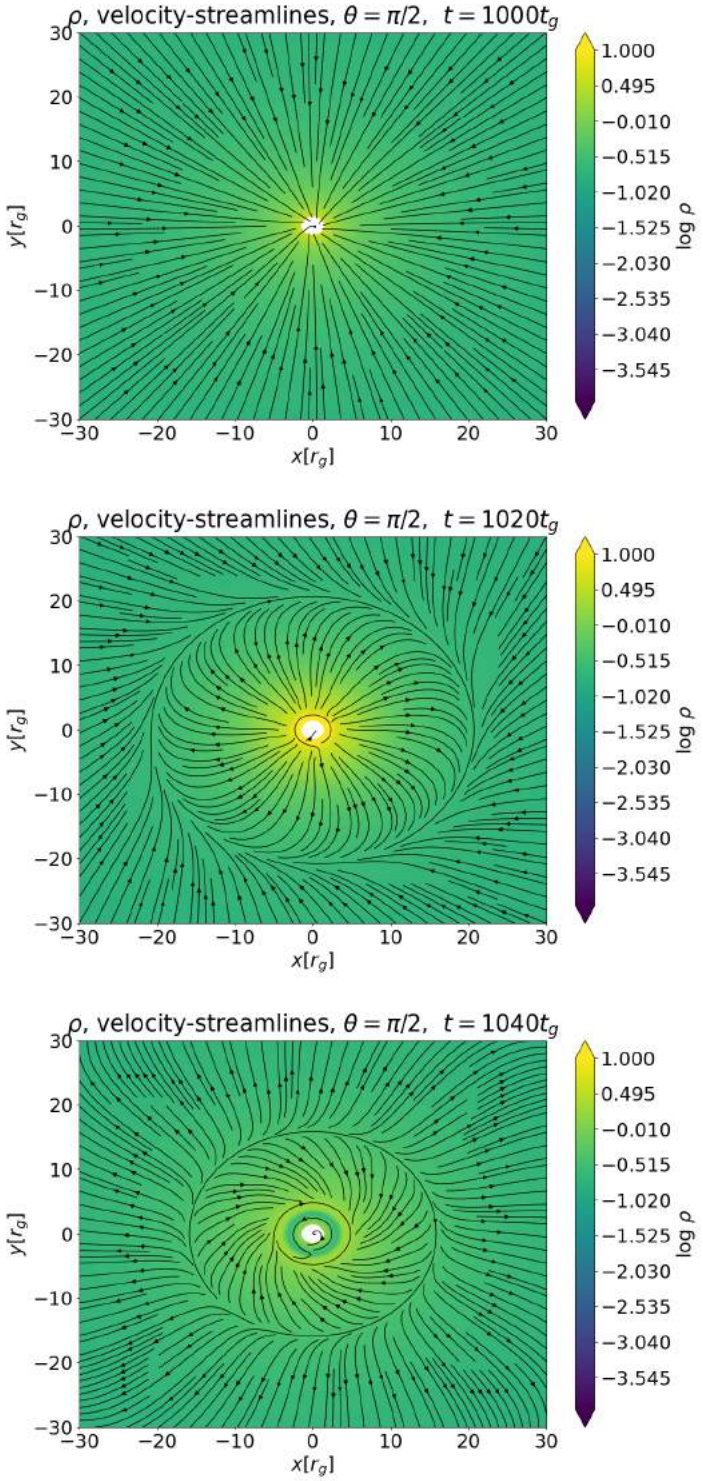

FIGURE 5.9: Plots of density and velocity stream lines from the 3D uniform field model b01.a90.3D at chosen time instances (contd.) (equatorial slice)

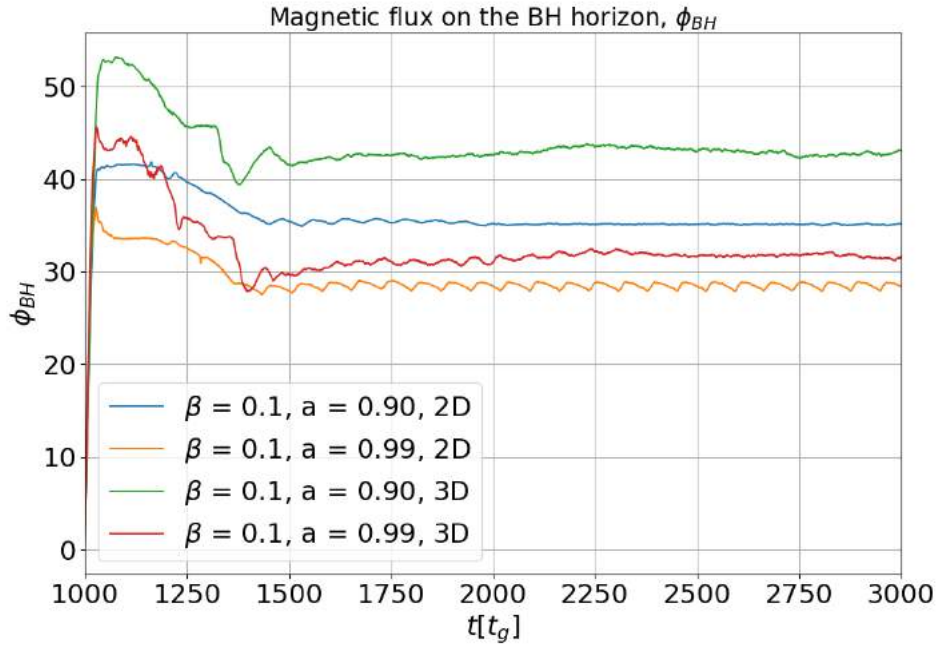

FIGURE 5.10: The evolution of magnetic flux on the black hole horizon with time for the 3D models with $\beta = 0.1$ and with different spin values from time $t = 1000\ t_g$ (values from 2D models are for comparison).

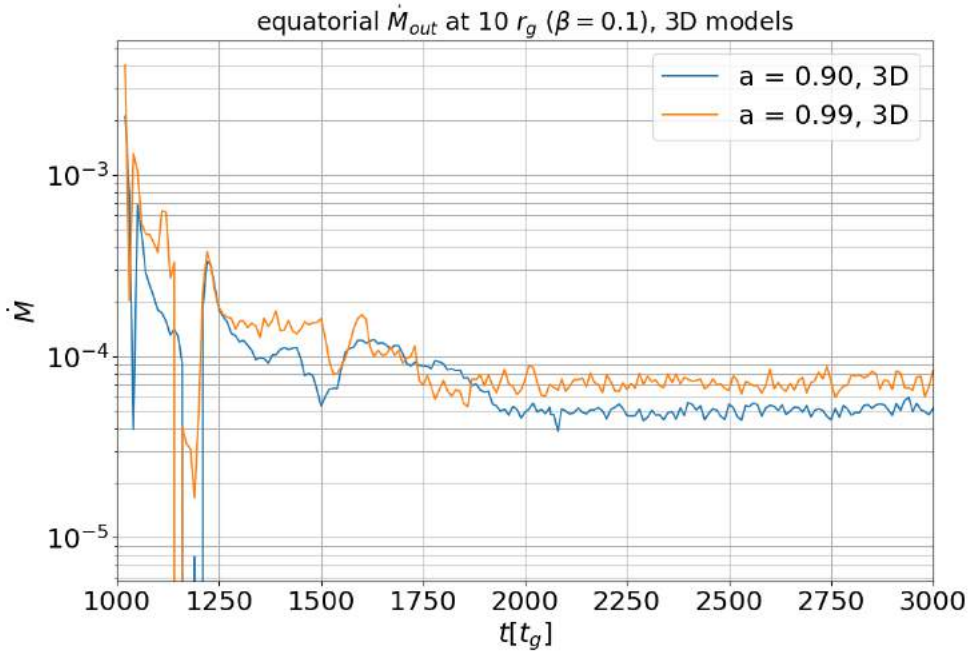

FIGURE 5.11: The equatorial mass outflow rate with time at 10 r_g, after the magnetic field is turned on, for the 3D models with $\beta = 0.1$ and different spin values

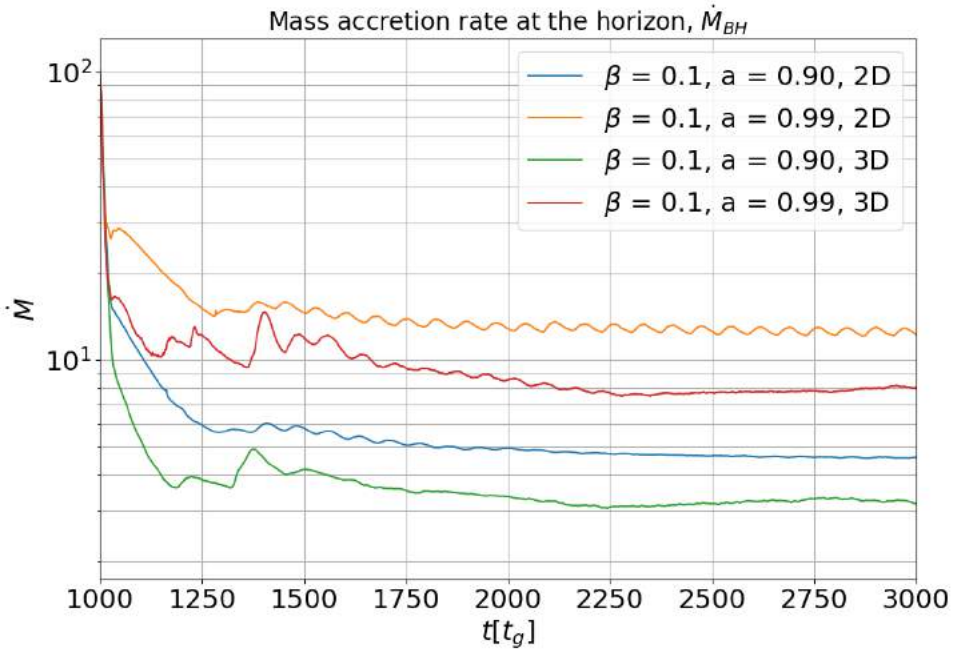

FIGURE 5.12: The evolution of inward mass accretion rate at the black hole horizon with time, after the magnetic field is turned on, for the 3D models with $\beta = 0.1$ and different spin values (values from 2D models are for comparison).

flows embedded in large scale poloidal magnetic fields with 3D GRMHD simulations for the case of rapidly spinning black holes. In their models, they found that the accretion flows initially needs to possess a specific angular momentum above a certain threshold in order to sustain a MAD state and to result in very powerful jets. Our models on the other hand seem to sustain a very large flux on the horizon even though the initial flows did not posses an angular momentum. They also note that accretion flows having initial specific angular momentum below their threshold also can launch episodic jets. Curd and Narayan, 2023 investigated MAD state with their GRRMHD simulations and those models resulted in relativistic jets. Their models showed significant variability in outgoing radiation which they attribute to episodes of magnetic flux eruptions.

5.4 Further investigations

For future work, we plan to investigate the effects of an asymptotically uniform magnetic field inclined with respect to the rotation axis of the black hole and evolve the non-axisymmetric 3D configuration. This is interesting as this will involve tangled magnetic field structures and the effect of this on the outflow rates and the inward accretion rate are to be investigated. When employed, we can investigate different angles between the black hole spin and the magnetic field direction and look further into their effect on the equatorial dynamics of accretion flows now governed by the magnetic reconnection-driven turbulence. Since we explore the regime of low-angular momentum accretion, especially focusing on the limiting case of zero angular momentum flows, the effects of magnetic field tilt can be studied better as opposed to the effects of angular momentum of the gas. It has been shown recently

by Ressler et al., 2021 that the jet direction in this case can fluctuate in time. Hence, periodic changes in synchrotron radiation as observed from our galaxy center Sgr A* may be investigated with such scenarios. We also plan to explore the influence of such a field and fluid geometry in the formation of magnetically dominated jets. We plan also to focus on highly magnetized models and investigate the relevance of such configurations on intermittent outflows observed in low-angular momentum accreting black hole sources.

Chapter 6

Summary and prospects

This thesis is a compendium of works exploring the features of black hole magnetospheres and magnetized jet launching from accreting black holes. In the introductory chapters, I summarize the essential basics of black hole accretion theory and the observed physical phenomena in which the theory is essential.

Relativistic jets are an interesting paradigm in high-energy astrophysics associated with a variety of sources ranging from neutron stars and stellar mass black holes to supermassive black hole sources. These jets are observed in GRBs and pulsars at the stellar mass scales, showing a wide variety of spatial structures - visible in terms of their opening angles and very fast (subsecond) variability in time. On the other hand, they are observed at much larger mass scales along with supermassive black holes in AGNs. Some of the largest and most active jets are produced by supermassive black holes residing at the center of active galaxies and extend to millions of parsecs in length. The reasons for the complex structure and variability in time of both these classes of jets are an area of active research. My research projects investigated the spatial structure and temporal variability properties of jets from accreting black hole sources at various mass scales. We employed computational methods and solved numerical equations pertaining to extreme accreting black hole environments and the associated jet base. We also compared the results from my numerical simulations with observational data and employed suitable models for explaining the physical properties of the jets we observe. The simulations were mainly done with the GRMHD code HARM and the additional modifications in the code for the systems we considered were done in consultation with my supervisor.

In the first project, we investigated the time variability of magnetized jets from accreting black holes with the HARM code. In this project, we have considered accreting black hole sources in general, spanning all the observed mass scales, and tried to investigate correlations between the jet properties and the characteristics of the central engine (Janiuk, James, and Palit, 2021). The central engine of all these sources consists of a black hole surrounded by an accretion disk. Observational studies have pointed towards a correlation between the jet Lorentz factor and their minimum variability timescale (MTS) initially for the case of GRBs (Sonbas et al., 2015) and later extended to blazars as well (Wu et al., 2016). On the other hand, the mechanisms behind the observed very fast variability, its correlation with the Lorentz factor, and the connection to the central engine of these sources are still a bit unclear. In this project, we investigated the connection of the variability timescales to the properties of the central engine which consists of an accretion disk and a Kerr black hole. We conducted 2D axisymmetric simulations of magnetized accretion disks around Kerr black holes for this investigation. We started with an equilibrium thick disk solution around a Kerr black hole, threaded by a poloidal magnetic field. This resulted in the development of magnetorotational instability and in turn accretion onto the black hole. Our models self-consistently resulted in nonuniform

jets, launched according to the Blandford-Znajek mechanism, which we analyzed in terms of jet energetics and time variability. We examined three different families of models and determined the idealized time-averaged jet Lorentz factor and its minimum variability timescale (MTS) for each one. Our study illustrated the relationships between jet properties and the characteristics of central engines in GRBs and blazars.

In the second project, we investigated the properties of GRB jets considering magnetically arrested disks as their central engines. This project extended the work done in the previous project to fully non-axisymmetric 3D simulations of GRB central engines (James, Janiuk, and Nouri, 2022). Many observational studies suggest the existence of structured jets in GRBs and such configurations are often taken into consideration to explain their complex variability in time (Margutti et al., 2018; Kathirgamaraju, Barniol Duran, and Giannios, 2018). It is also widely accepted that the emission we observe from both the classes of GRBs results from an accretion disk around a central compact object, which forms during the initial phases of the event (Gehrels, Ramirez-Ruiz, and Fox, 2009). Also, magnetically arrested accretion disks are nowadays considered to explain properties of accreting compact sources, more widely in the context of AGNs (Chael, Narayan, and Johnson, 2019; Dexter et al., 2020; Event Horizon Telescope Collaboration et al., 2021). In this work, we considered the magnetically arrested accretion disks for the central engines of GRBs and investigated how successfully they can explain the observed jet emission properties. We initialized the simulations with two different equilibrium disk solutions that are threaded by magnetic fields of different geometries depending on the central engines we considered. The models were set up in a way to achieve the magnetically arrested state rather fast, and we studied how this state affects the properties of the jets produced. We compared simulation results to the observed jet opening angles and variability time scales.

The final ongoing project investigates the effects of the accretion of large-scale magnetic fields to the black hole horizon (Chapter 5). The plasma in the vicinity of a black hole is attracted to it by the immense gravity and often results in an accretion flow sometimes accompanied by ejection. In this project, we model outflows driven by a large-scale magnetic field in the vicinity of a rotating black hole. We initialize our simulations with an initially spherical accretion profile and a uniform magnetic field in the Kerr geometry. The magnetic field lines frozen into the plasma are rapidly accreted onto the black hole as the simulations begin, canceling the initial Meissner-like expulsion due to the rapid rotation of the black hole. We notice the magnetic reconnection events near the equatorial plane which drives an outflow in our models. We also notice repetitive fluctuations in the accretion rate in some of our models and sometimes the emergence of velocity vortices in the accretion flow, found by the patterns of velocity streamlines. Both of these phenomena can affect the rate of outflows. We also plan to investigate non-axisymmetric magnetic field configurations, specifically asymptotically uniform fields inclined with the rotation axis of the black holes and study their effect on the rate of outflows. A manuscript from this work is also now under preparation at the time of writing this thesis.

In summary, this thesis explores the widely known jet paradigm in the domain of relativistic astrophysics and makes contributions to it by giving a clearer explanation for the observed time variability. Also, the spatial structure of the base of the jets, especially the GRB jets - which we cannot resolve with the present-day technologies, is explored in detail in terms of jet opening angle and its non-axisymmetric evolution. Thus this thesis provides new insights into the disk, black hole, and jet interconnection, as predicted by the Blandford-Znajek mechanism. In addition, it

also explores the evolution of black hole magnetospheres and predicts properties of outflows, based on the assumed models, which can be relevant in the regime of accretion onto supermassive black holes.

Bibliography

Abbott, B. P. et al. (Oct. 2017). "Gravitational Waves and Gamma-Rays from a Binary Neutron Star Merger: GW170817 and GRB 170817A". In: ApJ 848.2, L13, p. L13. DOI: 10.3847/2041-8213/aa920c. arXiv: 1710.05834 [astro-ph.HE].

Abramowicz, M., M. Jaroszynski, and M. Sikora (Feb. 1978). "Relativistic, accreting disks." In: A&A 63, pp. 221–224.

Abramowicz, Marek A. and P. Chris Fragile (Jan. 2013). "Foundations of Black Hole Accretion Disk Theory". In: *Living Reviews in Relativity* 16.1, 1, p. 1. DOI: 10.12942/lrr-2013-1. arXiv: 1104.5499 [astro-ph.HE].

Anderson, Wilhelm (Nov. 1929). "Über die Grenzdichte der Materie und der Energie". In: *Zeitschrift fur Physik* 56.11-12, pp. 851–856. DOI: 10.1007/BF01340146.

Armitage, Philip J. (Jan. 2022). "Lecture notes on accretion disk physics". In: *arXiv e-prints*, arXiv:2201.07262, arXiv:2201.07262. DOI: 10.48550/arXiv.2201.07262. arXiv: 2201.07262 [astro-ph.HE].

Balbus, Steven A. and John F. Hawley (July 1991). "A Powerful Local Shear Instability in Weakly Magnetized Disks. I. Linear Analysis". In: ApJ 376, p. 214. DOI: 10.1086/170270.

Balbus, Steven A. and John F. Hawley (Jan. 1998). "Instability, turbulence, and enhanced transport in accretion disks". In: *Reviews of Modern Physics* 70.1, pp. 1–53. DOI: 10.1103/RevModPhys.70.1.

Bambi, Cosimo (June 2018). "Astrophysical Black Holes: A Compact Pedagogical Review". In: *Annalen der Physik* 530.6, p. 1700430. DOI: 10.1002/andp.201700430. arXiv: 1711.10256 [gr-qc].

Bardeen, James M. (Apr. 1970). "Kerr Metric Black Holes". In: Nature 226.5240, pp. 64–65. DOI: 10.1038/226064a0.

Bardeen, James M., William H. Press, and Saul A. Teukolsky (Dec. 1972). "Rotating Black Holes: Locally Nonrotating Frames, Energy Extraction, and Scalar Synchrotron Radiation". In: ApJ 178, pp. 347–370. DOI: 10.1086/151796.

Bicak, J. and V. Janis (Feb. 1985). "Magnetic fluxes across black holes". In: MNRAS 212, pp. 899–915. DOI: 10.1093/mnras/212.4.899.

Bisnovatyi-Kogan, G. S. and A. A. Ruzmaikin (May 1974). "The Accretion of Matter by a Collapsing Star in the Presence of a Magnetic Field". In: Ap&SS 28.1, pp. 45–59. DOI: 10.1007/BF00642237.

Blandford, R. D. and D. G. Payne (June 1982). "Hydromagnetic flows from accretion disks and the production of radio jets." In: MNRAS 199, pp. 883–903. DOI: 10.1093/mnras/199.4.883.

Blandford, R. D. and R. L. Znajek (May 1977). "Electromagnetic extraction of energy from Kerr black holes." In: MNRAS 179, pp. 433–456. DOI: 10.1093/mnras/179.3.433.

Blandford, Roger and Noémie Globus (Aug. 2022). "Ergomagnetosphere, ejection disc, magnetopause in M87 - I. Global flow of mass, angular momentum, energy, and current". In: MNRAS 514.4, pp. 5141–5158. DOI: 10.1093/mnras/stac1682. arXiv: 2204.11995 [astro-ph.HE].

Boehle, A. et al. (Oct. 2016). "An Improved Distance and Mass Estimate for Sgr A* from a Multistar Orbit Analysis". In: ApJ 830.1, 17, p. 17. DOI: 10.3847/0004-637X/830/1/17. arXiv: 1607.05726 [astro-ph.GA].

Bolton, C. T. (Feb. 1972). "Identification of Cygnus X-1 with HDE 226868". In: Nature 235.5336, pp. 271–273. DOI: 10.1038/235271b0.

Bondi, H. (Jan. 1952). "On spherically symmetrical accretion". In: MNRAS 112, p. 195. DOI: 10.1093/mnras/112.2.195.

Bowyer, S. et al. (Jan. 1965). "Cosmic X-ray Sources". In: *Science* 147.3656, pp. 394–398. DOI: 10.1126/science.147.3656.394.

Boyer, Robert H. and Richard W. Lindquist (Feb. 1967). "Maximal Analytic Extension of the Kerr Metric". In: *Journal of Mathematical Physics* 8.2, pp. 265–281. DOI: 10.1063/1.1705193.

Carter, Brandon (Oct. 1968). "Global Structure of the Kerr Family of Gravitational Fields". In: *Physical Review* 174.5, pp. 1559–1571. DOI: 10.1103/PhysRev.174.1559.

Chael, Andrew, Ramesh Narayan, and Michael D. Johnson (June 2019). "Two-temperature, Magnetically Arrested Disc simulations of the jet from the supermassive black hole in M87". In: MNRAS 486.2, pp. 2873–2895. DOI: 10.1093/mnras/stz988. arXiv: 1810.01983 [astro-ph.HE].

Chakrabarti, S. K. (Jan. 1985). "The natural angular momentum distribution in the study of thick disks around black holes". In: ApJ 288, pp. 1–6. DOI: 10.1086/162755.

Chandrasekhar, S. (July 1931). "The Maximum Mass of Ideal White Dwarfs". In: ApJ 74, p. 81. DOI: 10.1086/143324.

Chandrasekhar, S. (1961). *Hydrodynamic and hydromagnetic stability*.

Chen, Francis F. (2016). *Introduction to Plasma Physics and Controlled Fusion*. DOI: 10.1007/978-3-319-22309-4.

Chen, Xingming et al. (Apr. 1995). "Unified Description of Accretion Flows around Black Holes". In: ApJ 443, p. L61. DOI: 10.1086/187836. arXiv: astro-ph/9502015 [astro-ph].

Chiuderi, C. and M. Velli (2015). *Basics of Plasma Astrophysics*.

Courant, R., K. Friedrichs, and H. Lewy (Mar. 1967). "On the Partial Difference Equations of Mathematical Physics". In: *IBM Journal of Research and Development* 11, pp. 215–234. DOI: 10.1147/rd.112.0215.

Crinquand, Benjamin et al. (Nov. 2022). "Synthetic Images of Magnetospheric Reconnection-Powered Radiation around Supermassive Black Holes". In: Phys. Rev. Lett. 129.20, 205101, p. 205101. DOI: 10.1103/PhysRevLett.129.205101. arXiv: 2202.04472 [astro-ph.HE].

Cruz-Osorio, Alejandro et al. (Jan. 2022). "State-of-the-art energetic and morphological modelling of the launching site of the M87 jet". In: *Nature Astronomy* 6, pp. 103–108. DOI: 10.1038/s41550-021-01506-w. arXiv: 2111.02517 [astro-ph.HE].

Curd, Brandon and Ramesh Narayan (Jan. 2023). "GRRMHD simulations of MAD accretion discs declining from super-Eddington to sub-Eddington accretion rates". In: MNRAS 518.3, pp. 3441–3461. DOI: 10.1093/mnras/stac3330. arXiv: 2209.12081 [astro-ph.HE].

Czerny, Bozena et al. (Nov. 2016). "A Test of the Formation Mechanism of the Broad Line Region in Active Galactic Nuclei". In: ApJ 832.1, 15, p. 15. DOI: 10.3847/0004-637X/832/1/15. arXiv: 1610.00420 [astro-ph.GA].

De Villiers, Jean-Pierre and John F. Hawley (May 2003). "A Numerical Method for General Relativistic Magnetohydrodynamics". In: ApJ 589.1, pp. 458–480. DOI: 10.1086/373949. arXiv: astro-ph/0210518 [astro-ph].

Dexter, J. et al. (Oct. 2020). "Sgr A* near-infrared flares from reconnection events in a magnetically arrested disc". In: MNRAS 497.4, pp. 4999–5007. DOI: 10.1093/mnras/staa2288. arXiv: 2006.03657 [astro-ph.HE].

Duque, Raphaël (Sept. 2021). "Compact object coalescences and gamma-ray bursts in the gravitational-wave era". PhD thesis. Sorbonne University.

Eckart, A. and R. Genzel (Jan. 1997). "Stellar proper motions in the central 0.1 PC of the Galaxy". In: MNRAS 284.3, pp. 576–598. DOI: 10.1093/mnras/284.3.576.

Eichler, David et al. (July 1989). "Nucleosynthesis, neutrino bursts and γ-rays from coalescing neutron stars". In: Nature 340.6229, pp. 126–128. DOI: 10.1038/340126a0.

Einstein, A. (Jan. 1916). "Die Grundlage der allgemeinen Relativitätstheorie". In: *Annalen der Physik* 354.7, pp. 769–822. DOI: 10.1002/andp.19163540702.

El Mellah, I. et al. (July 2022). "Spinning black holes magnetically connected to a Keplerian disk. Magnetosphere, reconnection sheet, particle acceleration, and coronal heating". In: A&A 663, A169, A169. DOI: 10.1051/0004-6361/202142847. arXiv: 2112.03933 [astro-ph.HE].

Escrivà, Albert, Florian Kuhnel, and Yuichiro Tada (Nov. 2022). "Primordial Black Holes". In: *arXiv e-prints*, arXiv:2211.05767, arXiv:2211.05767. DOI: 10.48550/arXiv.2211.05767. arXiv: 2211.05767 [astro-ph.CO].

Event Horizon Telescope Collaboration et al. (Apr. 2019). "First M87 Event Horizon Telescope Results. VI. The Shadow and Mass of the Central Black Hole". In: ApJ 875.1, L6, p. L6. DOI: 10.3847/2041-8213/ab1141. arXiv: 1906.11243 [astro-ph.GA].

Event Horizon Telescope Collaboration et al. (Mar. 2021). "First M87 Event Horizon Telescope Results. VIII. Magnetic Field Structure near The Event Horizon". In: ApJ 910.1, L13, p. L13. DOI: 10.3847/2041-8213/abe4de. arXiv: 2105.01173 [astro-ph.HE].

Event Horizon Telescope Collaboration et al. (May 2022a). "First Sagittarius A* Event Horizon Telescope Results. V. Testing Astrophysical Models of the Galactic Center Black Hole". In: ApJ 930.2, L16, p. L16. DOI: 10.3847/2041-8213/ac6672.

Event Horizon Telescope Collaboration et al. (May 2022b). "First Sagittarius A* Event Horizon Telescope Results. I. The Shadow of the Supermassive Black Hole in the Center of the Milky Way". In: ApJ 930.2, L12, p. L12. DOI: 10.3847/2041-8213/ac6674.

Fan, Xiaohui et al. (Jan. 2001). "High-Redshift Quasars Found in Sloan Digital Sky Survey Commissioning Data. IV. Luminosity Function from the Fall Equatorial Stripe Sample". In: AJ 121.1, pp. 54–65. DOI: 10.1086/318033. arXiv: astro-ph/0008123 [astro-ph].

Fath, Edward Arthur (Jan. 1909). "The spectra of some spiral nebulae and globular star clusters". In: *Lick Observatory Bulletin* 149, pp. 71–77. DOI: 10.5479/ADS/bib/1909LicOB.5.71F.

Fender, Rob and Elena Gallo (Sept. 2014). "An Overview of Jets and Outflows in Stellar Mass Black Holes". In: Space Sci. Rev. 183.1-4, pp. 323–337. DOI: 10.1007/s11214-014-0069-z. arXiv: 1407.3674 [astro-ph.HE].

Finkelstein, David (May 1958). "Past-Future Asymmetry of the Gravitational Field of a Point Particle". In: *Physical Review* 110.4, pp. 965–967. DOI: 10.1103/PhysRev.110.965.

Fishbone, L. G. and V. Moncrief (Aug. 1976). "Relativistic fluid disks in orbit around Kerr black holes." In: ApJ 207, pp. 962–976. DOI: 10.1086/154565.

Fong, W. and E. Berger (Oct. 2013). "The Locations of Short Gamma-Ray Bursts as Evidence for Compact Object Binary Progenitors". In: ApJ 776.1, 18, p. 18. DOI: 10.1088/0004-637X/776/1/18. arXiv: 1307.0819 [astro-ph.HE].

Font, José A. and Frédéric Daigne (Aug. 2002). "The runaway instability of thick discs around black holes - I. The constant angular momentum case". In: MNRAS 334.2, pp. 383–400. DOI: 10.1046/j.1365-8711.2002.05515.x. arXiv: astro-ph/0203403 [astro-ph].

Frank, Juhan, Andrew King, and Derek J. Raine (2002). *Accretion Power in Astrophysics: Third Edition*.

Frank-Kamenetskii, D. A. (1972). "Interchange or Flute Instabilities". In: *Plasma: The Fourth State of Matter*. London: Macmillan Education UK, pp. 98–100. ISBN: 978-1-349-01552-8. DOI: 10.1007/978-1-349-01552-8_32. URL: https://doi.org/10.1007/978-1-349-01552-8_32.

Fryer, Chris L. and Aimee Hungerford (2005). "Neutron Star Formation". In: *The Electromagnetic Spectrum of Neutron Stars*. Ed. by Altan Baykal et al. Dordrecht: Springer Netherlands, pp. 3–14. ISBN: 978-1-4020-3861-7.

Galama, T. J. et al. (Oct. 1998). "An unusual supernova in the error box of the γ-ray burst of 25 April 1998". In: Nature 395.6703, pp. 670–672. DOI: 10.1038/27150. arXiv: astro-ph/9806175 [astro-ph].

Gammie, Charles F., Jonathan C. McKinney, and Gábor Tóth (May 2003). "HARM: A Numerical Scheme for General Relativistic Magnetohydrodynamics". In: ApJ 589.1, pp. 444–457. DOI: 10.1086/374594. arXiv: astro-ph/0301509 [astro-ph].

Gehrels, N., E. Ramirez-Ruiz, and D. B. Fox (Sept. 2009). "Gamma-Ray Bursts in the Swift Era". In: ARA&A 47.1, pp. 567–617. DOI: 10.1146/annurev.astro.46.060407.145147. arXiv: 0909.1531 [astro-ph.HE].

Ghez, A. M. et al. (Dec. 1998). "High Proper-Motion Stars in the Vicinity of Sagittarius A*: Evidence for a Supermassive Black Hole at the Center of Our Galaxy". In: ApJ 509.2, pp. 678–686. DOI: 10.1086/306528. arXiv: astro-ph/9807210 [astro-ph].

Ghosh, Dip (2021). *Rayleigh-Taylor instability in Geodynamics*. URL: https://blogs.egu.eu/divisions/gd/2021/02/17/rayleigh-taylor-instability-in-geodynamics/ (visited on 06/11/2023).

Gourgoulhon, Eric (Mar. 2007). "3+1 Formalism and Bases of Numerical Relativity". In: *arXiv e-prints*, gr-qc/0703035, gr–qc/0703035. DOI: 10.48550/arXiv.gr-qc/0703035. arXiv: gr-qc/0703035 [gr-qc].

Greene, Jenny E., Jay Strader, and Luis C. Ho (Aug. 2020). "Intermediate-Mass Black Holes". In: ARA&A 58, pp. 257–312. DOI: 10.1146/annurev-astro-032620-021835. arXiv: 1911.09678 [astro-ph.GA].

Harten, Amiram, Peter D. Lax, and Bram van Leer (1983). "On Upstream Differencing and Godunov-Type Schemes for Hyperbolic Conservation Laws". In: *SIAM Review* 25.1, pp. 35–61. DOI: 10.1137/1025002. eprint: https://doi.org/10.1137/1025002. URL: https://doi.org/10.1137/1025002.

Hartle, J. B. (Jan. 1978). "Bounds on the mass and moment of inertia of nonrotating neutron stars." In: Phys. Rep. 46.6, pp. 201–247. DOI: 10.1016/0370-1573(78)90140-0.

Hawley, John F., Steven A. Balbus, and Wayne F. Winters (June 1999). "Local Hydrodynamic Stability of Accretion Disks". In: ApJ 518.1, pp. 394–404. DOI: 10.1086/307282. arXiv: astro-ph/9811057 [astro-ph].

Hirose, Shigenobu, Julian H. Krolik, and Omer Blaes (Jan. 2009). "Radiation-Dominated Disks are Thermally Stable". In: ApJ 691.1, pp. 16–31. DOI: 10.1088/0004-637X/691/1/16. arXiv: 0809.1708 [astro-ph].

Hjorth, Jens et al. (June 2003). "A very energetic supernova associated with the γ-ray burst of 29 March 2003". In: Nature 423.6942, pp. 847–850. DOI: 10.1038/nature01750. arXiv: astro-ph/0306347 [astro-ph].

Hoormann, J. K. et al. (Aug. 2019). "C IV black hole mass measurements with the Australian Dark Energy Survey (OzDES)". In: MNRAS 487.3, pp. 3650–3663. DOI: 10.1093/mnras/stz1539. arXiv: 1902.04206 [astro-ph.GA].

Igumenshchev, Igor V. (Apr. 2008). "Magnetically Arrested Disks and the Origin of Poynting Jets: A Numerical Study". In: ApJ 677.1, pp. 317–326. DOI: 10.1086/529025. arXiv: 0711.4391 [astro-ph].

James, B. and A. Janiuk (2022). "Numerical Study of Magnetically Dominated Jets from Accreting Black Hole Sources". In: *Acta Phys. Polon. Supp.* 15.1, p. 1. DOI: 10.5506/APhysPolBSupp.15.1-A6.

James, Bestin, Agnieszka Janiuk, and Fatemeh Hossein Nouri (Aug. 2022). "Modeling the Gamma-Ray Burst Jet Properties with 3D General Relativistic Simulations of Magnetically Arrested Accretion Flows". In: ApJ 935.2, 176, p. 176. DOI: 10.3847/1538-4357/ac81b7. arXiv: 2204.01515 [astro-ph.HE].

Janiuk, A., B. James, and K. Sapountzis (Mar. 2021). "Cosmic Gamma Ray Bursts". In: *Acta Physica Polonica A* 139.3, pp. 273–276. DOI: 10.12693/APhysPolA.139.273. arXiv: 2101.11880 [astro-ph.HE].

Janiuk, A. et al. (Dec. 2020). "Multi-messenger signals from short gamma ray bursts". In: *Multifrequency Behaviour of High Energy Cosmic Sources - XIII. 3-8 June 2019. Palermo*, 59, p. 59. DOI: 10.22323/1.362.0059. arXiv: 1911.05364 [astro-ph.HE].

Janiuk, Agnieszka (Mar. 2017). "Microphysics in the Gamma-Ray Burst Central Engine". In: ApJ 837.1, 39, p. 39. DOI: 10.3847/1538-4357/aa5f16. arXiv: 1609.09361 [astro-ph.HE].

Janiuk, Agnieszka and Bestin James (Dec. 2022). "Magnetically arrested accretion disks launching structured jets in application to GRB and AGN engines". In: A&A 668, A66, A66. DOI: 10.1051/0004-6361/202244196.

Janiuk, Agnieszka, Bestin James, and Ishika Palit (Aug. 2021). "Variability of Magnetically Dominated Jets from Accreting Black Holes". In: ApJ 917.2, 102, p. 102. DOI: 10.3847/1538-4357/ac0624. arXiv: 2105.13624 [astro-ph.HE].

Janiuk, Agnieszka et al. (June 2018). "Numerical Simulations of Black Hole Accretion Flows". In: *Supercomputing Frontiers and Innovations* 5.2, pp. 86–102. DOI: 10.14529/jsfi180208. URL: https://superfri.org/index.php/superfri/article/view/177.

Kathirgamaraju, Adithan, Rodolfo Barniol Duran, and Dimitrios Giannios (Jan. 2018). "Off-axis short GRBs from structured jets as counterparts to GW events". In: MNRAS 473.1, pp. L121–L125. DOI: 10.1093/mnrasl/slx175. arXiv: 1708.07488 [astro-ph.HE].

Kerr, Roy P. (Sept. 1963). "Gravitational Field of a Spinning Mass as an Example of Algebraically Special Metrics". In: Phys. Rev. Lett. 11.5, pp. 237–238. DOI: 10.1103/PhysRevLett.11.237.

King, A. R., J. P. Lasota, and W. Kundt (Nov. 1975). "Black holes and magnetic fields". In: *Phys. Rev. D* 12 (10), pp. 3037–3042. DOI: 10.1103/PhysRevD.12.3037. URL: https://link.aps.org/doi/10.1103/PhysRevD.12.3037.

King, A. R., J. E. Pringle, and M. Livio (Apr. 2007). "Accretion disc viscosity: how big is alpha?" In: MNRAS 376.4, pp. 1740–1746. DOI: 10.1111/j.1365-2966.2007.11556.x. arXiv: astro-ph/0701803 [astro-ph].

Klebesadel, Ray W., Ian B. Strong, and Roy A. Olson (June 1973). "Observations of Gamma-Ray Bursts of Cosmic Origin". In: ApJ 182, p. L85. DOI: 10.1086/181225.

Kološ, Martin and Agnieszka Janiuk (Apr. 2020). "Simulations of black hole accretion torus in various magnetic field configurations". In: *arXiv e-prints*, arXiv:2004.07535, arXiv:2004.07535. DOI: 10.48550/arXiv.2004.07535. arXiv: 2004.07535 [astro-ph.HE].

Komissarov, S. S. and Jonathan C. McKinney (May 2007). "The 'Meissner effect' and the Blandford-Znajek mechanism in conductive black hole magnetospheres". In: MNRAS 377.1, pp. L49–L53. DOI: 10.1111/j.1745-3933.2007.00301.x. arXiv: astro-ph/0702269 [astro-ph].

Kouveliotou, Chryssa et al. (Aug. 1993). "Identification of Two Classes of Gamma-Ray Bursts". In: ApJ 413, p. L101. DOI: 10.1086/186969.

Król, Dominika Ł. and Agnieszka Janiuk (May 2021). "Accretion-induced Black Hole Spin-up Revised by Numerical General Relativistic MHD". In: ApJ 912.2, 132, p. 132. DOI: 10.3847/1538-4357/abf245. arXiv: 2104.00741 [astro-ph.HE].

Krolik, Julian H. (1999). *Active galactic nuclei : from the central black hole to the galactic environment*.

Kruskal, M. and M. Schwarzschild (May 1954). "Some Instabilities of a Completely Ionized Plasma". In: *Proceedings of the Royal Society of London Series A* 223.1154, pp. 348–360. DOI: 10.1098/rspa.1954.0120.

Kwan, Tom M., Lixin Dai, and Alexander Tchekhovskoy (Nov. 2022). "The Effects of Gas Angular Momentum on Forming Magnetically Arrested Disks and Launching Powerful Jets". In: *arXiv e-prints*, arXiv:2211.12726, arXiv:2211.12726. DOI: 10.48550/arXiv.2211.12726. arXiv: 2211.12726 [astro-ph.HE].

Kwan, Tom M., Lixin Dai, and Alexander Tchekhovskoy (Apr. 2023). "The Effects of Gas Angular Momentum on the Formation of Magnetically Arrested Disks and the Launching of Powerful Jets". In: ApJ 946.2, L42, p. L42. DOI: 10.3847/2041-8213/acc334. arXiv: 2211.12726 [astro-ph.HE].

Le Floc'h, E. et al. (Mar. 2003). "Are the hosts of gamma-ray bursts sub-luminous and blue galaxies?" In: A&A 400, pp. 499–510. DOI: 10.1051/0004-6361:20030001. arXiv: astro-ph/0301149 [astro-ph].

Lin, D. N. C. and J. Papaloizou (Apr. 1980). "On the structure and evolution of the primordial solar nebula". In: MNRAS 191, pp. 37–48. DOI: 10.1093/mnras/191.1.37.

Lynden-Bell, D. and J. E. Pringle (Sept. 1974). "The evolution of viscous discs and the origin of the nebular variables." In: MNRAS 168, pp. 603–637. DOI: 10.1093/mnras/168.3.603.

Mallozzi, Robert S. (2018). *Gamma-Ray Astrophysics NSSTC Website*. URL: https://gammaray.nsstc.nasa.gov/batse/grb/lightcurve/ (visited on 06/11/2023).

Margutti, R. et al. (Mar. 2018). "The Binary Neutron Star Event LIGO/Virgo GW170817 160 Days after Merger: Synchrotron Emission across the Electromagnetic Spectrum". In: ApJ 856.1, L18, p. L18. DOI: 10.3847/2041-8213/aab2ad. arXiv: 1801.03531 [astro-ph.HE].

Michell, John (1784). "VII. On the means of discovering the distance, magnitude, &c. of the fixed stars, in consequence of the diminution of the velocity of their light, in case such a diminution should be found to take place in any of them, and such other data should be procured from observations, as would be farther necessary for that purpose. By the Rev. John Michell, B.D. F.R.S. In a letter to Henry Cavendish, Esq. F.R.S. and A.S". In: *Philosophical Transactions of the Royal Society of London* 74, pp. 35–57. DOI: 10.1098/rstl.1784.0008. URL: https://royalsocietypublishing.org/doi/abs/10.1098/rstl.1784.0008.

Misner, Charles W., Kip S. Thorne, and John Archibald Wheeler (1973). *Gravitation*.

Murguia-Berthier, Ariadna et al. (Oct. 2020). "On the Maximum Stellar Rotation to form a Black Hole without an Accompanying Luminous Transient". In: ApJ 901.2, L24, p. L24. DOI: 10.3847/2041-8213/abb818. arXiv: 2005.10212 [astro-ph.HE].

Narayan, Ramesh, Igor V. Igumenshchev, and Marek A. Abramowicz (Dec. 2003). "Magnetically Arrested Disk: an Energetically Efficient Accretion Flow". In: PASJ 55, pp. L69–L72. DOI: 10.1093/pasj/55.6.L69. arXiv: astro-ph/0305029 [astro-ph].

Newman, E. T. et al. (June 1965). "Metric of a Rotating, Charged Mass". In: *Journal of Mathematical Physics* 6.6, pp. 918–919. DOI: 10.1063/1.1704351.

Noble, Scott C. et al. (Apr. 2006). "Primitive Variable Solvers for Conservative General Relativistic Magnetohydrodynamics". In: ApJ 641.1, pp. 626–637. DOI: 10.1086/500349. arXiv: astro-ph/0512420 [astro-ph].

Nordström, G. (Jan. 1918). "On the Energy of the Gravitation field in Einstein's Theory". In: *Koninklijke Nederlandse Akademie van Wetenschappen Proceedings Series B Physical Sciences* 20, pp. 1238–1245.

Norris, J. P. et al. (Mar. 1984). "Frequency of fast, narrow γ-ray bursts". In: Nature 308.5958, pp. 434–435. DOI: 10.1038/308434a0.

Nouri, Fatemeh Hossein, Agnieszka Janiuk, and Małgorzata Przerwa (Feb. 2023). "Studying Postmerger Outflows from Magnetized-neutrino-cooled Accretion Disks". In: ApJ 944.2, 220, p. 220. DOI: 10.3847/1538-4357/acafe2. arXiv: 2212.05628 [astro-ph.HE].

Oppenheimer, J. R. and G. M. Volkoff (Feb. 1939). "On Massive Neutron Cores". In: *Physical Review* 55.4, pp. 374–381. DOI: 10.1103/PhysRev.55.374.

Paczynski, B. (Sept. 1986). "Gamma-ray bursters at cosmological distances". In: ApJ 308, pp. L43–L46. DOI: 10.1086/184740.

Paczynski, B. and M. A. Abramowicz (Feb. 1982). "A model of a thick disk with equatorial accretion". In: ApJ 253, pp. 897–907. DOI: 10.1086/159689.

Paczyński, Bohdan (Feb. 1998). "Are Gamma-Ray Bursts in Star-Forming Regions?" In: ApJ 494.1, pp. L45–L48. DOI: 10.1086/311148. arXiv: astro-ph/9710086 [astro-ph].

Paczyńsky, B. and P. J. Wiita (Aug. 1980). "Thick Accretion Disks and Supercritical Luminosities". In: A&A 88, p. 23.

Padovani, P. et al. (Aug. 2017). "Active galactic nuclei: what's in a name?" In: A&A Rev. 25.1, 2, p. 2. DOI: 10.1007/s00159-017-0102-9. arXiv: 1707.07134 [astro-ph.GA].

Padovani, Paolo (Aug. 2017). "On the two main classes of active galactic nuclei". In: *Nature Astronomy* 1, 0194, p. 0194. DOI: 10.1038/s41550-017-0194. arXiv: 1707.08069 [astro-ph.GA].

Papadopoulos, Philippos and Jose A. Font (Dec. 1999). "Analysis of relativistic hydrodynamics in conservation form". In: *arXiv e-prints*, gr-qc/9912054, gr-qc/9912054. DOI: 10.48550/arXiv.gr-qc/9912054. arXiv: gr-qc/9912054 [astro-ph].

Penrose, R. and R. M. Floyd (Feb. 1971). "Extraction of Rotational Energy from a Black Hole". In: *Nature Physical Science* 229.6, pp. 177–179. DOI: 10.1038/physci229177a0.

Piran, Tsvi (Oct. 2004). "The physics of gamma-ray bursts". In: *Reviews of Modern Physics* 76.4, pp. 1143–1210. DOI: 10.1103/RevModPhys.76.1143. arXiv: astro-ph/0405503 [astro-ph].

Punsly, Brian (2001). *Black hole gravitohydromagnetics*.

Rees, Martin J. and Marta Volonteri (2006). "Massive black holes: formation and evolution". In: *Proceedings of the International Astronomical Union* 2.S238, pp. 51–58. DOI: 10.1017/S1743921307004681.

Reid, M. J. and A. Brunthaler (Dec. 2004). "The Proper Motion of Sagittarius A*. II. The Mass of Sagittarius A*". In: ApJ 616.2, pp. 872–884. DOI: 10.1086/424960. arXiv: astro-ph/0408107 [astro-ph].

Reissner, H. (Jan. 1916). "Über die Eigengravitation des elektrischen Feldes nach der Einsteinschen Theorie". In: *Annalen der Physik* 355.9, pp. 106–120. DOI: 10.1002/andp.19163550905.

Remillard, Ronald A. and Jeffrey E. McClintock (Sept. 2006). "X-Ray Properties of Black-Hole Binaries". In: ARA&A 44.1, pp. 49–92. DOI: 10.1146/annurev.astro.44.051905.092532. arXiv: astro-ph/0606352 [astro-ph].

Ressler, S. M. et al. (July 2021). "Magnetically modified spherical accretion in GRMHD: reconnection-driven convection and jet propagation". In: MNRAS 504.4, pp. 6076–6095. DOI: 10.1093/mnras/stab311. arXiv: 2102.01694 [astro-ph.HE].

Rezzolla, Luciano (2016). "An Introduction to Astrophysical Black Holes and Their Dynamical Production". In: *Astrophysical Black Holes*. Ed. by Francesco Haardt et al. Cham: Springer International Publishing, pp. 1–44. ISBN: 978-3-319-19416-5. DOI: 10.1007/978-3-319-19416-5_1. URL: https://doi.org/10.1007/978-3-319-19416-5_1.

Rezzolla, Luciano, Elias R. Most, and Lukas R. Weih (Jan. 2018). "Using Gravitational-wave Observations and Quasi-universal Relations to Constrain the Maximum Mass of Neutron Stars". In: ApJ 852.2, L25, p. L25. DOI: 10.3847/2041-8213/aaa401. arXiv: 1711.00314 [astro-ph.HE].

Ripperda, B. et al. (Jan. 2022). "Black Hole Flares: Ejection of Accreted Magnetic Flux through 3D Plasmoid-mediated Reconnection". In: ApJ 924.2, L32, p. L32. DOI: 10.3847/2041-8213/ac46a1. arXiv: 2109.15115 [astro-ph.HE].

Ripperda, Bart, Fabio Bacchini, and Alexander A. Philippov (Sept. 2020). "Magnetic Reconnection and Hot Spot Formation in Black Hole Accretion Disks". In: ApJ 900.2, 100, p. 100. DOI: 10.3847/1538-4357/ababab. arXiv: 2003.04330 [astro-ph.HE].

Ruiz, Milton, Stuart L. Shapiro, and Antonios Tsokaros (Jan. 2018). "GW170817, general relativistic magnetohydrodynamic simulations, and the neutron star maximum mass". In: Phys. Rev. D 97.2, 021501, p. 021501. DOI: 10.1103/PhysRevD.97.021501. arXiv: 1711.00473 [astro-ph.HE].

Rybicki, George B. and Alan P. Lightman (1986). *Radiative Processes in Astrophysics*.

Salpeter, E. E. (Aug. 1964). "Accretion of Interstellar Matter by Massive Objects." In: ApJ 140, pp. 796–800. DOI: 10.1086/147973.

Salvaterra, Ruben (Sept. 2015). "High redshift Gamma-Ray Bursts". In: *Journal of High Energy Astrophysics* 7, pp. 35–43. DOI: 10.1016/j.jheap.2015.03.001. arXiv: 1503.03072 [astro-ph.CO].

Sapountzis, Konstantinos and Agnieszka Janiuk (Mar. 2019). "The MRI Imprint on the Short-GRB Jets". In: ApJ 873.1, 12, p. 12. DOI: 10.3847/1538-4357/ab0107. arXiv: 1802.02786 [astro-ph.HE].

Savaglio, S., K. Glazebrook, and D. Le Borgne (Jan. 2009). "The Galaxy Population Hosting Gamma-Ray Bursts". In: ApJ 691.1, pp. 182–211. DOI: 10.1088/0004-637X/691/1/182. arXiv: 0803.2718 [astro-ph].

Schmidt, M. (Mar. 1963). "3C 273 : A Star-Like Object with Large Red-Shift". In: Nature 197.4872, p. 1040. DOI: 10.1038/1971040a0.

Schwarzschild, Karl (Jan. 1916). "Über das Gravitationsfeld eines Massenpunktes nach der Einsteinschen Theorie". In: *Sitzungsberichte der Königlich Preussischen Akademie der Wissenschaften*, pp. 189–196.

Seyfert, Carl K. (Jan. 1943). "Nuclear Emission in Spiral Nebulae." In: ApJ 97, p. 28. DOI: 10.1086/144488.

Shakura, N. I. and R. A. Sunyaev (Jan. 1973). "Black holes in binary systems. Observational appearance." In: A&A 24, pp. 337–355.

Shu, F. H. (1992). *The physics of astrophysics. Volume II: Gas dynamics.*

Sonbas, E. et al. (June 2015). "Gamma-ray Bursts: Temporal Scales and the Bulk Lorentz Factor". In: ApJ 805.2, 86, p. 86. DOI: 10.1088/0004-637X/805/2/86. arXiv: 1408.3042 [astro-ph.HE].

Stone, James M. and Michael L. Norman (June 1992). "ZEUS-2D: A Radiation Magnetohydrodynamics Code for Astrophysical Flows in Two Space Dimensions. I. The Hydrodynamic Algorithms and Tests". In: ApJS 80, p. 753. DOI: 10.1086/191680.

Stoner, Edmund (Jan. 1930). "The Equilibrium of Dense Stars". In: *The London* 9.60, pp. 944–963.

Tadhunter, Clive (Aug. 2008). "An introduction to active galactic nuclei: Classification and unification". In: New A Rev. 52.6, pp. 227–239. DOI: 10.1016/j.newar.2008.06.004.

Tchekhovskoy, Alexander, Ramesh Narayan, and Jonathan C. McKinney (Nov. 2011). "Efficient generation of jets from magnetically arrested accretion on a rapidly spinning black hole". In: MNRAS 418.1, pp. L79–L83. DOI: 10.1111/j.1745-3933.2011.01147.x. arXiv: 1108.0412 [astro-ph.HE].

Tolman, Richard C. (Feb. 1939). "Static Solutions of Einstein's Field Equations for Spheres of Fluid". In: *Physical Review* 55.4, pp. 364–373. DOI: 10.1103/PhysRev.55.364.

Tóth, Gábor (July 2000). "The $\nabla\cdot$ B=0 Constraint in Shock-Capturing Magnetohydrodynamics Codes". In: *Journal of Computational Physics* 161.2, pp. 605–652. DOI: 10.1006/jcph.2000.6519.

Velikhov, EP (1959). "Stability of an ideally conducting liquid flowing between cylinders rotating in a magnetic field". In: *Sov. Phys. JETP* 36.9, pp. 995–998.

Visser, Matt (June 2007). "The Kerr spacetime: A brief introduction". In: *arXiv e-prints*, arXiv:0706.0622, arXiv:0706.0622. DOI: 10.48550/arXiv.0706.0622. arXiv: 0706.0622 [gr-qc].

Volonteri, Marta (July 2010). "Formation of supermassive black holes". In: A&A Rev. 18.3, pp. 279–315. DOI: 10.1007/s00159-010-0029-x. arXiv: 1003.4404 [astro-ph.CO].

von Kienlin, A. et al. (Apr. 2020). "The Fourth Fermi-GBM Gamma-Ray Burst Catalog: A Decade of Data". In: ApJ 893.1, 46, p. 46. DOI: 10.3847/1538-4357/ab7a18. arXiv: 2002.11460 [astro-ph.HE].

Wald, Robert M. (Sept. 1974). "Black hole in a uniform magnetic field". In: Phys. Rev. D 10.6, pp. 1680–1685. DOI: 10.1103/PhysRevD.10.1680.

Wang, Chih-Yueh and Roger A. Chevalier (Mar. 2001). "Instabilities and Clumping in Type IA Supernova Remnants". In: ApJ 549.2, pp. 1119–1134. DOI: 10.1086/319439. arXiv: astro-ph/0005105 [astro-ph].

Webster, B. Louise and Paul Murdin (Jan. 1972). "Cygnus X-1-a Spectroscopic Binary with a Heavy Companion ?" In: Nature 235.5332, pp. 37–38. DOI: 10.1038/235037a0.

Weinberg, Steven (1972). *Gravitation and Cosmology: Principles and Applications of the General Theory of Relativity*.

Woosley, S. E. (Mar. 1993). "Gamma-Ray Bursts from Stellar Mass Accretion Disks around Black Holes". In: ApJ 405, p. 273. DOI: 10.1086/172359.

Wu, Qingwen et al. (Jan. 2016). "The extension of variability properties in gamma-ray bursts to blazars". In: MNRAS 455.1, pp. L1–L5. DOI: 10.1093/mnrasl/slv136. arXiv: 1509.04896 [astro-ph.HE].

Xie, Fu-Guo, Ramesh Narayan, and Feng Yuan (Jan. 2023). "Observational Constraints on Direct Electron Heating in the Hot Accretion Flows in Sgr A* and M87*". In: ApJ 942.1, 20, p. 20. DOI: 10.3847/1538-4357/aca534. arXiv: 2210.02879 [astro-ph.HE].

Yarza, Ricardo et al. (July 2020). "Bremsstrahlung in GRMHD Models of Accreting Black Holes". In: ApJ 898.1, 50, p. 50. DOI: 10.3847/1538-4357/ab9808. arXiv: 2006.01145 [astro-ph.HE].

Yuan, Feng and Ramesh Narayan (Aug. 2014). "Hot Accretion Flows Around Black Holes". In: ARA&A 52, pp. 529–588. DOI: 10.1146/annurev-astro-082812-141003. arXiv: 1401.0586 [astro-ph.HE].

Zel'dovich, Ya. B. (Sept. 1964). "The Fate of a Star and the Evolution of Gravitational Energy Upon Accretion". In: *Soviet Physics Doklady* 9, p. 195.

Zhang, Bing (Apr. 2011). "Open questions in GRB physics". In: *Comptes Rendus Physique* 12, pp. 206–225. DOI: 10.1016/j.crhy.2011.03.004. arXiv: 1104.0932 [astro-ph.HE].